RUNX1 marks a luminal castration resistant lineage established at the onset of prostate development

AUTHORS

Renaud Mevel[1], Ivana Steiner[2], Susan Mason[3], Laura C.A. Galbraith[3], Rahima Patel[1], Muhammad ZH Fadlullah[1], Imran Ahmad[3,4], Hing Y. Leung[3,4], Pedro Oliveira[5], Karen Blyth[3,4], Esther Baena[2,6], Georges Lacaud[1,7]

AFFILIATIONS

[1] Cancer Research UK, Stem Cell Biology Group, Cancer Research UK Manchester Institute, The University of Manchester, Alderley Park, Alderley Edge, Macclesfield, SK10 4TG, UK.

[2] Cancer Research UK, Prostate Oncobiology Group, Cancer Research UK Manchester Institute, The University of Manchester, Alderley Park, Alderley Edge, Macclesfield, SK10 4TG, UK.

[3] Cancer Research UK Beatson Institute, Bearsden, Glasgow, G61 1BD, UK.

[4] Institute of Cancer Sciences, College of Medical, Veterinary and Life Sciences, University of Glasgow, Bearsden, Glasgow, G61 1QH, UK.

[5] Department of Pathology, The Christie NHS Foundation Trust, Manchester, UK.

[6] Belfast-Manchester Movember Centre of Excellence, Cancer Research UK Manchester Institute, The University of Manchester, Alderley Park SK10 4TG, UK.

[7] Correspondence: georges.lacaud@manchester.ac.uk

Phone: +44 (0) 161 446 6058, Fax: +44 (0) 161 446 3109

ABSTRACT

The characterization of prostate epithelial hierarchy and lineage heterogeneity is critical to understand its regenerative properties and malignancies. Here, we report that the transcription factor RUNX1 marks a specific subpopulation of proximal luminal cells (PLCs), enriched in the periurethral region of the developing and adult mouse prostate, and distinct from the previously identified NKX3.1^{+} luminal castration resistant cells. Using scRNA-seq profiling and genetic lineage tracing, we show that RUNX1^{+} PLCs are unaffected by androgen deprivation, and do not contribute to the regeneration of the distal luminal compartments. Furthermore, we demonstrate that a transcriptionally similar RUNX1^{+} population emerges at the onset of embryonic prostate specification to populate the proximal region of the ducts. Collectively, our results reveal that RUNX1^{+} PLCs is an intrinsic castration-resistant and self-sustained lineage that emerges early during prostate development and provide new insights into the lineage relationships of the prostate epithelium.

INTRODUCTION

The prostate is a glandular organ of the mammalian male reproductive system. In mice, prostate development starts during embryogenesis at embryonic day (E) 15.5-16.5 with the emergence of the first prostatic buds from the rostral end of the urogenital sinus (UGS) (Bhatia-Gaur et al., 1999; Georgas et al., 2015; Keil et al., 2012; Toivanen & Shen, 2017). These initial buds grow into the surrounding mesenchyme to develop postnatally and through puberty into a branched ductal network organized in distinct pairs of lobes, known as the anterior prostate (AP), dorsolateral prostate (DLP) and ventral prostate (VP) (Sugimura et al., 1986a). Each lobe has distinct branching patterns, histopathological characteristics, and is thought to contribute differently to the physiological function of the prostate. The differentiated epithelium of the adult prostate gland is mainly composed of basal and luminal cells, interspersed with rare neuroendocrine cells (Shen & Abate-Shen, 2010; Toivanen & Shen, 2017; Y. Wang et al., 2001). Luminal cells form a layer of polarized tall columnar cells that depend on androgen signaling and produce the prostatic secretions. Basal cells act as a supportive layer located between the luminal cells and the surrounding stroma.

Despite being mostly quiescent under homeostatic conditions, the prostate gland encompasses incredible plasticity. In mice, surgical castration-induced prostate involution has proven an invaluable tool to identify progenitor castration-resistant cell populations, characterized by their ability to survive in the absence of androgens, and to fully regenerate an intact adult prostate after re-administration of testosterone (Barros-Silva et al., 2018; Kwon et al., 2016; McAuley et al., 2019; Tsujimura et al., 2002; B. Wang et al., 2015; X. Wang et al., 2009; Yoo et al., 2016). Such plasticity has also been shown in defined experimental conditions

to stimulate regenerative properties of epithelial subpopulations, including transplantations (Barros-Silva et al., 2018; Burger et al., 2005; Lawson et al., 2007; Lukacs et al., 2010; Richardson et al., 2004; X. Wang et al., 2009; Xin et al., 2005; Yoo et al., 2016), injury repair (Centonze et al., 2020; Horton et al., 2019; Kwon et al., 2014; Toivanen et al., 2016), and organoid assays (Chua et al., 2014; Höfner et al., 2015; Karthaus et al., 2014). In addition, several studies have proposed that progenitor populations with distinct physiological roles and regenerative capacity reside at different locations within the prostate (Burger et al., 2005; Crowell et al., 2019; Goldstein et al., 2008; Goto et al., 2006; Kwon et al., 2016; Leong et al., 2008; McNeal, 1981; Tsujimura et al., 2002). However, the precise cellular hierarchy and how it is established during development remains controversial.

RUNX transcription factors (TF) are master regulators of lineage commitment and cell fate (Mevel et al., 2019). In particular, RUNX1 is essential for the ontogeny of the hematopoietic system and alterations of RUNX1 have been associated with a broad spectrum of hematological malignancies. Interestingly, increasing evidence implicates RUNX1 in the biology and pathology of hormone-associated epithelia (Lie-A-Ling et al., 2020; Riggio & Blyth, 2017; Scheitz & Tumbar, 2013), including breast (Browne et al., 2015; Chimge et al., 2016; Ferrari et al., 2014; van Bragt et al., 2014), uterine (Planagumà et al., 2004, 2006), ovarian (Keita et al., 2013), and prostate cancers (Banach-Petrosky et al., 2007; Scheitz et al., 2012; Takayama et al., 2015). Despite the documented importance of RUNX TFs and reports of RUNX1 in PCa, its expression in the normal prostate gland during development, homeostasis, and regeneration has not been explored.

In this study, we found that *Runx1* marks a discrete subset of luminal cells located in the proximal region of the prostatic ducts. Using mouse models, combined with lobe-specific single-cell transcriptomic profiling of adult, castrated, and developing prostates, we show that RUNX1^{+} proximal luminal cells represent a distinct lineage established at the onset of prostate development, displaying intrinsic castration-resistant and self-sustaining properties.

RESULTS

RUNX1 marks a subpopulation of prostate proximal luminal cells (PLCs)

We initially sought to characterize the expression pattern of *Runx1* in adult mouse prostate. While RUNX1 was detected in basal cells at multiple spatial locations, its expression was specifically high in a subset of luminal cells found in the proximal region of all three lobes, also known as periurethral (Figures 1A, B; Figure 1–figure supplement 1A, B). Sections were co-stained with NKX3.1, a master regulator of prostate development broadly expressed in luminal cells. Using quantitative image-based cytometry (QBIC), we found that RUNX1 and NKX3.1 had a largely mutually exclusive expression pattern, with a sharp transition from $RUNX1^{+}$ $NKX3.1^{-}$ to $RUNX1^{-}$ $NKX3.1^{+}$ cells in the proximal region (Figures 1A, B; Figure 1–figure supplement 1A, B). These proximal luminal cells had a unique histological profile, with a compact organization, intense nuclear hematoxylin staining, and increased nuclear-to-cytoplasmic ratio (Figure 1–figure supplement 1C). In contrast, distal luminal cells had a large cytoplasm with intense pink eosin staining, likely reflecting their secretory function. These observations suggest that RUNX1 marks a subset of proximal luminal cells, distinct from the abundant $NKX3.1^{+}$ luminal population lining the rest of the prostate epithelium.

The proximal site of the prostate has been proposed to be enriched in cells with stem/progenitor properties (Goldstein et al., 2008; Kwon et al., 2016; Tsujimura et al., 2002; Yoo et al., 2016). In order to study the regenerative potential of *Runx1* expressing cells *ex vivo*, we took advantage of isoform-specific fluorescent reporter mouse models of *Runx1* (Draper et al., 2018; Sroczynska et al., 2009). *Runx1* expression is controlled by two promoters, P1 and P2, that respectively drive the expression of the *Runx1c* and the *Runx1b* isoform (Mevel et al.,

2019). We found that *Runx1* expression in the prostate was exclusively mediated by the proximal P2 promoter, in up to 30% of all epithelial EPCAM^{+} prostate cells (Figure 1–figure supplement 2A-C). Flow-cytometry profiling confirmed the enrichment of P2-*Runx1*:RFP in both basal (EPCAM^{+} CD49f^{high}) and luminal (EPCAM^{+} CD24^{high}) lineages of the proximal compared to the distal prostate (Figures 1C, D; Figure 1–figure supplement 2D). Mirroring our QBIC spatial analysis (Figure 1–figure supplement 1B), P2-*Runx1*:RFP was also detected in a large fraction of the VP epithelium (Figure 1–figure supplement 2D).

We therefore used the P2-*Runx1*:RFP mouse line to isolate *Runx1* positive (RFP^{+}) and negative (RFP^{-}) epithelial cells from the basal and luminal compartments of all three prostate lobes and evaluated their regenerative potential in organoid culture assays (Drost et al., 2016) (Figure 1E). The proximal and distal regions of the AP were analyzed separately. In line with previous reports, basal cells were more efficient at forming organoids compared to all luminal fractions (Drost et al., 2016, Kwon et al., 2015). Importantly, in the luminal fraction, proximal RFP^{+} luminal cells of the AP consistently displayed higher Organoid Formation Capacity (OFC) than the RFP^{-} fraction (Figure 1F). Luminal RFP^{+} sorted cells of the DLP and VP also had a greater OFC than RFP^{-} cells (Figure 1–figure supplement 3A). In contrast, no significant differences in OFC were observed between basal enriched subsets and distal luminal RFP^{+} and RFP^{-} cells. Brightfield assessment revealed that virtually all organoids had a ‘solid’ aspect, except for the predominantly ‘hollow’ organoids derived from proximal RFP^{+} luminal cells (Figure 1–figure supplement 3B). To further characterize their lineage potential, we classified organoids into three types based on the expression of specific lineage markers: unipotent “basal-like” Keratin 5^{+} (K5^{+}), unipotent “luminal-like” Keratin 8^{+} (K8^{+}), or multipotent K5^{+} K8^{+} (Figures 1G, H; Figure

1–figure supplement 3C). Interestingly, AP proximal luminal RFP$^+$ derived organoids were predominantly small unipotent K8$^+$, while the remainder fraction mainly gave larger unipotent K5$^+$ organoids (Figures 1H; Figure 1–figure supplement 3D-E). Few multipotent K5$^+$ K8$^+$ organoids were also identified in nearly all populations.

Together, our results show that RUNX1 marks a specific subset of proximal luminal cells (PLCs), and that its expression in the prostate is mediated by the P2 promoter. RUNX1$^+$ PLCs have a particular predisposition to form unipotent K8$^+$ hollow organoids, suggesting a lineage bias towards the luminal identity, and highlighting differences within the luminal compartment of proximal and distal regions.

Runx1 expressing cells are enriched in the castrated prostate epithelium

In mice, androgen-deprivation can be modelled by surgical castration which leads to prostate regression and enriches for castration-resistant cells (Toivanen & Shen, 2017; Zhang et al., 2018). This process is accompanied by the death of luminal androgen-dependent cells and a small proportion of basal cells (English et al., 1987; Sugimura et al., 1986b). To track changes in *Runx1* expression following androgen withdrawal, we surgically castrated P2-*Runx1*:RFP mice and harvested tissue ≥ 4 weeks post-surgery (Figure 2A). While intact prostates contained 22.8 ± 6.0% RFP$^+$ epithelial cells, their frequency increased to 87 ± 6.0% following castration (Figures 2B, C). High RUNX1 levels were no longer restricted to the proximal region, and RFP was detected in virtually all basal cells of the AP, DLP and VP, as well as more than 75% of the luminal castration-resistant cells (Figures 2D; Figure 2–figure supplement 1A). RUNX1 expressing cells often co-expressed TROP2 (Figure 2E), known to be widely expressed in

castrated prostate epithelium (Goldstein et al., 2008; X.-D. Wang et al., 2007). Several castration-resistant luminal populations have been identified in mice (Barros-Silva et al., 2018; Kwon et al., 2016; McAuley et al., 2019; Tsujimura et al., 2002; B. Wang et al., 2015; X. Wang et al., 2009; Yoo et al., 2016), including rare castration-resistant *Nkx3-1* expressing cells (CARNs). Accordingly, we observed low, but detectable, levels of NKX3.1 in some luminal cells, but only occasional RUNX1$^+$ NKX3.1$^+$ luminal cells in the distal regions of the castrated prostate (Figures 2D; Figure 2–figure supplement 1B, C). Importantly, the clear transition from RUNX1$^+$ to NKX3.1$^+$ cells identified in the proximal luminal layer of intact mice was conserved after castration (Figure 2D, ii).

Together, these results show that RUNX1 is expressed in the majority of the castration-resistant cells. The RUNX1$^+$ NKX3.1$^-$ subset identified in the proximal luminal epithelium of the intact prostate remain NKX3.1$^-$ following castration, supporting the notion that RUNX1$^+$ PLCs constitute a distinct lineage from distal NKX3.1$^+$ cells.

scRNA-seq profiling of *Runx1*$^+$ and *Runx1*$^-$ cells in individual lobes of the intact and castrated prostate

To further characterize the RUNX1$^+$ and RUNX1$^-$ fractions residing at different anatomical locations of the prostate, we performed droplet-based single cell (sc)RNA-seq. We sorted EPCAM$^+$ RFP$^+$ and RFP$^-$ cells from individually dissected lobes of intact and castrated prostates isolated from P2-*Runx1*:RFP reporter mice (Figure 3A). Sorted populations were multiplexed using MULTI-seq lipid-tagged indices to minimize technical confounders such as doublets and batch effects (McGinnis, Patterson, et al., 2019). We retrieved a total of 3,825

prostate epithelial cells from all sorted populations, with a median of 2,846 genes per cell (see Methods; Figure 3–figure supplement 1, 2A-G). We identified 9 *in silico* computed clusters expressing canonical epithelial, basal, and luminal markers (Figure 3–figure supplement 2H-J). A large population of basal cells was annotated by merging 3 tightly connected subclusters broadly expressing *Krt5*, *Krt14,* and *Trp63* (Figures 3B-D; Figure 3–figure supplement 2E, J). Luminal populations expressed surprisingly heterogeneous levels of canonical luminal markers such as *Cd26*/*Dpp4, Cd24a*, *Krt8, and Krt18* (Figure 3–figure supplement 2I). We annotated those distinct clusters as Luminal-A (Lum-A), Lum-B, Lum-C, Lum-D, Lum-E and Lum-F (Figure 3B). Differential gene expression analysis revealed genes strongly associated with each luminal subpopulation (Figures 3C, 3D; Figure 3–figure supplement 3A; Supplementary file 2).

Initially, we sought to evaluate the effect of androgen withdrawal on lobe-specific cellular heterogeneity. Lum-A/B/C/D were largely enriched in luminal cells originating from intact prostates, whereas Lum-E/F contained mainly castrated luminal cells (Figures 3E; Figure 3–figure supplement 3B). Interestingly, Lum-A/C/F mainly contained VP cells, while Lum-B/D/E had a majority of AP and DLP cells, indicating that the lobular identity of luminal cells in the intact prostate is conserved following castration (Figures 3F; Figure 3–figure supplement 3C). These results suggest that a subset of intact Lum-A/C might undergo partial reprogramming during castration-induced regression and gives rise to the Lum-F cluster. Similarly, surviving Lum-B/D may predominantly reprogram into Lum-E cells upon castration. Alternatively, the small fraction of intact cells observed in Lum-E and Lum-F clusters might give rise to the expanded Lum-E/F clusters upon castration. In contrast to luminal cells, castrated basal cells were minimally affected by androgen-deprivation and clustered together with intact basal cells

(Figure 3E). Overall, these results highlight the dramatic changes occurring upon androgen deprivation in the representation of distinct luminal subpopulations.

Runx1 expressing luminal cells are transcriptionally similar to castration-resistant cells

We next specifically focused our attention on RUNX1^{+} luminal cells. The Lum-D cluster predominantly consisted of AP derived RFP^{+} cells, as well as a small number of RFP^{+} DLP and VP cells (Figure 3F, H; Figure 3–figure supplements 2E, 3B, 3C). High *Runx1* expression in Lum-D correlated with higher levels of *Tacstd2*/*Trop2*, Ly6 family members as well as *Runx2* (Figures 3D, G; Figure 3–figure supplements 3D, E). In contrast, *Runx1* was barely detected in clusters Lum-B/C which expressed high levels of *Nkx3-1* while Lum-A cells expressed low levels of both *Runx1* and *Nkx3-1*. These results suggest that the Lum-D cluster corresponds to the distinct RUNX1^{+} luminal cells identified in the proximal region of all three prostate lobes (Figure 1).

To further characterize the specificities of those populations, we performed gene ontology analysis. In line with the secretory role of distal luminal cells, clusters Lum-A/B/C were enriched in enzymatic activity and protein synthesis functions. In contrast, the Lum-D cluster was enriched in terms related to epithelial developmental processes, similar to Lum-E/F (Figure 3–figure supplements 4A-I). This was supported by partition-based graph abstraction (Wolf et al., 2019), which uncovered a strong degree of connectivity between the mainly intact Lum-D and castrated Lum-E population (Figure 3B). Additionally, the Lum-D cluster contained a small, but defined, subpopulation of castrated epithelial cells, suggesting the preservation of its identity upon androgen deprivation (Figures 3E, F). In this population, we found very few genes significantly differentially expressed between intact and castrated cells (n=103; Supplementary

file 3). As expected, androgen-regulated genes including *Psca* and *Tspan1* were downregulated in the castrated subset, while strong contributors of the Lum-D identity such as *Tacstd2*/*Trop2*, *Krt4* and *Runx1* did not vary (Figure 3–figure supplement 4J). These observations further support the hypothesis that Lum-D/RUNX1^{+} PLCs maintain their identity following androgen-deprivation.

Overall, our single-cell transcriptomic analysis highlighted a vast degree of heterogeneity within and between the luminal compartments of both intact and castrated mouse prostates. The tight transcriptional relationship observed between high *Runx1* expressing clusters Lum-D and Lum-E/F suggest that the Lum-D population, which corresponds to PLCs, may contain intrinsically castration-resistant luminal cells

Lineage-tracing of *Runx1* expressing cells establishes the intrinsic castration resistant properties of the proximal luminal lineage

To determine if RUNX1^{+} PLCs were enriched in castration-resistant cells, we combined prostate regression-regeneration assays with genetic lineage-tracing using *Runx1*$^{\text{mER-CRE-mER}}$ *Rosa*$^{\text{flox-stop-flox-tdRFP}}$ mice (Luche et al., 2007; Samokhvalov et al., 2007), henceforth *Runx1*^{CreER} *Rosa26*$^{LSL\text{-}RFP}$ (Figure 4A). Using this model, we could genetically label an average of 4.70 ± 2.8% prostate epithelial *Runx1* expressing cells with RFP upon tamoxifen injection (Figures 4B, C; Figure 4–figure supplement 1A). This corresponded to 0.54 ± 0.2‰ of the total epithelium (Figure 4E). Consistent with the expression pattern of *Runx1*, the majority of labelled cells were located in the proximal region of the prostate (Figure 4C), and co-expressed Keratin 4 (K4) (Figure 4–figure supplements 1D, E), previously found enriched in Lum-D cells (Figure 3D).

Following surgical castration, we found that the absolute number of RFP$^+$ marked cells remained stable (Figure 4–figure supplements 1C, D). However, the frequency of RFP$^+$ cells in the epithelial compartment increased by ~4.3 fold (Figures 4E; Figure 4–figure supplement 1B) indicating that *Runx1* expressing cells have an enhanced capacity to survive castration compared to *Runx1* negative cells. Next, we investigated whether these intrinsically castration-resistant *Runx1* expressing cells were involved in epithelial regeneration upon testosterone addback (Figure 4B, bottom). Surprisingly, only 0.71 ± 0.2‰ RFP$^+$ epithelial cells were found in the regenerated prostate, which was comparable to the intact state (Figures 4E; Figure 4–figure supplements 1B-D). Although the majority of RFP$^+$ clones consisted of single cells, we did observe a minor ~2-fold increase in the frequency of larger clones (2-4 cells) after regeneration, highlighting a modest contribution of RFP labeled cells during prostate regeneration (Figures 4F, G). We found that most RFP marked cells were luminal K8$^+$ in intact, castrated, and regenerated prostates (Figures 4F, H), with only a few basal K5$^+$ RFP$^+$ cells detected in distal areas (Figure 4F). Strikingly, more than 90% of all RFP$^+$ cells remained negative for NKX3.1 in all experimental arms (Figure 4I).

Thus, these results indicate that RFP$^+$ cells, including PLCs, are mostly unaffected by fluctuations in androgen levels during regression-regeneration assays. RUNX1 expression marks intrinsically castration-resistant luminal cells that do not contribute substantially to the expansion of luminal NKX3.1$^+$ cells during prostate regeneration.

Runx1 marks proximal cells during prostate development

Given the singular identity of proximal luminal *Runx1* expressing cells in the adult prostate, we then asked if this luminal lineage was already emerging during prostate development. At E18.5, once the first prostate buds have emerged, RUNX1 was mainly found in the $K8^{high}$ inner layers of the stratified urogenital epithelium (UGE) (Figure 5A). Interestingly, these cells also co-expressed K4 (Figure 5–figure supplement 1A), previously found in the Lum D population (Figure 3D), as well as LY6D, recently shown to mark a subset of adult luminal progenitors (Barros-Silva et al., 2018) (Figure 5–figure supplement 1B). In contrast, RUNX1 expression was low in $p63^+$ and $K5^+$ cells, either lining the outer UGE or found in the tips of premature $NKX3.1^+$ prostate buds (Figures 5A-C). At postnatal day 14 (P14), a prepubescent stage when most of the initial branching events have already occurred (Sugimura et al., 1986a; Tika et al., 2019), RUNX1 was broadly expressed in the proximal region (Figure 5D), mainly in $K4^+$ luminal cells and in some $K5^+$ or $p63^+$ cells (Figure 5–figure supplement 1C-E). Conversely, $NKX3.1^+$ cells were found in distal locations, largely distinct from $RUNX1^+$ cells. The specific spatial expression pattern of RUNX1 in proximal luminal cells, largely mutually exclusive with NKX3.1, suggests that these two transcription factors already mark distinct cellular lineages during embryonic prostate organogenesis.

To study the dynamic emergence of $RUNX1^+$ cells during prostate development, we utilized an explant culture system (Berman et al., 2004; Doles et al., 2005; Kruithof-de Julio et al., 2013; Lopes et al., 1996). Dissected E15.5 UGS were cultured for up to 7 days in the presence of dihydrotestosterone (Figures 5E, F). Bud formation was initiated within 2 days of culture (Figure 5G) and composed of a double positive $K5^+$ $K8^+$ stratified epithelium, partially diversifying by day 7 (Figure 5–figure supplement 2A, B). On day 0 (E15.5), RUNX1 was detected

at the rostral end of the UGE, particularly within the inner layers of the stratified epithelium. After 1 day in culture, NKX3.1 expression emerged in RUNX1$^+$ cells located in the outer layers of the UGE, while defined budding was yet to be observed. On day 2, NKX3.1$^+$ prostate buds were evident and had reduced or absent RUNX1 expression. This pattern was conserved in the mature explant, in which distal tips were mainly NKX3.1$^+$, whereas the proximal area remained RUNX1$^+$ (Figures 5G, H), and co-expressed LY6D and K4 (Figure 5–figure supplements 2C, D). Cellular proliferation marked by Ki67 was more substantial in distal regions, suggesting that most of the expansion did not take place in the RUNX1$^+$ compartment (Figure 5–figure supplement 2E).

These results suggest that prostate budding originates from a subset of cells located in the outer layers of the stratified UGE, transiently marked by RUNX1 and NKX3.1. During embryonic prostate development, *Runx1* expression is already primarily confined to the proximal region of the prostatic ducts, in a distinct compartment from NKX3.1$^+$ cells.

scRNA-seq of explant cultures reveals the specification of the proximal luminal lineage during embryonic prostate development

The characterization by immunostainings of continuous developmental processes is generally constrained to a small number of markers at a time. To further study the specification of RUNX1 and NKX3.1 lineages, we performed scRNA-seq on UGS explant cultures collected at successive time points: E15.5 (D0), day 1 (D1), day 3 (D3), and day 6 (D6) (Figure 6A). After data processing, 3,937 developing prostatic cells were retained, with a median of 3,608 genes per cell (see Methods; Figure 6–figure supplement 1).

Visualization of the dataset using a force-directed layout highlighted the progressive cellular diversification taking place from D0 to D6 (Figure 6B). Cellular populations were divided into 9 clusters, annotated C0 to C8 (Figures 6C-E). C0/C1 contained the majority of D0 and D1 derived cells, while C2-C8 emerged and expanded at later time points. Due to the primitive nature of the UGE at these time points, the classical basal and luminal lineages were not fully established yet (Figures 6F; Figure 6–figure supplements 2A-E; Supplementary file 4). Nevertheless, C4-C6 had a more pronounced 'basal' identity compared to the other clusters. *Krt5*/*Krt14* marked mainly C4, and additional basal markers including *Trp63, Dcn*, *Apoe,* or *Vcan* were higher in C5/C6. Overall, known regulators of prostate development (Toivanen & Shen, 2017) displayed a variable expression pattern across the different clusters. For example, *Foxa1* and *Shh* were strongly expressed in C0/C1, *Notch1* was higher in C3, and *Sox9* in C7 (Figure 6–figure supplement 2C), highlighting the potential of this dataset to interrogate specific features of prostate development.

Consistent with our previous results, *Runx1* was highly expressed in clusters having lower *Nkx3-1* levels, including C0, C1, C2 and C4 (Figure 6G). To determine how these clusters relate to differentiated prostate lineages, we interrogated population-specific gene signatures previously identified in the adult (Figure 3). The 'Basal' signature was enriched across all clusters, especially in C4/C6 (Figures 6I; Figure 6–figure supplement 2F, G). Strikingly, the 'Lum-D' derived signature was highly enriched in C2 compared to all the other adult luminal population signatures, suggesting that the 'Lum-D' fate is determined early during prostate development. The singular identity of C2 was characterized by genes previously found highly

expressed in the adult 'Lum-D' population, including *Tacstd2*/*Trop2*, *Krt4*, *Psca*, as well as *Ly6d* and *Nupr1* (Figure 6H; Figure 6–figure supplement 2A).

Collectively, our scRNA-seq analysis show that adult 'Lum-D'/PLCs share strong similarities with the unique C2 population identified in embryonic explant cultures. This suggests that the distinct proximal luminal lineage is established at the very onset of prostate specification.

RUNX1$^+$ cells contribute to the establishment of the proximal luminal lineage during embryonic prostate development

To trace the fate of RUNX1$^+$ cells during embryonic prostate specification, we cultured UGS explants isolated from the *Runx1^{CreER} Rosa26$^{LSL\text{-}RFP}$* lineage tracing model. We performed 2 pulses of tamoxifen treatment on day 0 and 1 of culture and analyzed the explants on day 2 and day 7 (Figure 7A). The majority of the RFP labeled cells were in the most proximal RUNX1$^+$ subset and rarely found in the distal area of the branches, where RUNX1$^-$ cells reside (Figures 7B, C). Accordingly, the proportion of RFP$^+$ RUNX1$^+$ cells remained stable between day 2 and 7 (Figure 7D). Also, the fraction of RFP$^+$ cells co-expressing p63 remained unchanged throughout the culture (Figure 7–figure supplements 1A-C), while a small fraction diversified into either K5$^+$ or K8$^+$ cells (Figure 7–figure supplements 1D, E). The scattered RFP$^+$ RUNX1$^-$ cells detected in distal branches by day 7 often co-expressed NKX3.1 (Figures 7E, F). Overall, this indicates that *Runx1* expressing cells only marginally contribute to the expansion of the NKX3.1 compartment (Figure 7G). Finally, we wondered whether RUNX1$^+$ cells contributed to the establishment of the proximal luminal lineage. We evaluated the proportion of RFP labelled cells co-expressing

K4, previously identified as a marker of the developing C2 and adult Lum-D populations (Figures 3D and 6H). Interestingly, the fraction of $K4^+$ RFP labeled cells increased from 56.9 ± 10.6% to 74.1 ± 3.0% between day 2 and 7 (Figures 7F, G). There was also an increase of RFP^+ cells expressing *Nupr1*, another marker of the C2 cluster (Figure 7–figure supplements 1F-H). Taken together, these results show that only a small subset of *Runx1* expressing cells contributes to the expansion of $NKX3.1^+$ lineage, found in the distal region of the developing prostatic buds. Instead, the majority of *Runx1* expressing cells preferentially remain in the proximal region of the premature buds, where the proximal luminal lineage is established.

DISCUSSION

In this study, we identified RUNX1 as a new marker of a luminal population enriched in the proximal region of the prostatic ducts. By combining scRNA-seq profiling and genetic lineage tracing of *Runx1* expressing cells, we show that RUNX1^{+} PLCs present in the intact prostate constitute a developmentally distinct and intrinsically castration-resistant luminal lineage. We propose that proximal and distal lineages are separate luminal entities from the earliest stages of prostate development. As such, our study provides novel insights into the cellular composition and developmental hierarchy of the mouse prostate epithelium.

Until the recent advances in single-cell technologies, the prostate epithelial hierarchy was mainly defined based on anatomical features of the basal and luminal layers, their histological characteristics and the expression of a small subset of markers (Shen & Abate-Shen, 2010; Toivanen & Shen, 2017). Here we present two comprehensive scRNA-seq dataset covering both the adult and the developing prostate. To our knowledge, this constitutes the first comprehensive single-cell atlas covering both intact and castrated adult mouse prostates, annotated by their lobe of origin. These datasets can be browsed interactively at http://shiny.cruk.manchester.ac.uk/pscapp/. In particular, our adult scRNA-seq dataset highlighted an extensive degree of cellular heterogeneity, in particular within the luminal epithelia. Several studies recently made similar observations either focusing on the AP (Karthaus et al., 2020), the intact prostate (Crowley et al., 2020; Joseph et al., 2020), or both the intact and castrated prostates (Guo et al., 2020). Integration of these multiple datasets will provide a more global view of the transcriptional landscape of the prostate epithelium.

Although mainly known as a master regulator of hematopoiesis, RUNX1 is increasingly implicated in hormone-associated epithelia including malignant conditions such as prostate cancer (Banach-Petrosky et al., 2007; Lie-A-Ling et al., 2020; Scheitz et al., 2012; Takayama et al., 2015). Here, we identified a subset of RUNX1$^+$ luminal cells located in the proximal region of the developing and adult prostate, referred to as RUNX1$^+$ PLCs, and corresponding to the Lum-D cluster identified in our adult scRNA-seq dataset. Of note, this subset appears to be the equivalent of the 'L2' (Karthaus et al., 2020) or 'LumP' (Crowley et al., 2020), or 'Lum-C' (Guo et al., 2020) clusters identified in recent studies. In light of the extensive contribution of RUNX transcription factors to developmental processes (Mevel et al., 2019), our study suggests that *Runx1*, but also *Runx2*, may be involved in the development and maintenance of specific subpopulations of the prostate epithelium. Future work should therefore aim at characterizing the functional role played by RUNX factors in the prostate, in particular in PLCs.

We demonstrate that these RUNX1$^+$ PLCs exhibit a greater organoid forming potential compared to the remaining luminal fraction, consistent with previous reports isolating similar proximal populations using different markers such as SCA-1, TROP2 or CD26 (Crowley et al., 2020; Goldstein et al., 2008; Guo et al., 2020; Karthaus et al., 2020; Kwon et al., 2016). Furthermore, RUNX1$^+$ PLCs predominantly formed unipotent K8$^+$ hollow organoids demonstrating their preferential commitment to the luminal fate. The greater clonogenicity of RUNX1$^+$ PLCs may in fact be linked to the gene expression profile of the corresponding Lum-D population, suggesting a more immature epithelial state, committed to the luminal lineage but not the secretory function of the prostate. Similar to the enhanced regenerative potential of glandular basal cells under specific regenerative conditions (Centonze et al., 2020), it is

tempting to speculate that these cells act as a latent niche of 'facultative' luminal stem cells (Clevers & Watt, 2018), primed to generate a structured prostatic epithelium under defined conditions.

Further characterization of RUNX1 expression in prostate development revealed a consistent expression pattern with the adult. RUNX1^{+} luminal cells were restricted to the most proximal region of the developing prostate buds, both in embryos and UGS explant cultures. Our scRNA-seq of the developing prostate revealed a broad basal identity, supporting the presence of multipotent basal progenitors during embryonic development (Ousset et al., 2012; Pignon et al., 2013), switching to unipotency postnatally (Tika et al., 2019). However, we observed a distinct cluster (C2) that strongly resembled the adult Lum-D population, suggesting an early branching event towards the proximal luminal fate at the onset of prostate development. Subsequent lineage tracing experiments indicated that *Runx1* expressing cells preferentially populate the emerging proximal luminal identity. It would be interesting to determine if the adult Lum-A, Lum-B, and Lum-C derive from multipotent-basal progenitors or from any specific clusters identified in the developing prostate. This appears to be the case at least for the adult Lum-D/RUNX1^{+} PLCs which already emerges during embryonic specification.

Our data also sheds a light on the regenerative potential of specific epithelial populations. Basal and luminal lineages have previously been shown to be largely self-sustained using generic basal and luminal *Cre* drivers (Choi et al., 2012; Ousset et al., 2012). However, whether distinct subpopulations of luminal cells contribute to the regeneration of the others remains poorly understood (X. Wang et al., 2009; Yoo et al., 2016). Our characterization of RUNX1^{+} PLCs and the detection of a wide variety of luminal populations in our adult prostate

scRNA-seq data highlights the possible existence of multiple self-contained luminal populations. Indeed, *Runx1* driven genetic tracing experiments in regression-regeneration assays revealed that RUNX1^{+} PLCs did not contribute substantially to the regeneration of distal NKX3.1^{+} cells. It was however evident that RUNX1^{+} PLCs are intrinsically castration resistant and capable of sustaining their own lineage in the regenerated prostate. Recently, it was proposed that prostate epithelial regeneration is driven by almost all luminal cells persisting in castrated prostates (Karthaus et al., 2020). Our results are compatible with this model, but we further demonstrate that not all luminal subsets retain the same *in vivo* regenerative potential in response to androgen stimulation. Thus, we suggest that the model of self-sustained basal and luminal populations might be extended to individual luminal subpopulations. This hypothesis should be tested in the future using a more specific Lum-D *Cre* driver (e.g. *Krt4*/*Psca*). It will also be of interest to investigate the self-sustenance of other luminal compartments using Lum-A, Lum-B and Lum-C specific *Cre* drivers.

Finally, our study suggests that the emerging C2/Lum-D population retains a more embryonic-like program, which may relate to their intrinsic castration-resistant potential and have broader relevance to cancer treatment. Along these lines, recent work by Guo and colleagues indicates that *Pten* loss induced in *Psca* expressing cells of the proximal prostate can initiate prostatic intraepithelial neoplasia (Guo et al., 2020). These results warrant future investigation of this luminal subset in the context of cancer development, tumor aggressiveness and treatment responses.

In conclusion, we characterized the expression pattern of *Runx1* in the developing, normal and castrated mouse prostate. We observed that *Runx1* marks proximal luminal cells, which is a distinct luminal lineage emerging early during prostate specification, displaying intrinsic castration-resistant and self-sustaining properties. Our results therefore reveal strong intrinsic lineage differences within the luminal compartment of the prostate epithelium.

MATERIALS AND METHODS

KEY RESOURCES TABLE

Reagent type (species) or resource	Designation	Source or reference	Identifiers	Additional information
Strain, strain background (*Mus musculus,* male)	ICR (CD-1) wild-type	Envigo	Hsd:ICR (CD-1)	7-15 week old males
Strain, strain background (*Mus musculus,* male)	P1-*Runx1*:GFP	Georges Lacaud lab		7-15 week old males
Strain, strain background (*Mus musculus,* male)	P2-*Runx1*:RFP	Georges Lacaud lab		7-15 week old males
Strain, strain background (*Mus musculus,* male)	*Runx1*$^{\text{mER-CRE-mER}}$ *Runx1*^{CreER} *Rosa26*$^{LSL-RFP}$	RIKEN (Japan) Samokhvalov et al., 2007	Runx1-MER-Cre-MER	C57Bl/6J background 7-15 week old males
Strain, strain background (*Mus musculus,* male)	*Rosa26*$^{\text{flox-stop-flox-tdRFP}}$ *Runx1*^{CreER} *Rosa26*$^{LSL-RFP}$	European Mouse Mutant Archive Luche et al., 2007	B6.Cg-Thy1 Gt(ROSA)26 Sortm1Hjf	C57Bl/6J background 7-15 week old males
Antibody	Anti-RUNX1 (rabbit monoclonal)	Cell Signaling	Cat: 8529 RRID:AB_10950225	IHC/IF (1:100)

Antibody	Anti-NKX3.1 (rabbit polyclonal)	Athenaes	Cat: AES-0314	IHC/IF (1:200)
Antibody	Anti-CDH1 (goat polyclonal)	R&D Systems	Cat: AF748 AB_355568	IHC/IF (1:400)
Antibody	Anti-p63 (rabbit monoclonal)	Cell Signaling	Cat: 39692 RRID:AB_2799159	IHC/IF (1:800)
Antibody	Anti-K5 (rabbit monoclonal)	Abcam	Cat: ab52635 RRID:AB_869890	IHC/IF (1:400)
Antibody	Anti-K8 (rabbit monoclonal)	Abcam	Cat: ab53280 RRID:AB_869901	IHC/IF (1:400)
Antibody	Anti-K4 (mouse monoclonal)	Abcam	Cat: Ab9004 RRID:AB_306932	IHC/IF (1:100)
Antibody	Anti-LY6D (rabbit polyclonal)	Proteintech	Cat: 17361-1-AP	IHC/IF (1:100)
Antibody	Anti-TROP-2 (goat polyclonal)	R&D Systems	Cat: AF1122 RRID:AB_2205662	IHC/IF (1:200)
Antibody	Anti-BrdU (rat monoclonal)	Abcam	Cat: ab6326 RRID:AB_305426	IHC/IF (1:400)
Antibody	Anti-Ki67 (rabbit monoclonal)	Abcam	Cat: ab15580 RRID:AB_443209	IHC/IF (1:800)

Antibody	Anti-RFP (rabbit polyclonal)	Rockland	Cat: 600-402-379 RRID:AB_828391	IHC/IF (1:400)
Antibody	Anti-RFP (rabbit monoclonal)	MBL	Cat: PM005 RRID:AB_591279	IF (1:200)
Antibody	Anti-GFP (rabbit polyclonal)	MBL	Cat: 598 RRID:AB_591816	IF (1:200)
Antibody	EnVision+/HRP Anti-Rabbit	Dako (Agilent)	Cat: K4003 RRID:AB_2630375	IHC/IF Ready to use
Antibody	EnVision+/HRP Anti-Rabbit	Dako (Agilent)	Cat: K4001 RRID:AB_2827819	IHC/IF Ready to use
Antibody	ImmPRESS HRP Anti-Goat	Vector Laboratories	Cat: MP-7405 RRID:AB_2336526	IHC/IF Ready to use
Antibody	ImmPRESS HRP Anti-Rat	Vector Laboratories	Cat: MP-7444 RRID:AB_2336530	IHC/IF Ready to use
Antibody	Donkey anti-Goat IgG 647	ThermoFischer Scientific	Cat: A-21447 RRID:AB_141844	IF (1:400)
Antibody	Anti-CD16/32 Fc block	Biolegend	Cat: 101301 Clone: 93 RRID:AB_312800	FACS (1:200)
Antibody	Anti-CD45 SB436	ThermoFischer Scientific	Cat: 62-0451-82 Clone: 30-F11	FACS (1:200)

			RRID:AB_2744774	
Antibody	Anti-EPCAM BV421	Biolegend	Cat: 118225 Clone: G8.8 RRID:AB_2563983	FACS (1:200)
Antibody	Anti-EPCAM APC	Biolegend	Cat: 118214 Clone: G8.8 RRID:AB_1134102	FACS (1:200)
Antibody	Anti-CD49f FITC	Biolegend	Cat: 313606 Clone: GoH3 RRID:AB_345300	FACS (1:200)
Antibody	Anti-CD49f APC	Biolegend	Cat: 313616 Clone: GoH3 RRID:AB_1575047	FACS (1:200)
Antibody	Anti-CD24 BV786	BD Biosciences	Cat: 744470 Clone: M1/69 RRID:AB_2742258	FACS (1:200)
Sequence-based reagent	MULTI-seq reagents	Zev Gartner lab McGinnis, Patterson, et al., 2019		
Software, algorithm	R v3.6.3	CRAN R Project	SCR_001905	https://cran.r-project.org
Software, algorithm	deMULTIplex	McGinnis, Patterson, et al., 2019		https://github.com/chris-mcginnis-ucsf/MULTI-seq

Software, algorithm	DoubletFinder	McGinnis, Murrow, et al., 2019	SCR_018771	https://github.com/chris-mcginnis-ucsf/DoubletFinder
Software, algorithm	Seurat v3.1.5	Rahul Satija lab	SCR_016341	https://github.com/satijalab/seurat
Software, algorithm	Scanpy v1.4.6 PAGA	Wolf et al., 2019	SCR_018139	https://scanpy.readthedocs.io/en/stable/
Software, algorithm	AUCell v1.8.0	Aibar et al., 2017		https://github.com/aertslab/AUCell
Software, algorithm	scater v1.14.6	Bioconductor	SCR_015954	https://bioconductor.org/packages/release/bioc/html/scater.html
Software, algorithm	QuPath v0.2	Bankhead et al., 2017	SCR_018257	https://qupath.github.io/
Software, algorithm	Cellranger v3.1.0	10x Genomics	SCR_017344	
Software, algorithm	FlowJo v10	BD Life Sciences	SCR_008520	
Software, algorithm	Harmony	PerkinElmer	SCR_018809	
Software, algorithm	Graphpad Prism v8.4.2	Graphpad	SCR_002798	

447

448 **Animal work**

449 Animal experiments were approved by the Animal Welfare and Ethics Review Body
450 (AWERB) of the Cancer Research UK Manchester Institute and conducted according to the UK
451 Home Office Project Licence (PPL 70/8580). Genetic lineage-tracing experiments were
452 performed at the Beatson Biological Services Unit (PPL 70/8645 & P5EE22AEE) and approved by
453 the University of Glasgow AWERB. Mice were maintained in purpose-built facility in a 12-hour
454 light/dark cycle with continual access to food and water.

455

456 Immunocompetent wild-type ICR (CD-1) mice were purchased from Envigo. P1-*Runx1*:GFP
457 and P2-*Runx1*:RFP have been described previously (Draper et al., 2018; Sroczynska et al., 2009).
458 Colonies were maintained on a ICR (CD-1) background. C57Bl/6J *Runx1*$^{mER\text{-}CRE\text{-}mER}$ (Samokhvalov
459 et al., 2007) were provided by RIKEN (Japan). C57Bl/6J *Rosa26*$^{flox\text{-}stop\text{-}flox\text{-}tdRFP}$ mice (Luche et al.,
460 2007) were acquired from the European Mouse Mutant Archive (EMMA). For all transgenic
461 lines, routine genotyping was undertaken at weaning (3 weeks of age) by automated PCR
462 genotyping (Transnetyx). For timed mating experiments, vaginal plug detection was considered
463 as embryonic day (E) 0.5.

464

465 All animal procedures were performed on adult males at least 7 weeks of age. Surgical
466 castration was carried out under aseptic conditions. For prostate regeneration assays,
467 testosterone pellets (Belma Technologies) were implanted subcutaneously. For *in vivo* genetic
468 lineage-tracing experiments, tamoxifen (Sigma, T5648) was resuspended in ethanol and diluted

in corn oil at a concentration of 10 mg/mL and administered via intra-peritoneal injections daily for 4 consecutive days using the following regimen: 3mg, 2mg, 2mg, 2mg.

Isolation of mouse prostate cells

All dissections were performed under a stereo microscope in sterile PBS. Dissociated murine prostate cells were obtained by digesting pre-minced prostate tissue for 1h at 37˚C in digestive medium prepared in prepared in ADMEM/F12 (Gibco), and containing 1mg/mL Collagenase Type I (ThermoFischer Scientific, #17018029), 1mg/mL Dispase II (ThermoFischer Scientific, #17105041), 10% Fetal Bovine Serum (Gibco), 1% Penicillin-Streptomycin-Glutamine (Sigma), and 10 µM Y-27632 dyhydrochloride (Chemdea, #CD0141). For embryonic urogenital sinuses (UGS), dissociation time was reduced to 30 min. Single cells were obtained after an additional 10 min incubation in TrypLE (Gibco) at 37˚C before mechanical dissociation with a syringe and needle (25G). Cells were then filtered through a 50 µm cell strainer.

Flow-cytometry and cell-sorting

Single cell suspensions were kept in Advanced DMEM/F-12 (Gibco) containing 5% FBS supplemented with 10 µM Y-27632. Cells were incubated for 10 min using unconjugated anti-mouse CD16/32 antibody (Biolegend, C93, #101301) at 4˚C prior to labelling with specific fluorochrome-labelled antibodies. Details of FACS reagents and antibodies are listed in the Key Resources Table. Cells were filtered through a 50 µm cell strainer prior to acquisition. Hoechst 33258 or Sytox blue (ThermoFischer Scientific) were used as viability stains. Single-cell

suspensions were analyzed on a Fortessa (BD Biosciences) and sorts were performed on a FACSAriaIII (BD Biosciences). FACS data were analyzed using FlowJo software (BD Life Sciences).

Organoid formation assays

In vitro organoid formation assays were performed as described in Drost et al., 2016. Single cells were resuspended in 40 µL drops of phenol red-free Cultrex RGF BME Type 2 (BME 2, Amsbio, #3533-005-02), and seeded in CellCarrier-96 Ultra Microplates (PerkinElmer, #6055302). Defined organoid culture medium was prepared with Advanced DMEM/F-12 (Gibco), supplemented with 10 mM Hepes (Sigma), Gutamax (Gibco), Penicillin/Streptomycin (Sigma), B27 (Life Technologies, 17504-044), 50 mg/mL EGF (PeproTech, #AF-100-15), 500 ng/mL R-spondin 1 (R&D Systems, #4645-RS), 100 ng/mL Noggin (R&D Systems, #6057-NG), 10 mM Y-27632 dyhydrochloride (Chemdea, #CD0141), 200nM A83-01 (Tocris Bioscience, #2939), 1.25 mM N-Acetylcystein (Sigma), and 1 nM Dihydrotestosterone (DHT, Sigma #730637). Medium was refreshed every 2-3 days, and organoid cultures were scored after 7 days.

UGS explant cultures

UGS explant cultures were performed as described previously (Kruithof-de Julio et al., 2013). Briefly, E15.5 embryos were obtained from timed matings. Urogenital sinuses (UGS) were isolated from the embryos and cultured using a Durapore Membrane Filter 0.65 µm (#DVPP02500) placed on a stainless-steel mesh for up to 7 days in Ham's F-12/DMEM (Gibco) supplemented with Insulin-Transferrin-Sodium Selenite Supplement (Roche) and 10 µM dihydrotestosterone (Sigma). Media were renewed every 2-3 days. For lineage-tracing

experiments, tamoxifen-induced labelling was performed using 0.5 µM 4-hydroxytamoxifen (#T176, Sigma).

Immunohistochemistry

Prostate tissues were harvested and fixed in 10% buffered formalin for 24h. Fixed tissues were processed using standard procedures and embedded in paraffin. Formalin-fixed paraffin-embedded (FFPE) sections (4 µm) were cut and dried overnight at 37°C. Multiplexed immunofluorescent stainings of FFPE sections were performed on an automated Leica BOND RX platform using the Opal multiplexing workflow (PerkinElmer). In brief, sections were dewaxed, and rehydrated, and endogenous peroxidase activity was quenched by 10 min pre-treatment with 3% hydrogen peroxide diluted in TBS-T (Tris-Buffered Saline 0.05% Tween-20). Following on-board heat-induced epitope retrieval with citrate buffer (pH 6.0) for 20 min, sections were incubated for 10 min with 10% Casein (Vector Laboratories) diluted in TBS-T. Each staining cycle included a primary antibody incubation for 30 min, followed by buffer washes, and 30 min incubation with HRP labelled secondary antibodies (Key Resources Table). After further washes, the Tyramide labeled with a fluorophore (Opal 520, Opal 570 or Opal 650, PerkinElmer) was added for a final 10 min. Subsequent antibody stainings were performed by repeating the same procedure, separated by heat-mediated antibody denaturation using citrate buffer (pH 6.0) for 5 min at 95°C. Nuclei were counterstained with DAPI (Sigma) and slides were sealed using ProLong Gold Antifade Mountant (ThermoFischer Scientific). *In situ* hybridization (ISH) to detect *Nupr1* (ACD, LS 2.5 Mm-Nupr1 #434818) was done using the Multiplex Fluorescent detection kit (ACD) on the automated Leica BOND RX platform following the manufacturer's instructions.

Pre-treatment was done using an EDTA based pH 9.0 epitope retrieval solution for 15 min at 88°C followed by 10 min protease incubation. After ISH, antibody staining was carried out using an anti-RFP antibody for 1h detected with EnVision HRP anti-rabbit secondary (Agilent) followed by incubation with Tyramide-conjugated Opal 570 (PerkinElmer) as described above. Anti-CDH1 antibody was applied for 1h and detected using an anti-goat Alexa Fluor 647 secondary antibody (ThermoFischer Scientific, #A-21447). Staining of frozen sections was performed as described previously (Thambyrajah et al., 2016). The list of antibodies used is available in the Key Resources Table.

Image acquisition and analysis

Whole-slide images were acquired on an Olympus VS120 slide scanner. Images were analyzed using QuPath v0.2 (Bankhead et al., 2017). Briefly, annotations were drawn manually to select areas of interest. Nuclear detection was achieved using the "cell detection" module on the DAPI channel. A classifier was then trained for each batch of images using the random forest algorithm, to detect the epithelial layers based on either CDH1 or K5/K8 stainings. Single-cell intensity measurements were analyzed using R (3.6.3). For Quantitative Imaged-Based Cytometry (QBIC), single-cell intensity measurements were $\log_{10}$ transformed and plotted using the 'geom_hex' function of the ggplot2 R package. QuPath was used to extract representative high-quality raw images of selected areas from whole slide images using the 'Send region to ImageJ' tool. Images used for publication were processed with ImageJ (NIH Image, Maryland, USA). Confocal images were acquired using a Leica TCS SP8 confocal microscope and LAS X Leica software. Images of whole UGS explant culture were taken using a Leica MZ FLIII microscope.

Whole-mount immunofluorescent staining of organoids

Whole-mount staining was adapted from Yokomizo et al., 2012. Organoids were fixed directly in 96-well plates using 4% paraformaldehyde for 1h at 4°C. After 3 washes of 5 min in PBS, organoids were incubated in PBS-BST, containing PBS, 1% milk, 1% BSA, 10% goat serum (Agilent, #X090710), 0.4% Triton X-100. Pre-conjugated primary antibodies, K5 Alexa Fluor 647 (#ab193895, Abcam) and K8 Alexa Fluor 488 (#ab192467, Abcam) were diluted at 1/400 in PBS-BST and incubated with the organoids overnight at 4°C on a rocking platform. After 3 washes of 1h in PBS-BST at 4°C, organoids were stained with DAPI at 2 µg/mL diluted in PBS-BST and incubated for another 30 min at 4°C on a rocking platform. Images were acquired on an Opera Phenix High Content Screening System using the 10x air and 20x water lenses. Quantitative analysis was performed using the Harmony software on maximum projection images.

scRNA-seq sample preparation

A detailed description of the samples, replicates, and the corresponding cellular populations used for each sequencing run is provided in Supplementary file 1. For the adult mouse prostate dataset, AP, DLP, and VP lobes were micro dissected and pooled from P2-*Runx1*:RFP reporter mice after dissociation. Single live EPCAM^{+} cells from RFP^{+} and RFP^{-} fractions of each lobes were sorted separately (containing a mix of CD49f^{high} basal and CD24^{high} luminal cells). For the UGS explant culture dataset, the middle regions of the explants were micro dissected to enrich for prostatic branching events and pooled by time point after dissociation. Single live EPCAM+ cells were sorted for each independent time point.

578

579 **scRNA-seq sample multiplexing**

580 Individually sorted populations were multiplexed using the MULTI-seq protocol (McGinnis,
581 Patterson, et al., 2019). Reagents were kindly provided by Dr. Zev Gartner. In brief, after
582 sorting, cells were washed once in cold serum- and BSA-free PBS. A lipid-modified DNA
583 oligonucleotide and a specific sample barcode oligonucleotide were then mixed and added to
584 the cells at a final concentration of 200 nM each, and incubated in cold PBS for 5 min. Each
585 individual sample to be multiplexed received an independent sample barcode. Next, a common
586 lipid-modified co-anchor was added at 200 nM to each sample to stabilize the membrane
587 bound barcodes. After an additional 5 min incubation on ice, cells were washed 2 times with
588 PBS containing 1% FBS 1% BSA in order to quench unbound barcodes. Samples were then
589 pooled together and washed once with PBS 1% FBS 1% BSA. After cell counting, cells were
590 loaded in a Chromium Single Cell 3' GEM Library & Gel Bead Kit v3 (10x Genomics).

591

592 **scRNA-seq library preparation, sequencing and pre-processing**

593 Gene expression (cDNA) libraries were prepared according to the manufacturer's protocol.
594 MULTI-seq barcode libraries were separated from the cDNA libraries during the first round of
595 size selection, and PCR amplified prior to sequencing according to the MULTI-seq library
596 preparation protocol (McGinnis, Patterson, et al., 2019). For the adult mouse prostate dataset,
597 cDNA libraries of 'run 1' and 'run 2' were sequenced on Illumina NovaSeq 6000 System, and
598 'run 3' was sequenced on Illumina HiSeq 2500. The UGS mouse prostate explant run was also
599 sequenced on Illumina HiSeq 2500. Sequencing data of cDNA libraries were processed using

Cellranger v3.1.0 and mapped onto mm10 mouse reference genome. Pre-processing of the MULTI-seq library fastq files was performed using the 'deMULTIplex' (v1.0.2) R package (https://github.com/chris-mcginnis-ucsf/MULTI-seq) to generate a sample barcode UMI count matrix. Detailed quality control metrics of each sequencing run are provided in Supplementary file 1.

Adult mouse prostate dataset analysis

Quality control and barcode demultiplexing of individual runs. Each run was pre-processed individually prior data integration. Cellranger outputs were loaded into the R package Seurat (v3.1.5). Cells were kept if they had more than 750 detected genes, less than 7500 UMIs and less than 10% mitochondrial transcripts. Sample barcodes were demultiplexed using the HTODemux function implemented in Seurat. Briefly, a negative binomial distribution was used to estimate the background levels based on *k*-means clustering of the barcode normalized counts. Barcodes with values above the 99% quantile were considered 'positive' for a given sample. Cells positive for more than one barcode were considered as 'doublets'. Doublets and negative cells were excluded for all downstream analyses. Thresholds were empirically adjusted to remove additional cells with possible ambiguous classification (Supplementary file 1). Of note, in both 'run 1' and 'run 2', a large number of cells were classified 'negative' due to the failed labelling of 'Bar3' (corresponding to 'Intact DLP RFP+' sample). For these runs, we used DoubletFinder (McGinnis, Murrow, et al., 2019) to remove predicted doublets missed out as a consequence of the failed labeling of 'Bar3'. After classification, barcodes were represented in

621 UMAP space to confirm the purity of the barcode assignment obtained for each sample (Figure
622 3–figure supplement 5A). We obtained a total of 4,499 cells from 3 independent experiments.
623
624 *Integration, low dimensional embedding and clustering.* Data aggregation was performed
625 according to the standard integration procedure implemented in Seurat. In brief, each dataset
626 was log normalized, and 3000 variable features were initially computed using the 'vst' method.
627 For integration, 2000 features and 50 dimensions were used as anchors. Integrated data were
628 scaled and the first 50 principal components (PC) were calculated for downstream analyses.
629 Uniform Manifold Approximation and Projection (UMAP) (McInnes et al., 2018) was used for
630 visualization. Graph-based louvain clustering was performed on a shared nearest neighbor
631 graph constructed using 20 nearest neighbors for every cell, and a resolution of 0.4, which gave
632 a reasonable segmentation of the data (Figure 3–figure supplement 5B,C). Extensive
633 exploration of each cluster based on known marker genes was then carried out to subset
634 prostate epithelial cells. We found 10 prostate epithelial clusters (*Epcam*, *Krt8*, *Cd24a*, *Spink1*,
635 *Krt19*, *Tacstd2*, *Psca*, *Krt4*, *Tgm4*, *Nkx3-1*, *Pbsn*, *Msmb*, *Piezo2*, *Trp63*, *Krt5*, *Krt14*), 3 clusters of
636 hematopoietic cells (*Vim*, *Ptprc*, *Cd74*, *Itgam*, *Cd3d*), 1 cluster of endothelial cells (*Pecam1*), 1
637 cluster of fibroblasts (*Vim*, *Col1a1*) and 1 cluster of mesonephric derivatives (*Svs2*, *Pax2*) (Figure
638 3–figure supplement 5D,E).
639
640 *Analysis of prostate epithelial populations.* The same dimension reduction approach described
641 above was performed on the selected prostate epithelial clusters, using a resolution of 0.3 for
642 graph-based louvain clustering. We annotated 1 large population of basal cells by merging 3

643 subclusters highly expressing *Krt5*, *Krt14* and *Trp63* as we did not discuss the heterogeneity of
644 the basal compartment in this study (Figures 3B-D; Figure 3–figure supplement 6F,I). We
645 annotated the different luminal clusters expressing higher levels of *Cd26*/*Dpp4, Cd24a*, *Krt8* and
646 *Krt18*, as Lum-A, Lum-B, Lum-C, Lum-D, Lum-E and Lum-F. Several genes specifically marked
647 each cluster, including *Sbp*/*Spink1* in Lum-A, *Tgm4* in Lum-B, *Msmb* in Lum-C, *Psca*/*Krt4* in Lum-
648 D, *Basp1*/*Lpl* in Lum-E, and *Crym* in Lum-F (Figures 3C, D; Figure 3–figure supplement 7A). Data
649 were then imported in Scanpy (v1.4.6) to infer lineage relationships between cellular
650 populations via partition-based graph abstraction (PAGA) implemented in the tl.paga function
651 (Wolf et al., 2019). Briefly, a single cell neighborhood graph (n_neighbors = 50) was computed
652 using the integrated principal components previously calculated in Seurat. PAGA was generated
653 based on our annotated clusters. The final UMAP representation was generated using PAGA-
654 initialised positions to better preserve the global topology of the data. All final data
655 visualizations were generated in R.
656
657 *Differential gene expression analysis and gene ontology.* Differential gene expression analyses
658 between clusters were performed using the MAST method (Finak et al., 2015) implemented in
659 Seurat within the 'FindAllMarkers' and 'FindMarkers' functions. Testing was limited to genes
660 detected in at least 25% of the tested populations (min.pct = 0.25) and showing at least ± 0.25
661 log fold change difference (logfc.threshold = 0.25). The 'g:GOSt' function of the gprofiler2 R
662 package was used to perform functional enrichment analysis on gene ontology terms (GO:BP,
663 biological processes). Genes showing at least 0.50 log fold change enrichment in the group
664 tested were kept.

UGS explant cultures dataset

A similar strategy was applied for the analysis of the UGS explant culture dataset, with some alterations described below.

Quality control and barcode demultiplexing. Cells were kept if they had more than 1000 detected genes, and less than 7.5% mitochondrial transcripts. Barcode classification was performed as above, using the 90% quantile in 'HTODemux' (Figure 6–figure supplement 12A). We obtained a total of 5,122 cells that passed quality control from the 4 time points.

Low dimensional embedding and clustering. The first 50 principal components and 20 neighbors were used for UMAP visualization. Graph-based clustering was done using a resolution parameter of 0.3. We noticed a strong effect of cell cycle using cell cycles genes defined in Tirosh et al., 2016. This was particularly evident using the 'CellCycleScoring' function implemented in Seurat (Figure 6–figure supplement 12B). To minimize the impact of cell cycle on downstream analyses, the cell cycle scores were regressed out during data scaling. We identified 6 main clusters, that we annotated based on the expression of several marker genes (Figure 6–figure supplement 12C-E). We identified 2 clusters of developing mesonephric derivatives (*Hoxb7*, *Wfdc2*, *Gata3*, *Sox17*, *Pax2*, *Pax8*, *Lhx1*), 1 cluster of developing bladder urothelium (*Upk3a*, *Foxq1*, *Plaur*, *Krt7*, *Krt20*), 1 cluster of mesenchymal cells (*Vim*, *Col3a1*, *Col1a1*, *Pdgfra*, *Zeb1*) and 1 cluster corresponding to the developing prostatic epithelium

(*Epcam*, *Krt8*, *Krt5*, *Krt14*, *Krt15*, *Shh*, *Hoxb13*, *Hoxd13*, *Nkx3-1*). We also identified one cluster largely associated with hypoxia and cellular stress ontologies (Figure 6–figure supplement 12F).

Analysis of the developing prostatic epithelium. The same dimension reduction approach was initially applied on the developing prostatic cluster. After graph-based clustering using a resolution of 0.5, 10 clusters were identified and visualized via UMAP (Figure 6–figure supplement 12G-J). We computed diffusion components using 'runDiffusionMap' (ncomponents = 20, k = 20) implemented in the scater (v1.14.6) R package. We found the small cluster C9 to be largely diverging from the remainder fraction in diffusion space, therefore it was excluded for downstream analysis (Figure 6–figure supplement 12K). We then imported the data in Scanpy and used the first 10 diffusion components to compute a neighborhood graph (n_neighbors = 20) which was used for PAGA. We finally computed a force-direct layout (ForceAtlas2) using PAGA-initialised positions.

Analysis of gene set activity. Gene signatures were generated from the list of differentially expressed genes by keeping those showing at least 0.50 log fold change enrichment in each given group. Gene lists were used as custom gene sets (Supplementary file 5) in the AUCell (Aibar et al., 2017) R package (v1.8.0). Briefly, AUCell uses the Area Under the Curve to evaluate the enrichment of a given gene set in each cell, in a ranking based manner. It outputs an AUC score for each individual cell, which is used to explore the relative expression of the signature. Per cell AUC scores of each signatures were overlayed on the dimension reduction layout and plotted as boxplots to visualize enrichments across the different cellular subsets.

Data availability

Raw sequencing files and processed gene expression matrices have been deposited in the NCBI Gene Expression Omnibus under the accession number GSE151944. The processed datasets for both mouse adult prostate and UGS prostate explant cultures can be accessed via a searchable R Shiny application available at http://shiny.cruk.manchester.ac.uk/pscapp/. All code used to process data and generate figures is available on a public GitHub repository at https://github.com/glacaud/prostate-scRNAseq.

Statistical analyses

Statistical analyses were performed using Graphpad/Prism (v8.4.2). Data are represented as mean ±SD. Unless otherwise specified in the corresponding figure legend, two-tailed unpaired *t*-tests were used to compare means between two groups. Statistical significance was set at $p < 0.05$. For animal model studies, no statistical method was used to pre-determine the sample size. No randomization or blinding was used for *in vivo* studies.

ACKNOWLEDGEMENTS

We thank the laboratories' members for critical reading of the manuscript, in particular Dr. Michael Lie-a-ling, Dr. Alice Lallo and Catherine Winchester. We thank the staff at the Histology, Flow Cytometry, Advanced Imaging, Molecular Biology, and Breeding Unit Core facilities of CRUK Manchester Institute, as well as the CRUK Beatson Biological Services Unit and Flow Cytometry Core facility for technical support. We thank Dr. Zev Gartner for kindly providing the MULTI-seq reagents. We thank Dr. Kirsteen Campbell with assistance on the lineage tracing experiments. We thank Dr. Berenika Plusa and Dr. Roberto de la Fuente with assistance on timed matings experiments. We thank Professor Hans Jorg Fehling and the European Mouse Mutant Archive for providing the Rosa26$^{\text{flox-stop-flox-tdRFP}}$ mice.

COMPETING INTERESTS

The authors declare no competing interests.

REFERENCES

Aibar, S., González-Blas, C. B., Moerman, T., Huynh-Thu, V. A., Imrichova, H., Hulselmans, G., Rambow, F., Marine, J.-C., Geurts, P., Aerts, J., van den Oord, J., Atak, Z. K., Wouters, J., & Aerts, S. (2017). SCENIC: Single-cell regulatory network inference and clustering. *Nature Methods*, *14*(11), 1083–1086. https://doi.org/10.1038/nmeth.4463

Banach-Petrosky, W., Jessen, W. J., Ouyang, X., Gao, H., Rao, J., Quinn, J., Aronow, B. J., & Abate-Shen, C. (2007). Prolonged exposure to reduced levels of androgen accelerates prostate cancer progression in Nkx3.1; Pten mutant mice. *Cancer Research*, *67*(19), 9089–9096. https://doi.org/10.1158/0008-5472.CAN-07-2887

Bankhead, P., Loughrey, M. B., Fernández, J. A., Dombrowski, Y., McArt, D. G., Dunne, P. D., McQuaid, S., Gray, R. T., Murray, L. J., Coleman, H. G., James, J. A., Salto-Tellez, M., & Hamilton, P. W. (2017). QuPath: Open source software for digital pathology image analysis. *Scientific Reports*, *7*(1), 16878. https://doi.org/10.1038/s41598-017-17204-5

Barros-Silva, J. D., Linn, D. E., Steiner, I., Guo, G., Ali, A., Pakula, H., Ashton, G., Peset, I., Brown, M., Clarke, N. W., Bronson, R. T., Yuan, G.-C., Orkin, S. H., Li, Z., & Baena, E. (2018). Single-Cell Analysis Identifies LY6D as a Marker Linking Castration-Resistant Prostate Luminal Cells to Prostate Progenitors and Cancer. *Cell Reports*, *25*(12), 3504-3518.e6. https://doi.org/10.1016/j.celrep.2018.11.069

Berman, D. M., Desai, N., Wang, X., Karhadkar, S. S., Reynon, M., Abate-Shen, C., Beachy, P. A., & Shen, M. M. (2004). Roles for Hedgehog signaling in androgen production and prostate ductal morphogenesis. *Developmental Biology*, *267*(2), 387–398. https://doi.org/10.1016/j.ydbio.2003.11.018

760 Bhatia-Gaur, R., Donjacour, A. A., Sciavolino, P. J., Kim, M., Desai, N., Young, P., Norton, C. R.,
761 Gridley, T., Cardiff, R. D., Cunha, G. R., Abate-Shen, C., & Shen, M. M. (1999). Roles for
762 Nkx3.1 in prostate development and cancer. *Genes & Development*, *13*(8), 966–977.
763 Browne, G., Taipaleenmäki, H., Bishop, N. M., Madasu, S. C., Shaw, L. M., van Wijnen, A. J.,
764 Stein, J. L., Stein, G. S., & Lian, J. B. (2015). Runx1 is associated with breast cancer
765 progression in MMTV-PyMT transgenic mice and its depletion in vitro inhibits migration
766 and invasion. *Journal of Cellular Physiology*, *230*(10), 2522–2532.
767 https://doi.org/10.1002/jcp.24989
768 Burger, P. E., Xiong, X., Coetzee, S., Salm, S. N., Moscatelli, D., Goto, K., & Wilson, E. L. (2005).
769 Sca-1 expression identifies stem cells in the proximal region of prostatic ducts with high
770 capacity to reconstitute prostatic tissue. *Proceedings of the National Academy of*
771 *Sciences of the United States of America*, *102*(20), 7180–7185.
772 https://doi.org/10.1073/pnas.0502761102
773 Centonze, A., Lin, S., Tika, E., Sifrim, A., Fioramonti, M., Malfait, M., Song, Y., Wuidart, A., Van
774 Herck, J., Dannau, A., Bouvencourt, G., Dubois, C., Dedoncker, N., Sahay, A., de
775 Maertelaer, V., Siebel, C. W., Van Keymeulen, A., Voet, T., & Blanpain, C. (2020).
776 Heterotypic cell–cell communication regulates glandular stem cell multipotency. *Nature*,
777 *584*(7822), 608–613. https://doi.org/10.1038/s41586-020-2632-y
778 Chimge, N.-O., Little, G. H., Baniwal, S. K., Adisetiyo, H., Xie, Y., Zhang, T., O'Laughlin, A., Liu, Z.
779 Y., Ulrich, P., Martin, A., Mhawech-Fauceglia, P., Ellis, M. J., Tripathy, D., Groshen, S.,
780 Liang, C., Li, Z., Schones, D. E., & Frenkel, B. (2016). RUNX1 prevents oestrogen-

781 mediated AXIN1 suppression and β-catenin activation in ER-positive breast cancer.
782 *Nature Communications*, *7*, 10751. https://doi.org/10.1038/ncomms10751
783 Choi, N., Zhang, B., Zhang, L., Ittmann, M., & Xin, L. (2012). Adult murine prostate basal and
784 luminal cells are self-sustained lineages that can both serve as targets for prostate
785 cancer initiation. *Cancer Cell*, *21*(2), 253–265. https://doi.org/10.1016/j.ccr.2012.01.005
786 Chua, C. W., Shibata, M., Lei, M., Toivanen, R., Barlow, L. J., Bergren, S. K., Badani, K. K.,
787 McKiernan, J. M., Benson, M. C., Hibshoosh, H., & Shen, M. M. (2014). Single luminal
788 epithelial progenitors can generate prostate organoids in culture. *Nature Cell Biology*,
789 *16*(10), 951–961, 1–4. https://doi.org/10.1038/ncb3047
790 Clevers, H., & Watt, F. M. (2018). Defining Adult Stem Cells by Function, not by Phenotype.
791 *Annual Review of Biochemistry*, *87*(1), 1015–1027. https://doi.org/10.1146/annurev-
792 biochem-062917-012341
793 Crowell, P. D., Fox, J. J., Hashimoto, T., Diaz, J. A., Navarro, H. I., Henry, G. H., Feldmar, B. A.,
794 Lowe, M. G., Garcia, A. J., Wu, Y. E., Sajed, D. P., Strand, D. W., & Goldstein, A. S. (2019).
795 Expansion of Luminal Progenitor Cells in the Aging Mouse and Human Prostate. *Cell*
796 *Reports*, *28*(6), 1499-1510.e6. https://doi.org/10.1016/j.celrep.2019.07.007
797 Crowley, L., Cambuli, F., Aparicio, L., Shibata, M., Robinson, B. D., Xuan, S., Li, W., Hibshoosh, H.,
798 Loda, M., Rabadan, R., & Shen, M. M. (2020). A single-cell atlas of the mouse and human
799 prostate reveals heterogeneity and conservation of epithelial progenitors. *ELife*, *9*.
800 https://doi.org/10.7554/eLife.59465

Doles, J. D., Vezina, C. M., Lipinski, R. J., Peterson, R. E., & Bushman, W. (2005). Growth, morphogenesis, and differentiation during mouse prostate development in situ, in renal grafts, and in vitro. *The Prostate*, *65*(4), 390–399. https://doi.org/10.1002/pros.20321

Draper, J. E., Sroczynska, P., Fadlullah, M. Z. H., Patel, R., Newton, G., Breitwieser, W., Kouskoff, V., & Lacaud, G. (2018). A novel prospective isolation of murine fetal liver progenitors to study in utero hematopoietic defects. *PLoS Genetics*, *14*(1), e1007127. https://doi.org/10.1371/journal.pgen.1007127

Drost, J., Karthaus, W. R., Gao, D., Driehuis, E., Sawyers, C. L., Chen, Y., & Clevers, H. (2016). Organoid culture systems for prostate epithelial and cancer tissue. *Nature Protocols*, *11*(2), 347–358. https://doi.org/10.1038/nprot.2016.006

English, H. F., Santen, R. J., & Isaacs, J. T. (1987). Response of glandular versus basal rat ventral prostatic epithelial cells to androgen withdrawal and replacement. *The Prostate*, *11*(3), 229–242.

Ferrari, N., Mohammed, Z. M. A., Nixon, C., Mason, S. M., Mallon, E., McMillan, D. C., Morris, J. S., Cameron, E. R., Edwards, J., & Blyth, K. (2014). Expression of RUNX1 Correlates with Poor Patient Prognosis in Triple Negative Breast Cancer. *PLoS ONE*, *9*(6), e100759. https://doi.org/10.1371/journal.pone.0100759

Finak, G., McDavid, A., Yajima, M., Deng, J., Gersuk, V., Shalek, A. K., Slichter, C. K., Miller, H. W., McElrath, M. J., Prlic, M., Linsley, P. S., & Gottardo, R. (2015). MAST: A flexible statistical framework for assessing transcriptional changes and characterizing heterogeneity in single-cell RNA sequencing data. *Genome Biology*, *16*(1), 278. https://doi.org/10.1186/s13059-015-0844-5

823 Georgas, K. M., Armstrong, J., Keast, J. R., Larkins, C. E., McHugh, K. M., Southard-Smith, E. M.,
824 Cohn, M. J., Batourina, E., Dan, H., Schneider, K., Buehler, D. P., Wiese, C. B., Brennan, J.,
825 Davies, J. A., Harding, S. D., Baldock, R. A., Little, M. H., Vezina, C. M., & Mendelsohn, C.
826 (2015). An illustrated anatomical ontology of the developing mouse lower urogenital
827 tract. *Development (Cambridge, England)*, *142*(10), 1893–1908.
828 https://doi.org/10.1242/dev.117903
829 Goldstein, A. S., Lawson, D. A., Cheng, D., Sun, W., Garraway, I. P., & Witte, O. N. (2008). Trop2
830 identifies a subpopulation of murine and human prostate basal cells with stem cell
831 characteristics. *Proceedings of the National Academy of Sciences of the United States of*
832 *America*, *105*(52), 20882–20887. https://doi.org/10.1073/pnas.0811411106
833 Goto, K., Salm, S. N., Coetzee, S., Xiong, X., Burger, P. E., Shapiro, E., Lepor, H., Moscatelli, D., &
834 Wilson, E. L. (2006). Proximal Prostatic Stem Cells Are Programmed to Regenerate a
835 Proximal-Distal Ductal Axis. *STEM CELLS*, *24*(8), 1859–1868.
836 https://doi.org/10.1634/stemcells.2005-0585
837 Guo, W., Li, L., He, J., Liu, Z., Han, M., Li, F., Xia, X., Zhang, X., Zhu, Y., Wei, Y., Li, Y., Aji, R., Dai,
838 H., Wei, H., Li, C., Chen, Y., Chen, L., & Gao, D. (2020). Single-cell transcriptomics
839 identifies a distinct luminal progenitor cell type in distal prostate invagination tips.
840 *Nature Genetics*, *52*(9), 908–918. https://doi.org/10.1038/s41588-020-0642-1
841 Höfner, T., Eisen, C., Klein, C., Rigo-Watermeier, T., Goeppinger, S. M., Jauch, A., Schoell, B.,
842 Vogel, V., Noll, E., Weichert, W., Baccelli, I., Schillert, A., Wagner, S., Pahernik, S., Sprick,
843 M. R., & Trumpp, A. (2015). Defined Conditions for the Isolation and Expansion of Basal

844 Prostate Progenitor Cells of Mouse and Human Origin. *Stem Cell Reports*, *4*(3), 503–518.
845 https://doi.org/10.1016/j.stemcr.2015.01.015
846 Horton, C., Liu, Y., Yu, C., Xie, Q., & Wang, Z. A. (2019). Luminal-contact-inhibition of epithelial
847 basal stem cell multipotency in prostate organogenesis and homeostasis. *Biology Open*,
848 *8*(10). https://doi.org/10.1242/bio.045724
849 Joseph, D. B., Henry, G. H., Malewska, A., Iqbal, N. S., Ruetten, H. M., Turco, A. E., Abler, L. L.,
850 Sandhu, S. K., Cadena, M. T., Malladi, V. S., Reese, J. C., Mauck, R. J., Gahan, J. C.,
851 Hutchinson, R. C., Roehrborn, C. G., Baker, L. A., Vezina, C. M., & Strand, D. W. (2020).
852 Urethral luminal epithelia are castration-insensitive cells of the proximal prostate. *The*
853 *Prostate*. https://doi.org/10.1002/pros.24020
854 Karthaus, W. R., Hofree, M., Choi, D., Linton, E. L., Turkekul, M., Bejnood, A., Carver, B.,
855 Gopalan, A., Abida, W., Laudone, V., Biton, M., Chaudhary, O., Xu, T., Masilionis, I.,
856 Manova, K., Mazutis, L., Pe'er, D., Regev, A., & Sawyers, C. L. (2020). Regenerative
857 potential of prostate luminal cells revealed by single-cell analysis. *Science*, *368*(6490),
858 497–505. https://doi.org/10.1126/science.aay0267
859 Karthaus, W. R., Iaquinta, P. J., Drost, J., Gracanin, A., van Boxtel, R., Wongvipat, J., Dowling, C.
860 M., Gao, D., Begthel, H., Sachs, N., Vries, R. G. J., Cuppen, E., Chen, Y., Sawyers, C. L., &
861 Clevers, H. C. (2014). Identification of multipotent luminal progenitor cells in human
862 prostate organoid cultures. *Cell*, *159*(1), 163–175.
863 https://doi.org/10.1016/j.cell.2014.08.017
864 Keil, K. P., Mehta, V., Abler, L. L., Joshi, P. S., Schmitz, C. T., & Vezina, C. M. (2012). Visualization
865 and quantification of mouse prostate development by in situ hybridization.

Differentiation; Research in Biological Diversity, *84*(3), 232–239. https://doi.org/10.1016/j.diff.2012.07.005

Keita, M., Bachvarova, M., Morin, C., Plante, M., Gregoire, J., Renaud, M.-C., Sebastianelli, A., Trinh, X. B., & Bachvarov, D. (2013). The RUNX1 transcription factor is expressed in serous epithelial ovarian carcinoma and contributes to cell proliferation, migration and invasion. *Cell Cycle (Georgetown, Tex.)*, *12*(6), 972–986. https://doi.org/10.4161/cc.23963

Kruithof-de Julio, M., Shibata, M., Desai, N., Reynon, M., Halili, M. V., Hu, Y.-P., Price, S. M., Abate-Shen, C., & Shen, M. M. (2013). Canonical Wnt signaling regulates Nkx3.1 expression and luminal epithelial differentiation during prostate organogenesis. *Developmental Dynamics : An Official Publication of the American Association of Anatomists*, *242*(10), 1160–1171. https://doi.org/10.1002/dvdy.24008

Kwon, O.-J., Zhang, L., Ittmann, M. M., & Xin, L. (2014). Prostatic inflammation enhances basal-to-luminal differentiation and accelerates initiation of prostate cancer with a basal cell origin. *Proceedings of the National Academy of Sciences of the United States of America*, *111*(5), E592-600. https://doi.org/10.1073/pnas.1318157111

Kwon, O.-J., Zhang, L., & Xin, L. (2016). Stem Cell Antigen-1 Identifies a Distinct Androgen-Independent Murine Prostatic Luminal Cell Lineage with Bipotent Potential. *STEM CELLS*, *34*(1), 191–202. https://doi.org/10.1002/stem.2217

Lawson, D. A., Xin, L., Lukacs, R. U., Cheng, D., & Witte, O. N. (2007). Isolation and functional characterization of murine prostate stem cells. *Proceedings of the National Academy of*

887 *Sciences of the United States of America*, *104*(1), 181–186.

888 https://doi.org/10.1073/pnas.0609684104

889 Leong, K. G., Wang, B.-E., Johnson, L., & Gao, W.-Q. (2008). Generation of a prostate from a

890 single adult stem cell. *Nature*, *456*(7223), 804–808.

891 https://doi.org/10.1038/nature07427

892 Lie-A-Ling, M., Mevel, R., Patel, R., Blyth, K., Baena, E., Kouskoff, V., & Lacaud, G. (2020). RUNX1

893 Dosage in Development and Cancer. *Molecules and Cells*, *43*(2), 126–138.

894 https://doi.org/10.14348/molcells.2019.0301

895 Lopes, E. S., Foster, B. A., Donjacour, A. A., & Cunha, G. R. (1996). Initiation of secretory activity

896 of rat prostatic epithelium in organ culture. *Endocrinology*, *137*(10), 4225–4234.

897 https://doi.org/10.1210/endo.137.10.8828481

898 Luche, H., Weber, O., Nageswara Rao, T., Blum, C., & Fehling, H. J. (2007). Faithful activation of

899 an extra-bright red fluorescent protein in 'knock-in' Cre-reporter mice ideally suited for

900 lineage tracing studies. *European Journal of Immunology*, *37*(1), 43–53.

901 https://doi.org/10.1002/eji.200636745

902 Lukacs, R. U., Goldstein, A. S., Lawson, D. A., Cheng, D., & Witte, O. N. (2010). Isolation,

903 cultivation and characterization of adult murine prostate stem cells. *Nature Protocols*,

904 *5*(4), 702–713. https://doi.org/10.1038/nprot.2010.11

905 McAuley, E., Moline, D., VanOpstall, C., Lamperis, S., Brown, R., & Vander Griend, D. J. (2019).

906 Sox2 Expression Marks Castration-Resistant Progenitor Cells in the Adult Murine

907 Prostate. *Stem Cells (Dayton, Ohio)*, *37*(5), 690–700. https://doi.org/10.1002/stem.2987

McGinnis, C. S., Murrow, L. M., & Gartner, Z. J. (2019). DoubletFinder: Doublet Detection in Single-Cell RNA Sequencing Data Using Artificial Nearest Neighbors. *Cell Systems*, *8*(4), 329-337.e4. https://doi.org/10.1016/j.cels.2019.03.003

McGinnis, C. S., Patterson, D. M., Winkler, J., Conrad, D. N., Hein, M. Y., Srivastava, V., Hu, J. L., Murrow, L. M., Weissman, J. S., Werb, Z., Chow, E. D., & Gartner, Z. J. (2019). MULTI-seq: Sample multiplexing for single-cell RNA sequencing using lipid-tagged indices. *Nature Methods*, *16*(7), 619–626. https://doi.org/10.1038/s41592-019-0433-8

McInnes, L., Healy, J., & Melville, J. (2018). UMAP: Uniform Manifold Approximation and Projection for Dimension Reduction. *ArXiv:1802.03426 [Cs, Stat]*. http://arxiv.org/abs/1802.03426

McNeal, J. E. (1981). The zonal anatomy of the prostate. *The Prostate*, *2*(1), 35–49. https://doi.org/10.1002/pros.2990020105

Mevel, R., Draper, J. E., Lie-a-Ling, M., Kouskoff, V., & Lacaud, G. (2019). RUNX transcription factors: Orchestrators of development. *Development*, *146*(17), dev148296. https://doi.org/10.1242/dev.148296

Ousset, M., Van Keymeulen, A., Bouvencourt, G., Sharma, N., Achouri, Y., Simons, B. D., & Blanpain, C. (2012). Multipotent and unipotent progenitors contribute to prostate postnatal development. *Nature Cell Biology*, *14*(11), 1131–1138. https://doi.org/10.1038/ncb2600

Pignon, J.-C., Grisanzio, C., Geng, Y., Song, J., Shivdasani, R. A., & Signoretti, S. (2013). P63-expressing cells are the stem cells of developing prostate, bladder, and colorectal

929 epithelia. *Proceedings of the National Academy of Sciences of the United States of*
930 *America*, *110*(20), 8105–8110. https://doi.org/10.1073/pnas.1221216110
931 Planagumà, J., Díaz-Fuertes, M., Gil-Moreno, A., Abal, M., Monge, M., García, A., Baró, T.,
932 Thomson, T. M., Xercavins, J., Alameda, F., & Reventós, J. (2004). A differential gene
933 expression profile reveals overexpression of RUNX1/AML1 in invasive endometrioid
934 carcinoma. *Cancer Research*, *64*(24), 8846–8853. https://doi.org/10.1158/0008-
935 5472.CAN-04-2066
936 Planagumà, J., Gonzalez, M., Doll, A., Monge, M., Gil-Moreno, A., Baró, T., García, A., Xercavins,
937 J., Alameda, F., Abal, M., & Reventós, J. (2006). The up-regulation profiles of
938 p21WAF1/CIP1 and RUNX1/AML1 correlate with myometrial infiltration in endometrioid
939 endometrial carcinoma. *Human Pathology*, *37*(8), 1050–1057.
940 https://doi.org/10.1016/j.humpath.2006.03.007
941 Richardson, G. D., Robson, C. N., Lang, S. H., Neal, D. E., Maitland, N. J., & Collins, A. T. (2004).
942 CD133, a novel marker for human prostatic epithelial stem cells. *Journal of Cell Science*,
943 *117*(16), 3539–3545. https://doi.org/10.1242/jcs.01222
944 Riggio, A. I., & Blyth, K. (2017). The enigmatic role of RUNX1 in female-related cancers—Current
945 knowledge & future perspectives. *The FEBS Journal*, *284*(15), 2345–2362.
946 https://doi.org/10.1111/febs.14059
947 Samokhvalov, I. M., Samokhvalova, N. I., & Nishikawa, S. (2007). Cell tracing shows the
948 contribution of the yolk sac to adult haematopoiesis. *Nature*, *446*(7139), 1056–1061.
949 https://doi.org/10.1038/nature05725

950 Scheitz, C. J. F., Lee, T. S., McDermitt, D. J., & Tumbar, T. (2012). Defining a tissue stem cell-
951 driven Runx1/Stat3 signalling axis in epithelial cancer. *The EMBO Journal*, *31*(21), 4124–
952 4139. https://doi.org/10.1038/emboj.2012.270
953 Scheitz, C. J. F., & Tumbar, T. (2013). New insights into the role of Runx1 in epithelial stem cell
954 biology and pathology. *Journal of Cellular Biochemistry*, *114*(5), 985–993.
955 https://doi.org/10.1002/jcb.24453
956 Shen, M. M., & Abate-Shen, C. (2010). Molecular genetics of prostate cancer: New prospects for
957 old challenges. *Genes & Development*, *24*(18), 1967–2000.
958 https://doi.org/10.1101/gad.1965810
959 Sroczynska, P., Lancrin, C., Kouskoff, V., & Lacaud, G. (2009). The differential activities of Runx1
960 promoters define milestones during embryonic hematopoiesis. *Blood*, *114*(26), 5279–
961 5289. https://doi.org/10.1182/blood-2009-05-222307
962 Sugimura, Y., Cunha, G. R., & Donjacour, A. A. (1986a). Morphogenesis of ductal networks in the
963 mouse prostate. *Biology of Reproduction*, *34*(5), 961–971.
964 https://doi.org/10.1095/biolreprod34.5.961
965 Sugimura, Y., Cunha, G. R., & Donjacour, A. A. (1986b). Morphological and histological study of
966 castration-induced degeneration and androgen-induced regeneration in the mouse
967 prostate. *Biology of Reproduction*, *34*(5), 973–983.
968 Takayama, K., Suzuki, T., Tsutsumi, S., Fujimura, T., Urano, T., Takahashi, S., Homma, Y.,
969 Aburatani, H., & Inoue, S. (2015). RUNX1, an androgen- and EZH2-regulated gene, has
970 differential roles in AR-dependent and -independent prostate cancer. *Oncotarget*, *6*(4),
971 2263–2276. https://doi.org/10.18632/oncotarget.2949

Thambyrajah, R., Mazan, M., Patel, R., Moignard, V., Stefanska, M., Marinopoulou, E., Li, Y., Lancrin, C., Clapes, T., Möröy, T., Robin, C., Miller, C., Cowley, S., Göttgens, B., Kouskoff, V., & Lacaud, G. (2016). GFI1 proteins orchestrate the emergence of haematopoietic stem cells through recruitment of LSD1. *Nature Cell Biology*, *18*(1), 21–32. https://doi.org/10.1038/ncb3276

Tika, E., Ousset, M., Dannau, A., & Blanpain, C. (2019). Spatiotemporal regulation of multipotency during prostate development. *Development*, dev.180224. https://doi.org/10.1242/dev.180224

Tirosh, I., Izar, B., Prakadan, S. M., Wadsworth, M. H., Treacy, D., Trombetta, J. J., Rotem, A., Rodman, C., Lian, C., Murphy, G., Fallahi-Sichani, M., Dutton-Regester, K., Lin, J.-R., Cohen, O., Shah, P., Lu, D., Genshaft, A. S., Hughes, T. K., Ziegler, C. G. K., … Garraway, L. A. (2016). Dissecting the multicellular ecosystem of metastatic melanoma by single-cell RNA-seq. *Science*, *352*(6282), 189–196. https://doi.org/10.1126/science.aad0501

Toivanen, R., Mohan, A., & Shen, M. M. (2016). Basal Progenitors Contribute to Repair of the Prostate Epithelium Following Induced Luminal Anoikis. *Stem Cell Reports*, *0*(0). https://doi.org/10.1016/j.stemcr.2016.03.007

Toivanen, R., & Shen, M. M. (2017). Prostate organogenesis: Tissue induction, hormonal regulation and cell type specification. *Development (Cambridge, England)*, *144*(8), 1382–1398. https://doi.org/10.1242/dev.148270

Tsujimura, A., Koikawa, Y., Salm, S., Takao, T., Coetzee, S., Moscatelli, D., Shapiro, E., Lepor, H., Sun, T.-T., & Wilson, E. L. (2002). Proximal location of mouse prostate epithelial stem

cells. *The Journal of Cell Biology*, *157*(7), 1257–1265. https://doi.org/10.1083/jcb.200202067

van Bragt, M. P. A., Hu, X., Xie, Y., & Li, Z. (2014). RUNX1, a transcription factor mutated in breast cancer, controls the fate of ER-positive mammary luminal cells. *ELife*, *3*, e03881. https://doi.org/10.7554/eLife.03881

Wang, B., Wang, X., Long, J. E., Eastham-Anderson, J., Firestein, R., & Junttila, M. R. (2015). Castration-Resistant Lgr5+ Cells Are Long-Lived Stem Cells Required for Prostatic Regeneration. *Stem Cell Reports*, *4*(5), 768–779. https://doi.org/10.1016/j.stemcr.2015.04.003

Wang, X., Kruithof-de Julio, M., Economides, K. D., Walker, D., Yu, H., Halili, M. V., Hu, Y.-P., Price, S. M., Abate-Shen, C., & Shen, M. M. (2009). A luminal epithelial stem cell that is a cell of origin for prostate cancer. *Nature*, *461*(7263), 495–500. https://doi.org/10.1038/nature08361

Wang, X.-D., Wang, B.-E., Soriano, R., Zha, J., Zhang, Z., Modrusan, Z., Cunha, G. R., & Gao, W.-Q. (2007). Expression profiling of the mouse prostate after castration and hormone replacement: Implication of H-cadherin in prostate tumorigenesis. *Differentiation; Research in Biological Diversity*, *75*(3), 219–234. https://doi.org/10.1111/j.1432-0436.2006.00135.x

Wang, Y., Hayward, S., Cao, M., Thayer, K., & Cunha, G. (2001). Cell differentiation lineage in the prostate. *Differentiation; Research in Biological Diversity*, *68*(4–5), 270–279.

Wolf, F. A., Hamey, F. K., Plass, M., Solana, J., Dahlin, J. S., Göttgens, B., Rajewsky, N., Simon, L., & Theis, F. J. (2019). PAGA: Graph abstraction reconciles clustering with trajectory

1015 inference through a topology preserving map of single cells. *Genome Biology*, *20*(1), 59.
1016 https://doi.org/10.1186/s13059-019-1663-x
1017 Xin, L., Lawson, D. A., & Witte, O. N. (2005). The Sca-1 cell surface marker enriches for a
1018 prostate-regenerating cell subpopulation that can initiate prostate tumorigenesis.
1019 *Proceedings of the National Academy of Sciences of the United States of America*,
1020 *102*(19), 6942–6947. https://doi.org/10.1073/pnas.0502320102
1021 Yokomizo, T., Yamada-Inagawa, T., Yzaguirre, A. D., Chen, M. J., Speck, N. A., & Dzierzak, E.
1022 (2012). Whole-mount three-dimensional imaging of internally localized immunostained
1023 cells within mouse embryos. *Nature Protocols*, *7*(3), 421–431.
1024 https://doi.org/10.1038/nprot.2011.441
1025 Yoo, Y. A., Roh, M., Naseem, A. F., Lysy, B., Desouki, M. M., Unno, K., & Abdulkadir, S. A. (2016).
1026 Bmi1 marks distinct castration-resistant luminal progenitor cells competent for prostate
1027 regeneration and tumour initiation. *Nature Communications*, *7*, 12943.
1028 https://doi.org/10.1038/ncomms12943
1029 Zhang, D., Zhao, S., Li, X., Kirk, J. S., & Tang, D. G. (2018). Prostate Luminal Progenitor Cells in
1030 Development and Cancer. *Trends in Cancer*, *4*(11), 769–783.
1031 https://doi.org/10.1016/j.trecan.2018.09.003
1032

MAIN FIGURE LEGENDS

Figure 1. RUNX1 marks a subpopulation of mouse proximal prostate luminal cells (PLCs).

(**A**) Co-immunostaining of RUNX1, NKX3.1, CDH1 in the mouse Anterior Prostate (AP). Higher magnification images of (i) proximal AP and (ii) distal AP are shown. Arrows indicate RUNX1$^+$ NKX3.1$^-$ cells, arrowheads show RUNX1$^-$ NKX3.1$^+$ cells. Scale bars: 500µm (yellow) and 50µm (white). (**B**) Quantification of RUNX1 and NKX3.1 nuclear intensity (log_{10}) in CDH1$^+$ epithelial cells by QBIC in proximal and distal AP. *n* = 6-8 mice. (**C, D**) Flow-cytometry analysis of P2-*Runx1*:RFP mice, and corresponding quantification of the percentages of RFP$^+$ and RFP cells in the basal and luminal fractions of the proximal and distal AP. *n* = 7 mice. (**E**) Experimental strategy to grow organoids from sorted RFP$^+$ and RFP cells from the basal (CD49f^{high}) and luminal (CD24^{high}) lineages of P2-*Runx1*:RFP mouse reporters. (**F**) Organoid Forming Capacity (OFC) of RFP$^+$ and RFP$^-$ basal and luminal sorted cells after 7 days in culture. *n* = 4 mice. (**G**) Whole-mount immunostaining of unipotent K5$^+$, unipotent K8$^+$ or multipotent K5$^+$ K8$^+$ organoids. Scale bar: 50 µm. (**H**) Quantification of the type of organoids characterized by whole-mount immunostaining, as in G. Numbers of organoids quantified are shown above the graph. *p* value is indicated for the proportion of K8$^+$ organoids between Proximal AP Luminal RFP$^+$ versus RFP$^-$ derived subset. Other comparisons were not statistically significant. *n* = 2 mice per group. Source files are available in Figure 1—source data 1.

Figure 2. RUNX1 expressing cells are enriched in the castrated prostate epithelium.

(**A**) P2-*Runx1*:RFP reporter mice were surgically castrated between 6 to 12 weeks of age and analyzed at least 4 weeks post-castration. (**B**, **C**) Flow-cytometry analysis and corresponding

quantification of the proportion of RFP^+ and RFP^- cells in the $EPCAM^+$ fraction of intact and castrated prostates of P2-*Runx1*:RFP mice. *n* = 3 mice per group. Int: Intact, Cas: Castrated. (**D**) Co-immunostaining of RUNX1, NKX3.1, CDH1 in the castrated wild-type mouse prostate. Higher magnification images of (i) proximal, (ii) intermediate and (iii) distal AP are shown. Arrows indicate $RUNX1^-$ $NKX3.1^+$ cells, arrowheads show a luminal cell co-stained for RUNX1 and NKX3.1. Amp: ampullary gland. Scale bars: 500 µm (yellow) and 50 µm (white). Int: Intact, Cas: Castrated. (**E**) Co-immunostaining of RUNX1 and TROP2 showing colocalization of the 2 markers in both proximal (bottom) and distal (top) castrated AP. Scale bars: 50 µm (white). Source files are available in Figure 2—source data 1.

Figure 3. scRNA-seq profiling of intact and castrated *Runx1*$^+$ cells reveals transcriptomic similarity between proximal luminal cells and castration-resistant cells.

(**A**) Experimental strategy for scRNA-seq on RFP^+ and RFP^- cells individually dissected lobes of intact and castrated prostates isolated from P2-*Runx1*:RFP reporter mice. (**B**) UMAP visualization (left) and graph-abstracted representation (PAGA, right) of prostate epithelial cells (*n* = 3,825 cells from 3 independent experiments). Colors represent different clusters. In PAGA, clusters are linked by weighted edges that represent a statistical measure of connectivity. (**C**) Dot plot showing the expression of selected marker genes associated with each cluster. (**D-H**) UMAP visualization of prostate epithelial cells. Cells in **D** and **G** are colored by a gradient of log-normalized expression levels for each gene indicated. Cell colors in **E** represent the treatment of origin (intact, castrated), in **F** individual lobes of origin (AP, DLP, VP), and in **H** RFP FACS gate of origin (RFP^+, RFP^-).

Figure 4. Lineage-tracing of *Runx1* expressing cells establishes the intrinsic castration-resistant properties of the proximal luminal lineage.

(**A**) Schematic summary of the genetic lineage tracing system employed. (**B**) Experimental strategy for lineage-tracing experiments. (**C**) Co-immunostaining of RFP, RUNX1, CDH1 in the proximal AP. Arrows indicate RFP labelled RUNX1$^+$ cells. Scale bar: 50 µm. (**D**) Quantification of the percentage of epithelial RFP$^+$ cells in proximal and distal regions of the prostate in intact (*n* = 5), castrated (*n* = 4) and regenerated (*n* = 4) mice. (**E**) Quantification of the percentage of epithelial RFP$^+$ cells in intact (*n* = 5), castrated (*n* = 5) and regenerated (*n* = 4) mice. (**F**) Co-immunostaining of RFP, K5, K8 in the proximal AP, distal AP, and DLVP (DLP + VP). Arrowheads indicate RFP labelled basal cells (K5$^+$) found in distal AP, the white arrow indicates a luminal (K8$^+$) RFP$^+$ clone made of 2 cells. Scale bar: 50 µm. (**G**) Quantification of the percentage of epithelial RFP$^+$ clones comprising between 2 to 4 cells in intact (*n* = 5), castrated (*n* = 5) and regenerated (*n* = 4) mice. (**H, I**) Quantification of the percentage of RFP$^+$ cells being K5$^+$ or K8$^+$ in **H**, or NKX3.1$^+$ or NKX3.1$^-$ in **I,** in intact (*n* = 5), castrated (*n* = 5) and regenerated (*n* = 4) mice. Int: Intact, Cas: Castrated, Rgn: Regenerated. Source files are available in Figure 4—source data 1.

Figure 5. RUNX1 marks proximal cells during embryonic prostate development.

(**A-C**) Co-immunostainings of the mouse urogenital sinus at E18.5 for RUNX1, K5, K8 in **A**, RUNX1, p63, CDH1 in **B**, RUNX1, NKX3.1, CDH1 in **C**. Scale bar: 50 µm. (**D**) Co-immunostainings of RUNX1, NKX3.1, CDH1 at postnatal (P) day 14. Higher magnification images of (p) proximal, (i) intermediate, and (d) distal regions are shown. Scale bars: 200 µm (yellow) and 50 µm

(white). Amp: ampullary gland; Sv: seminal vesicles; Ur: urethra; p: proximal; i: intermediate; d: distal. (**E**) Scheme of the protocol to culture *ex vivo* explants of mouse UGS harvested at E15.5. (**F**) Representative images of UGS explants at E15.5 (day 0), day 3, day 5 and day 7 of culture showing the formation of premature prostate buds. (**G**) Co-immunostaining of RUNX1, NKX3.1, CDH1 in UGS explants harvested at day 0, day 1, day 2 and day 7. Higher magnification images of each square (left) are shown for each time point. Chevron arrows show $RUNX1^{+}$ $NKX3.1^{+}$ cells, closed arrows indicate $RUNX1^{-}$ $NKX3.1^{+}$ cells, arrowheads show $RUNX1^{+}$ $NKX3.1^{-}$ cells. Scale bars: 200 µm (yellow) and 50 µm (white). (**H**) Quantification of RUNX1 and NKX3.1 nuclear intensity (log_{10}) in $CDH1^{+}$ epithelial cells of UGS explants by QBIC. Quantification was performed within the boundaries delimited in **G** by dotted lines, at day 0 (*n* = 3 explants), day 1 (*n* = 7 explants), day 2 (*n* = 6 explants) and day 7 (*n* = 6 explants). Source files are available in Figure 5—source data 1.

Figure 6. scRNA-seq of UGS explant cultures shows specification of the proximal luminal lineage during embryonic prostate development.

(**A**) Experimental strategy for scRNA-seq of UGS explant cultures at day 0, day 1, day 3 and day 6. (**B**, **C**) Force directed visualization of the developing prostatic epithelium in UGS explant cultures. In **B** cells are colored by experimental time points, and in **C** cells are colored by clusters. (**D**) PAGA representation of the clusters as in **C**. Weighted edges between cluster nodes represent a statistical measure of connectivity. (**E**) Fraction of cells per cluster at each experimental time point, displaying a progressive cellular diversification. (**F-H**) PAGA representations with cluster nodes colored by a gradient representing the mean log-normalized

expression levels of each gene. (**I**) Force directed visualization of the developing prostatic epithelium in UGS explant cultures. Color gradient represents AUC scores per cell. Per-cell AUC scores were calculated using the 'AUCell' package. Gene signatures for 'Lum-D' (left) and 'Basal' (right) were generated using the list of differentially upregulated genes previously obtained from our adult mouse prostate clusters.

Figure 7. RUNX1$^+$ cells contribute to the establishment of the proximal luminal lineage during embryonic prostate development.

(**A**) Strategy for lineage-tracing of RUNX1$^+$ cells in UGS explant cultures. Tamoxifen was applied on day 0 and day 1 and washed out on day 2. (**B, C**) Co-immunostaining of RFP, RUNX1, CDH1 in UGS explants harvested at day 2 (**B**) and day 7 (**C**). Higher magnification images of proximal (i) and (ii) distal regions are shown for day 7. Arrows show RFP$^+$ RUNX1-low cells, arrowheads show RFP$^+$ RUNX1$^+$ cells. Scale bars: 200 µm (yellow) and 50 µm (white). (**C**) Quantification of the percentage of epithelial RUNX1$^+$ cells in the RFP subset at day 2 (n = 7) and day 7 (n = 3) of UGS explant cultures. Quantification was performed within the boundaries delimited in **B** by dotted lines. (**E, F**) Co-immunostaining of RFP, NKX3.1, CDH1 in UGS explants harvested at day 2 (**E**) and day 7 (**F**). Higher magnification images of (i) proximal and (ii) distal regions are shown for day 7. Arrows show RFP$^+$ NKX3.1$^+$ cells, arrowheads show RFP$^+$ NKX3.1$^-$ cells. Scale bars: 200 µm (yellow) and 50 µm (white). (**G**) Quantification of the percentage of epithelial NKX3.1$^+$ cells in the RFP subset at day 2 (n = 6) and day 7 (n = 4) of UGS explant cultures. Quantification was performed within the boundaries delimited in **F** by dotted lines. (**H, I**) Co-immunostaining of RFP, K4, CDH1 in UGS explants harvested at day 2 (**H**) and day 7 (**I**). Higher magnification images

of (i) proximal and (ii) distal regions are shown for day 7. Arrows show RFP^+ K4 cells, arrowheads show RFP^+ $K4^+$ cells. Scale bars: 200 µm (yellow) and 50 µm (white). (**J**) Quantification of the percentage of epithelial $K4^+$ cells in the RFP subset at day 2 (*n* = 3) and day 7 (*n* = 3) of UGS explant cultures. Quantification was performed within the boundaries delimited in **I** by dotted lines. Source files are available in Figure 7—source data 1.

Figure 1—figure supplement 1. RUNX1 is enriched in the mouse prostate epithelium.

(**A**) Co-immunostaining of RUNX1, NKX3.1, CDH1 in the mouse DLP (top) and VP (bottom). Closed arrows indicate $RUNX1^+$ $NKX3.1^-$ cells, chevron arrows indicate rare $RUNX1^+$ $NKX3.1^+$ cells, arrowheads show $RUNX1^-$ $NKX3.1^+$ cells. Scale bars: 50 µm. (**B**) Quantification of RUNX1 and NKX3.1 nuclear intensity (log_{10}) in CDH1+ epithelial cells by QBIC in proximal DLP (*n* = 3), distal DLP (*n* = 8), proximal VP (*n* = 3) and distal VP (*n* = 8). (**C**) H&E staining of the mouse AP. Higher magnification images of (i) proximal AP and (ii) distal regions are shown. Arrows show typical proximal luminal cells with condensed nuclei and cytoplasm, arrowheads show typical distal secretory luminal cells with enlarged cytoplasm and strong pink eosinophilic staining. Scale bars: 200 µm (blue) and 50 µm (black). Source files are available in Figure 1—figure supplement 1—source data 1.

Figure 1—figure supplement 2. *Runx1* expression is mediated by the P2 promoter in the mouse prostate epithelium.

(**A**) Schematic diagrams of the P2-*Runx1*:RFP reporter allele (top), *Runx1* WT allele (middle), and P1-*Runx1*:GFP reporter allele (bottom). In P2-*Runx1*:RFP or P1-*Runx1*:GFP mice, expression of

RFP or GFP is directed by *Runx1* proximal P2 or distal P1 promoter respectively. WT *Runx1* expression is directed by the remaining WT allele. (**B**) Flow-cytometry analysis of the epithelial EPCAM$^+$ fraction of WT, P2-*Runx1*:RFP and P1-*Runx1*:GFP mice. Percentages are indicated in each quadrant gates. (**C**) Confocal images indicating P2-*Runx1*:RFP signal in the glandular epithelium (top), while P1-*Runx1*:GFP (bottom) activity is detected in the surrounding stroma. Scale bar: 50 µm. (**D**) Flow-cytometry analysis of P2-*Runx1*:RFP mice, and corresponding quantification of the percentages of RFP$^+$ and RFP$^-$ cells in the basal and luminal fractions of DLP (*n* = 4 mice) and VP (*n* = 4 mice) lobes. Source files are available in Figure 1—figure supplement 2—source data 1.

Figure 1—figure supplement 3. Characterization of P2Runx1:RFP derived mouse prostate organoids.

(**A**) Organoid Forming Capacity (OFC) of RFP$^+$ and RFP$^-$ basal and luminal sorted cells from DLP (left) and VP (right) cultured for 7 days. *n* = 4 mice. (**B**) Quantification of organoid morphologies determined by brightfield assessment. *p* values are indicated only for statistically significant ($p < 0.05$) comparisons between RFP$^+$ versus RFP$^-$ derived subsets. *n* = 4 mice. (**C**) Quantification of the type of organoids (pink: unipotent K5$^+$, green: unipotent K8$^+$, orange: multipotent K5$^+$ K8$^+$ organoids) characterized by whole-mount immunostaining. *p* value is indicated for the proportion of K5$^+$K8$^+$ organoids between VP Luminal RFP$^+$ versus RFP$^-$ derived subset. Other comparisons were not statistically significant. *n* = 2 mice. (**D**) Quantification of organoid morphologies according to the type of organoids (unipotent K5$^+$, unipotent K8$^+$, multipotent K5$^+$ K8$^+$). Results are shown for luminal proximal and distal AP derived organoids. *n* = 2 mice.

Numbers of organoids quantified are shown above the graph. Two-way ANOVA using Tukey's multiple comparisons test was used for statistical analysis. (**E**) Quantification of the organoid area estimated from maximum projection of stacked images from basal (left) and luminal (right) fractions of the proximal AP. Numbers of organoids quantified are shown above the graph. Two-tailed Mann-Whitney test was used for statistical analysis. *n* = 2 mice. Source files are available in Figure 1—figure supplement 3—source data 1.

Figure 2—figure supplement 1. Characterization of RUNX1 expression in the castrated mouse prostate.

(**A**) Flow cytometry analysis and corresponding quantifications of the basal and luminal EPCAM$^+$ fraction from AP, DLP and VP lobes of castrated P2-*Runx1*:RFP mice (*n* = 3). (**B, C**) Co-immunostaining of RUNX1, NKX3.1, CDH1 in castrated DLP (**B**) and VP (**C**) lobes. Scale bars: 50 µm (white). Source files are available in Figure 2—figure supplement 2—source data 1.

Figure 3—figure supplement 1. Pre-processing of the scRNA-seq dataset of adult intact and castrated mouse prostates.

(**A**) UMAP visualization in MULTI-seq barcodes space for each independent experiment (Run 1: left, Run 2: middle, Run 3: right) before (top) and after (bottom) quality control and barcode filtration (see Methods for details). (**B**) UMAP visualization of the integrated batch-corrected dataset (*n* = 4,499 cells from 3 independent experiments). Colors represent different clusters. (**C**) UMAP visualization of the integrated batch-corrected dataset split and colored by individual experiment (Run 1: left, Run 2: middle, Run 3: right). (**D**, **E**) Example key marker genes used for

cell type characterization. (**D**) UMAP visualization of the integrated batch-corrected dataset. Cells are colored by a gradient of log-normalized expression levels for each gene indicated. (**E**) Dot plot showing the expression of selected marker genes associated with each cluster. Cells corresponding to the prostatic clusters were kept for downstream analyses.

Figure 3—figure supplement 2. Characterization of the scRNA-seq prostate epithelial subset. (**A**-**D**) Number of cells present in the prostate epithelial subset. In **A** colors correspond to phenotypic sorted populations, in **B** treatment of origin, in **C** RFP FACS gate of origin, in **D** individual lobes. (**E, G**) UMAP visualization of prostate epithelial cells. Cells in **E** are colored by clusters. Clusters 0, 1 and 5 were merged together. In **F** and **G** colors represent phenotypic sorted populations. (**H-J**) Cells are colored by a gradient of log-normalized expression levels for each gene. Canonical epithelial markers are shown in **H**, luminal lineage markers in **I**, and basal lineage markers in **J**.

Figure 3—figure supplement 3. Characterization of the scRNA-seq prostate epithelial dataset. (**A**) Heatmap of the 10 most differentially upregulated genes per cluster. (**B**, **C**) Sankey diagrams summarizing the proportion of cells and between phenotypic groups. (**D**, **E**) Cells are colored by a gradient of log-normalized expression levels for each gene. (**D**) shows the expression of Ly6 family members, and in **E** RUNX family members are shown.

Figure 3—figure supplement 4. Gene Ontology and differential expression analysis within the scRNA-seq prostate epithelial dataset.

Bar plots of the 8 most significantly (g:Profiler adjusted p-value < 0.05) enriched gene ontology (GO) terms (GO:BP, Biological Processes) using the list of differentially upregulated genes specific to (**A**) Lum-A, (**B**) Lum-B, (**C**) Lum-C, (**D**) Lum-D, (**E**) Lum-E, (**F**) Lum-F, and (**G**) Basal clusters. (**H, I**) 15 most enriched GO terms (g:Profiler adjusted p-value < 0.05) for genes upregulated in the Lum-D cluster against combined Lum-A, Lum-B and Lum-C clusters in **H**. Results of the opposite comparison are shown in **I**. (**J**) Violin plots showing the expression levels of specific genes within the Lum-D cluster. Data are split and colored by treatment for each lobe. The expression of *Krt4*, *Tacstd2*/*Trop2* and *Runx1* does not vary upon treatment, while Androgen Receptor (AR) regulated genes such as *Psca* and *Tspan1* are downregulated after castration.

Figure 4—figure supplement 1. Lineage tracing of RUNX1 expressing cells labelled in intact mice.

(**A**) Scheme of the tamoxifen labelling strategy to evaluate the labelling efficiency of *Runx1* expressing cells. (**B**) Flow-cytometry analysis of intact (*n* = 2), castrated (*n* = 2), and regenerated (*n* = 2) *Runx1*^{CreER} *Rosa26*$^{LSL\text{-}RFP}$ mice, and corresponding quantification of the percentage of RFP$^+$ cells in the epithelial EPCAM$^+$ fraction. (**C**) Estimated absolute number of epithelial RFP$^+$ cells in intact (*n* = 5) and castrated (*n* = 5) and regenerated (*n* = 4) prostates based on IHC quantifications. Int: Intact, Cas: Castrated, Rgn: Regenerated. (**D**) Quantification of the percentage of epithelial RFP$^+$ cells being K4$^+$ or K4 in intact (*n* = 3), castrated (*n* = 4) and regenerated (*n* = 5) mice. (**F**) Co-immunostaining showing the enrichment of K4$^+$ RFP labelled

cells in the proximal region of the AP (top) and DLVP (bottom) prostate lobes. Scale bar: 50 µm. Source files are available in Figure 4—figure supplement 1—source data 1.

Figure 5—figure supplement 1. Characterization of RUNX1 expression during prostate development *in vivo*.

(**A**) Co-immunostainings of the mouse urogenital sinus at E18.5 for RUNX1, NKX3.1, K4. p: proximal, d: distal. Scale bar: 50 µm. Dotted lines indicate the urogenital epithelium. (**B**) Co-immunostainings of the mouse urogenital sinus at E18.5 for RUNX1, NKX3.1, LY6D. p: proximal, d: distal. Scale bar: 50 µm. (**C**) Co-immunostaining of RUNX1, NKX3.1, K4 at postnatal (P) day 14. Higher magnification images of (p) proximal, (i) intermediate, and (d) distal regions are shown. Scale bars: 200 µm (yellow) and 50 µm (white). (**D**, **E**) Co-immunostainings at P14 for RUNX1, K5, K8 in **B** RUNX1, p63, CDH1 in **C**. p: proximal, i: intermediate, d: distal. Scale bar: 50 µm.

Figure 5—figure supplement 2. Characterization of RUNX1 expression during prostate development in UGS explant cultures.

(**A**) Co-immunostaining of RUNX1, K5, K8 in UGS explants harvested at day 2 and day 7. p: proximal, d: distal. Scale bar: 50 µm. (**E**) Quantification of the percentage of $K5^+$, $K8^+$, $K5^+$ $K8^+$ cells during UGS explant cultures at day 0 (*n* = 2 explants), day 1 (*n* = 3 explants), day 2 (*n* = 3 explants), day 7 (*n* = 4 explants), showing a progressive reduction in the proportion of $K5^+$ $K8^+$ double positive cells. (**C**) Co-immunostaining of RUNX1, NKX3.1, LY6D in UGS explants harvested at day 7. p: proximal, d: distal. Scale bar: 50 µm. (**D**) Co-immunostaining of RUNX1, NKX3.1, K4 in UGS explants harvested at day 1 (top), 3 (middle) and 7 (bottom). Higher magnification

images of (p) proximal, (i) intermediate, and (d) distal regions are shown for day 7. Scale bars: 200 µm (yellow) and 50 µm (white). Dotted lines indicate the urogenital epithelium. (**E**) Co-immunostaining of RUNX1, Ki67, CDH1 in UGS explants harvested at day 2 and day 7. p: proximal, d: distal. Scale bar: 50 µm. Source files are available in Figure 5—figure supplement 2—source data 1.

Figure 6—figure supplement 1. Pre-processing of the scRNA-seq dataset of UGS explant cultures.

(**A**) UMAP visualization in MULTI-seq barcodes space before (top) and after (bottom) quality control and barcode filtration (see Methods for details). (**B**) UMAP visualization of the dataset colored by estimated cell cycle phase (top). Due to the strong underlying impact on clustering, the cell cycle effect was regressed out (bottom). (**C, D**) UMAP visualization of the dataset colored in **C** by experimental time point and in **D** by labeled populations. (**E**) Dot plot showing the expression of selected marker genes associated with each labelled population. (**F**) Bar plots of the 10 most significantly (g:Profiler adjusted p-value < 0.05) enriched gene ontology (GO) terms (GO:BP, Biological Processes) on the differentially upregulated genes specific to the 'Hypoxic/Stressed' cluster. (**G**-**I**) UMAP visualization of the prostatic subset (from **D**), labelled by time points in **G**, clusters in **H**, estimated cell cycle phase in **I**. (**J**) Percentage of cells in the different estimated cell cycle phases in each clusters. (**K**) Diffusion maps representation of the prostatic subset using the first 2 diffusion components with (top) and without C9 (bottom). C9 was excluded for downstream analyses due to its outlying profile.

Figure 6—figure supplement 2. Characterization of the developing prostatic epithelium in the scRNA-seq dataset of UGS explant culture.

(**A**) Heatmap of the 10 most differentially upregulated genes per cluster. (**B**-**E**) PAGA representations with cluster nodes colored by a gradient representing the mean log-normalized expression levels of each genes indicated. (**B**) shows the expression of common prostate lineage markers, (**C**) shows known regulators of prostate development, (**D**) shows basal markers, (**E**) shows proliferation markers. (**F**) Box plots of per-cell AUC signature scores calculated using the 'AUCell' package for individual UGS explant clusters. Gene signatures were generated using the list of differentially upregulated genes previously obtained from our adult mouse prostate clusters. (**G**) Force directed visualization of the developing prostatic epithelium in UGS explant cultures. Color gradient represents AUC scores per cell.

Figure 7—figure supplement 1. Lineage-tracing of RUNX1 expressing cells in UGS explants.

(**A, B**) Co-immunostaining of RFP, p63, CDH1 in UGS explants harvested at day 2 (**A**) and day 7 (**B**). Higher magnification images of (i) proximal and (ii) distal regions are shown for day 7. Arrows show RFP^+ $p63^+$ cells, arrowheads show RFP^+ $p63^-$ cells. Scale bars: 200 µm (yellow) and 50 µm (white). (**C**) Quantification of the percentage of epithelial RFP^+ $p63^+$ cells at day 2 (n = 7) and day 7 (n = 4) of UGS explant cultures. Quantification was performed within the boundaries delimited in **B** by dotted lines. (**D**) Co-immunostaining of RFP, K5, K8 in UGS explants harvested at day 2 (top) and day 7 (bottom). Higher magnification images of proximal (i) and (ii) distal regions are shown for day 7. Arrows show RFP^+ $K5^+$ $K8^+$ cells, chevron arrows show RFP^+ $K5^-$ $K8^+$, arrowheads show RFP^+ $K5^+$ $K8^-$ cells. Scale bars: 200 µm (yellow) and 50 µm (white).

(**E**) Quantification of the percentage of epithelial $K5^+$ $K8^+$, $K5^-$ $K8^+$ cells and $K5^+$ $K8^-$ cells in the RFP subset at day 2 (*n* = 4) and day 7 (*n* = 3) of UGS explant cultures. Quantifications were performed within the boundaries delimited in **D** by dotted lines. (**F, G**) Co-immunostaining of RFP, *Nupr1* (mRNA), CDH1 in UGS explants harvested at day 2 (**F**) and day 7 (**G**). Higher magnification images of (i) proximal and (ii) distal regions are shown for day 7. Arrows show RFP^+ $Nupr1^+$ cells, arrowheads show RFP^+ $Nupr1^-$ cells. Scale bars: 200 µm (yellow) and 50 µm (white). **(J)** Quantification of the percentage of epithelial $K4^+$ cells in the RFP subset at day 2 (*n* = 3) and day 7 (*n* = 4) of UGS explant cultures. Quantification was performed within the boundaries delimited in **G** by dotted lines. Source files are available in Figure 7—figure supplement 1—source data 1.

FIGURE SUPPLEMENTS

Figure 1—figure supplement 1. RUNX1 is enriched in the mouse prostate epithelium.

Figure 1—figure supplement 2. *Runx1* expression is mediated by the P2 promoter in the mouse prostate epithelium.

Figure 1—figure supplement 3. Characterization of P2-*Runx1*:RFP derived mouse prostate organoids.

Figure 2—figure supplement 1. Characterization of RUNX1 expression in the castrated mouse prostate.

Figure 3—figure supplement 1. Pre-processing of the scRNA-seq dataset of adult intact and castrated mouse prostates.

Figure 3—figure supplement 2. Characterization of the scRNA-seq prostate epithelial subset.

Figure 3—figure supplement 3. Characterization of the scRNA-seq prostate epithelial dataset.

Figure 3—figure supplement 4. Gene Ontology and differential expression analysis within the scRNA-seq prostate epithelial dataset.

Figure 4—figure supplement 1. Lineage tracing of RUNX1 expressing cells labelled in intact mice.

Figure 5—figure supplement 1. Characterization of RUNX1 expression during prostate development *in vivo*.

Figure 5—figure supplement 2. Characterization of RUNX1 expression during prostate development in UGS explant cultures.

Figure 6—figure supplement 1. Pre-processing of the scRNA-seq dataset of UGS explant cultures.

Figure 6—figure supplement 2. Characterization of the developing prostatic epithelium in the scRNA-seq dataset of UGS explant culture.

Figure 7—figure supplement 1. Lineage-tracing of RUNX1 expressing cells in UGS explants.

SUPPLEMENTARY FILES

Supplementary file 1. Quality control metrics and metadata of scRNAseq experiments

Supplementary file 2. Genes differentially expressed between adult clusters

Supplementary file 3. Genes differentially expressed in intact versus castrated Lum-D cells

Supplementary file 4. Genes differentially expressed between UGS explants clusters

Supplementary file 5. Gene lists used for the analysis of gene set activity

SOURCE DATA FILES

Figure 1. source data 1.xlsx

Figure 1. figure supplement 1. source data1 .xlsx

Figure 1. figure supplement 2. source data1 .xlsx

Figure 1. figure supplement 3. source data 1.xlsx

Figure 2. figure supplement 1. source data 1.xlsx

Figure 2. source data 1.xlsx

Figure 4. source data 1.xlsx

Figure 4. figure supplement 1. source data 1.xlsx

Figure 5. figure supplement 2. source data 1.xlsx

Figure 5. source data 1.xlsx

Figure 7 - figure supplement 1. source data 1.xlsx

Figure 7 - source data 1.xlsx

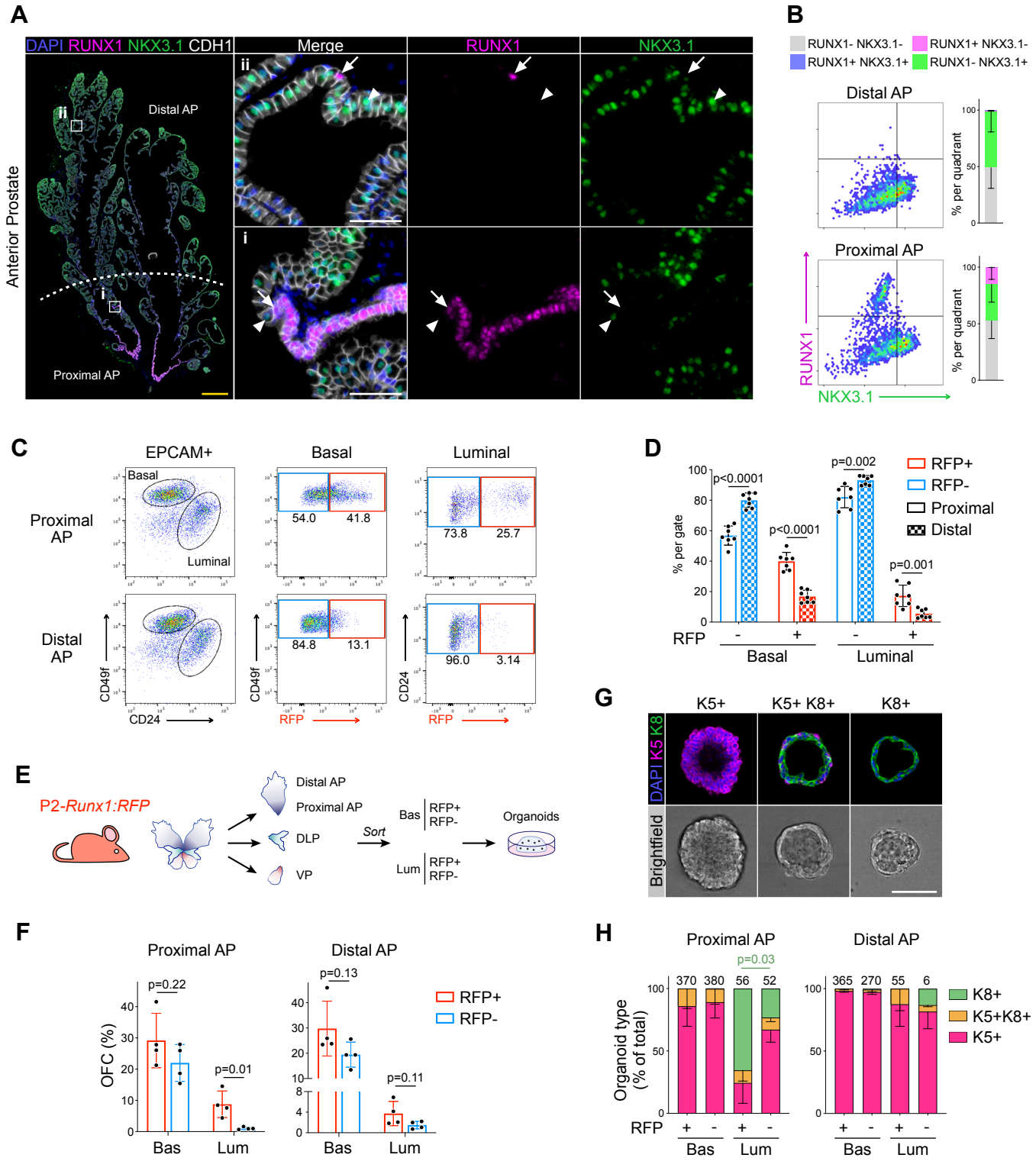
A
DAPI RUNX1 NKX3.1 CDH1
Merge
RUNX1
NKX3.1
Anterior Prostate
Distal AP
Proximal AP
ii
i
B
RUNX1- NKX3.1-
RUNX1+ NKX3.1-
RUNX1+ NKX3.1+
RUNX1- NKX3.1+
Distal AP
Proximal AP
% per quadrant
RUNX1
NKX3.1
C
EPCAM+
Basal
Luminal
Proximal AP
Distal AP
54.0
41.8
73.8
25.7
84.8
13.1
96.0
3.14
CD49f
CD24
RFP
D
p<0.0001
p<0.0001
p=0.002
p=0.001
% per gate
RFP+
RFP-
Proximal
Distal
RFP
Basal
Luminal
E
P2-Runx1:RFP
Distal AP
Proximal AP
DLP
VP
Sort
Bas
RFP+
RFP-
Lum
Organoids
F
Proximal AP
Distal AP
p=0.22
p=0.01
p=0.13
p=0.11
OFC (%)
RFP+
RFP-
Bas
Lum
G
K5+
K5+ K8+
K8+
DAPI K5 K8
Brightfield
H
Proximal AP
Distal AP
p=0.03
370
380
56
52
365
270
55
6
Organoid type (% of total)
K8+
K5+K8+
K5+
RFP
Bas
Lum

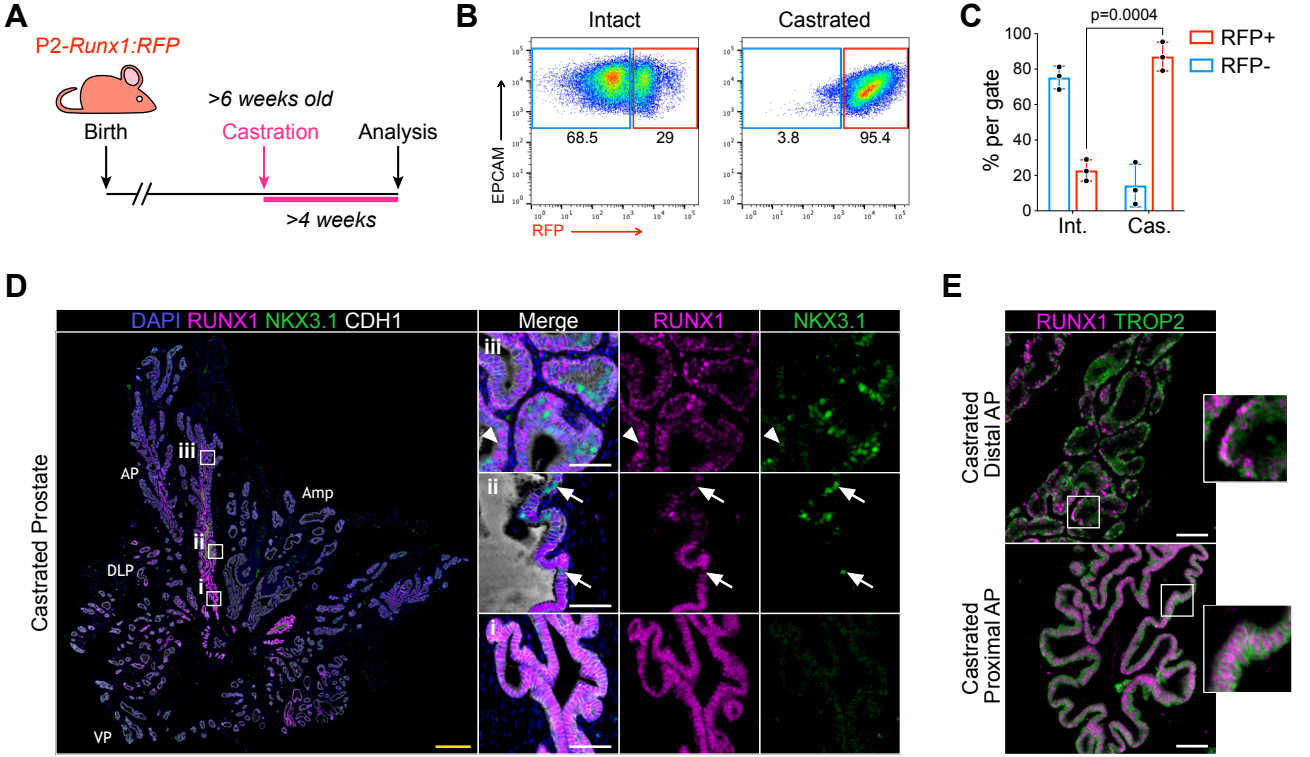
A
P2-Runx1:RFP
>6 weeks old
Birth
Castration
Analysis
>4 weeks
B
Intact
Castrated
EPCAM
RFP
68.5
29
3.8
95.4
C
p=0.0004
RFP+
RFP-
% per gate
Int.
Cas.
D
DAPI RUNX1 NKX3.1 CDH1
Merge
RUNX1
NKX3.1
Castrated Prostate
AP
Amp
DLP
VP
iii
ii
i
E
RUNX1 TROP2
Castrated Distal AP
Castrated Proximal AP

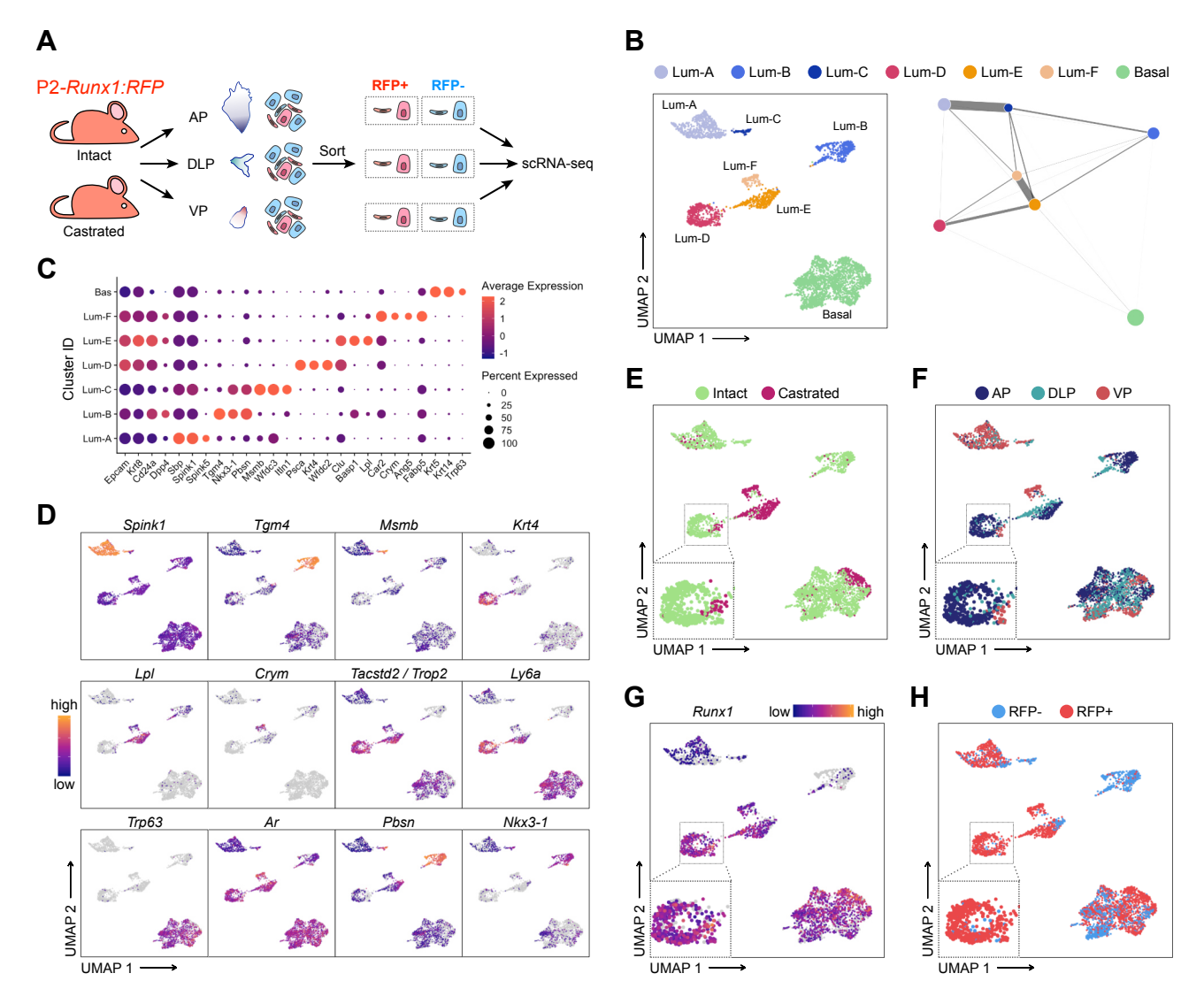
A
P2-Runx1:RFP
Intact
Castrated
AP
DLP
VP
Sort
RFP+
RFP-
scRNA-seq
B
Lum-A
Lum-B
Lum-C
Lum-D
Lum-E
Lum-F
Basal
UMAP 1
UMAP 2
C
Cluster ID
Bas
Lum-F
Lum-E
Lum-D
Lum-C
Lum-B
Lum-A
Average Expression
Percent Expressed
Epcam
Krt8
Cd24a
Dpp4
Sbp
Spink1
Spink5
Tgm4
Nkx3-1
Pbsn
Msmb
Wfdc3
Ifitm1
Psca
Krt4
Wfdc2
Clu
Basp1
Lpl
Car2
Crym
Aqp5
Fabp5
Krt5
Krt14
Trp63
D
Spink1
Tgm4
Msmb
Krt4
Lpl
Crym
Tacstd2 / Trop2
Ly6a
high
low
Trp63
Ar
Pbsn
Nkx3-1
UMAP 2
UMAP 1
E
Intact
Castrated
F
AP
DLP
VP
G
Runx1
low
high
H
RFP-
RFP+

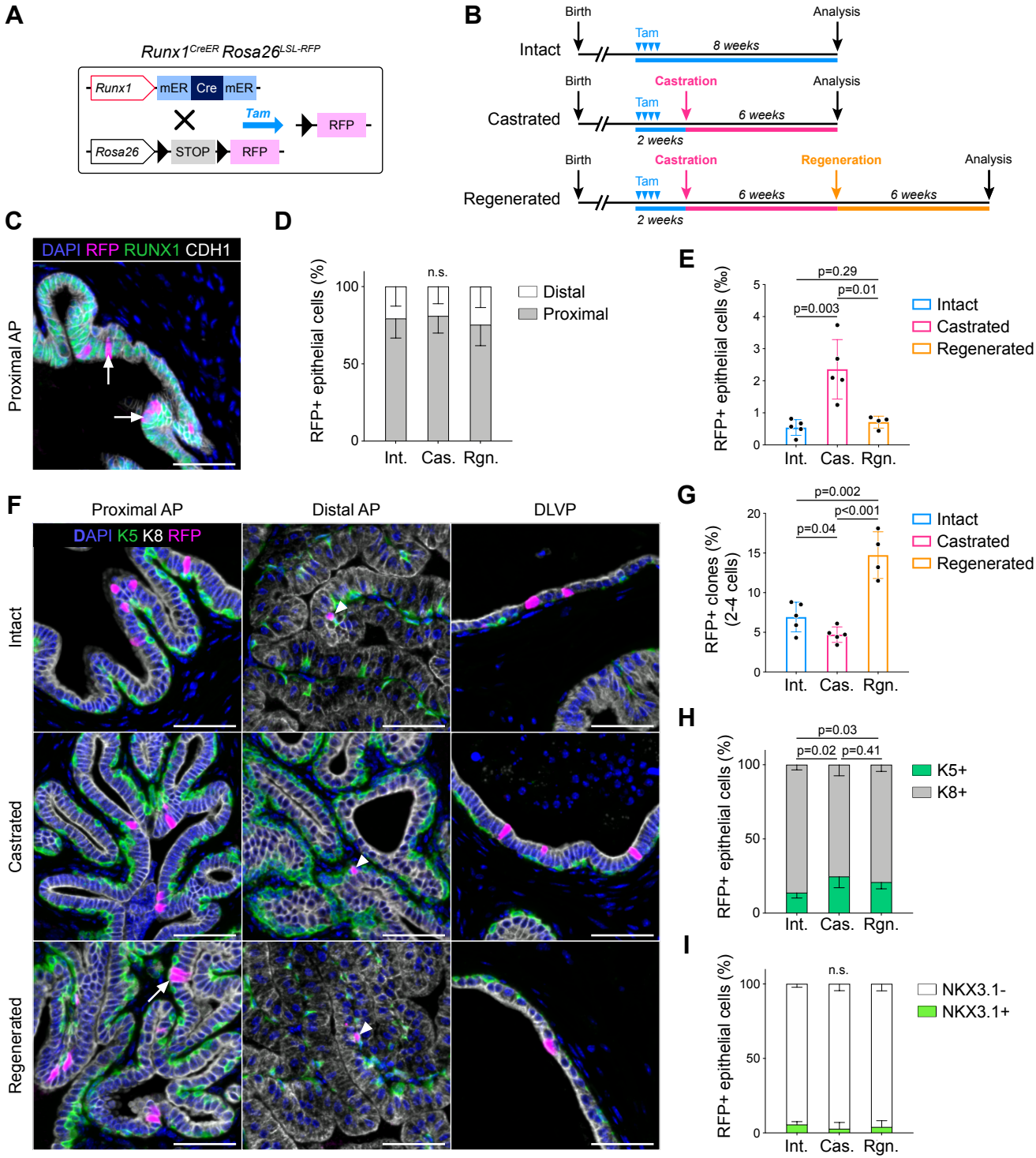
A
Runx1CreER Rosa26LSL-RFP
Runx1
mER
Cre
mER
Tam
RFP
Rosa26
STOP
RFP
B
Birth
Analysis
Intact
Tam
8 weeks
Birth
Castration
Analysis
Castrated
Tam
6 weeks
2 weeks
Birth
Castration
Regeneration
Analysis
Regenerated
Tam
6 weeks
6 weeks
2 weeks
C
DAPI RFP RUNX1 CDH1
Proximal AP
D
RFP+ epithelial cells (%)
n.s.
Distal
Proximal
Int.
Cas.
Rgn.
E
RFP+ epithelial cells (‰)
p=0.29
p=0.01
p=0.003
Intact
Castrated
Regenerated
Int.
Cas.
Rgn.
F
Proximal AP
Distal AP
DLVP
DAPI K5 K8 RFP
Intact
Castrated
Regenerated
G
RFP+ clones (%) (2-4 cells)
p=0.002
p<0.001
p=0.04
Intact
Castrated
Regenerated
Int.
Cas.
Rgn.
H
RFP+ epithelial cells (%)
p=0.03
p=0.02
p=0.41
K5+
K8+
Int.
Cas.
Rgn.
I
RFP+ epithelial cells (%)
n.s.
NKX3.1-
NKX3.1+
Int.
Cas.
Rgn.

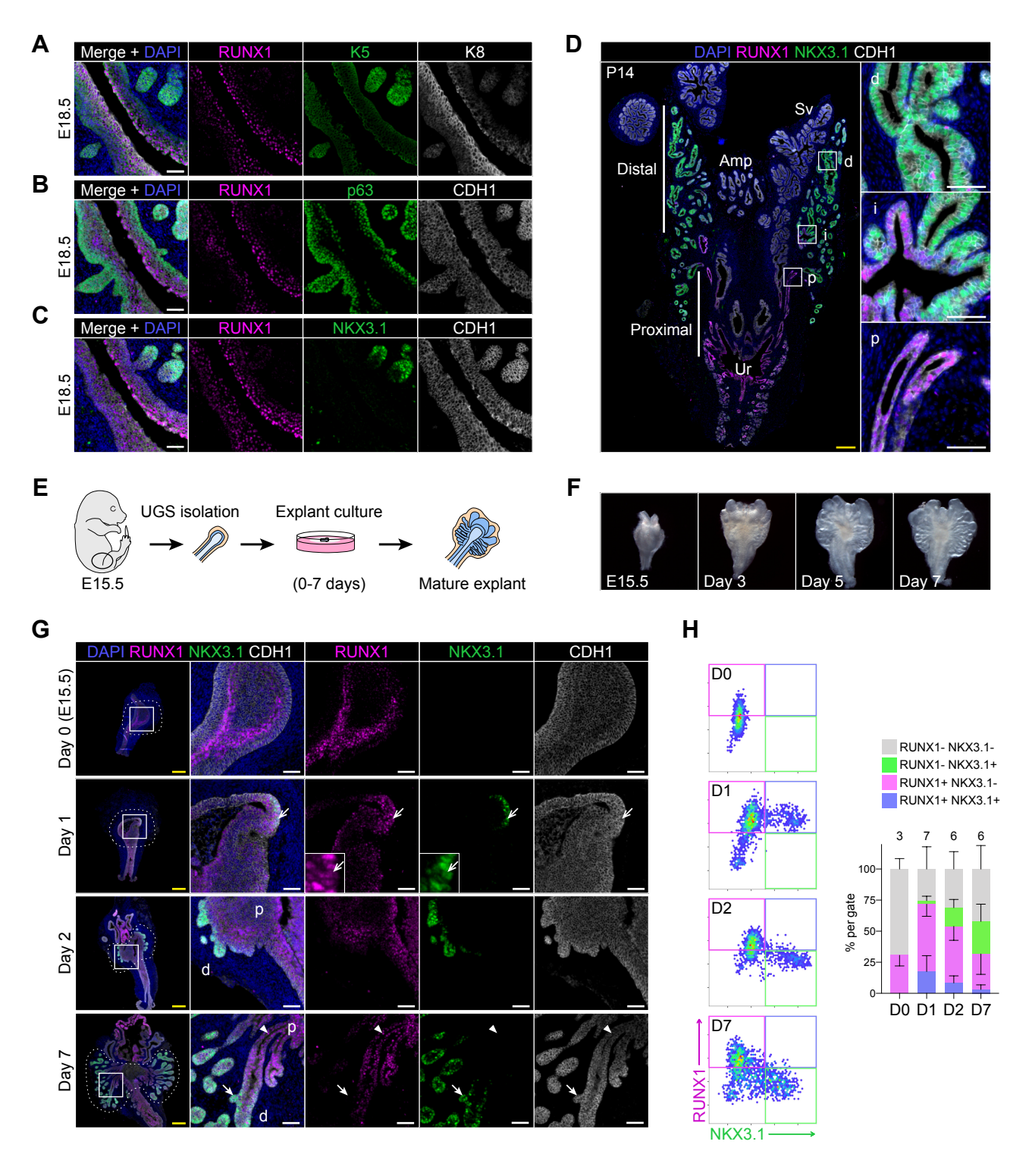
A
Merge + DAPI
RUNX1
K5
K8
E18.5
B
Merge + DAPI
RUNX1
p63
CDH1
E18.5
C
Merge + DAPI
RUNX1
NKX3.1
CDH1
E18.5
D
DAPI RUNX1 NKX3.1 CDH1
P14
Distal
Amp
Sv
Proximal
Ur
d
i
p
E
UGS isolation
Explant culture
E15.5
(0-7 days)
Mature explant
F
E15.5
Day 3
Day 5
Day 7
G
DAPI RUNX1 NKX3.1 CDH1
RUNX1
NKX3.1
CDH1
Day 0 (E15.5)
Day 1
Day 2
Day 7
p
d
H
D0
D1
D2
D7
RUNX1
NKX3.1
RUNX1- NKX3.1-
RUNX1- NKX3.1+
RUNX1+ NKX3.1-
RUNX1+ NKX3.1+
3
7
6
6
% per gate
100
75
50
25
0
D0 D1 D2 D7

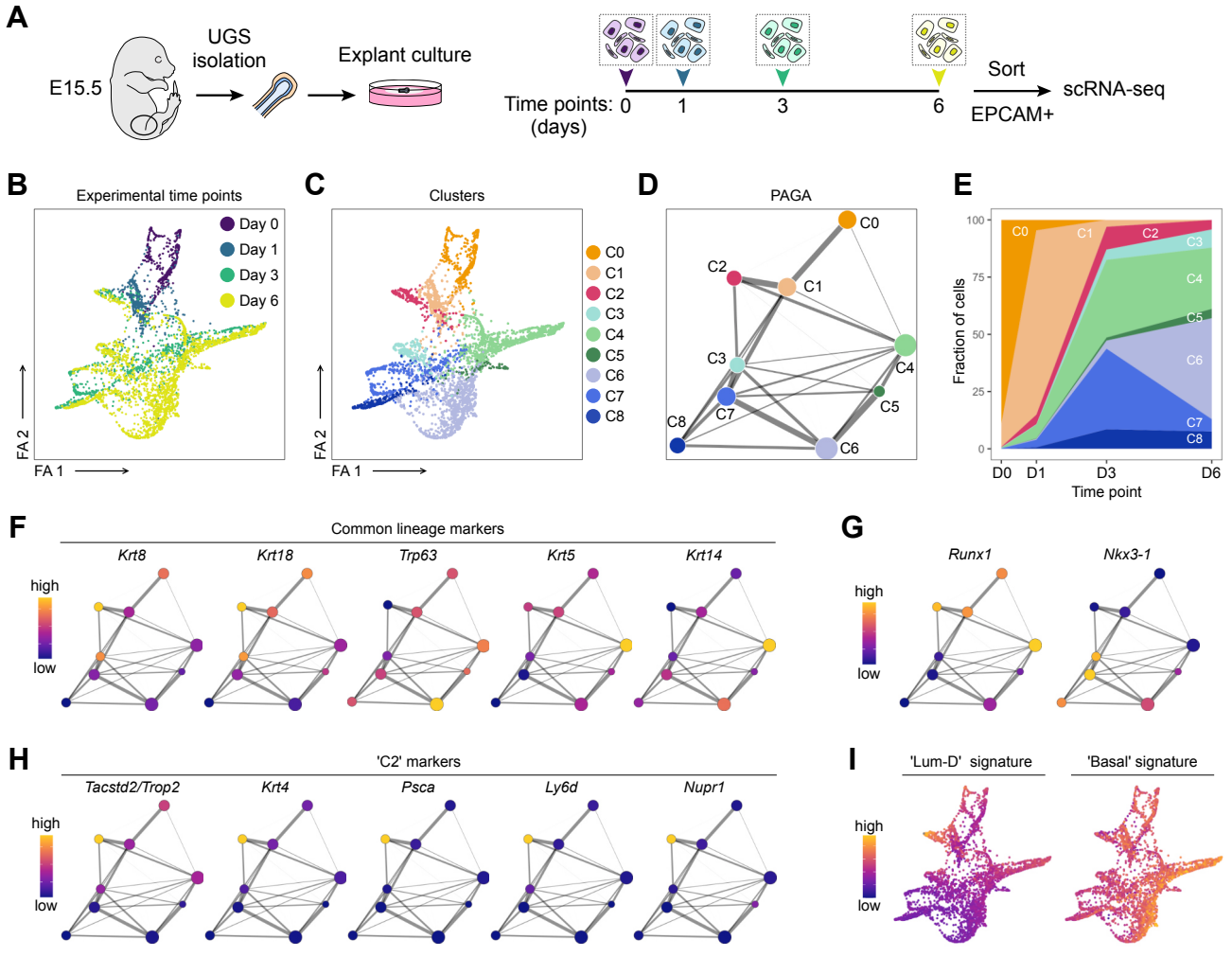
A
E15.5
UGS isolation
Explant culture
Time points: (days)
0
1
3
6
Sort
EPCAM+
scRNA-seq
B
Experimental time points
Day 0
Day 1
Day 3
Day 6
FA 1
FA 2
C
Clusters
C0
C1
C2
C3
C4
C5
C6
C7
C8
D
PAGA
E
Fraction of cells
Time point
D0
D1
D3
D6
F
Common lineage markers
Krt8
Krt18
Trp63
Krt5
Krt14
high
low
G
Runx1
Nkx3-1
H
'C2' markers
Tacstd2/Trop2
Krt4
Psca
Ly6d
Nupr1
I
'Lum-D' signature
'Basal' signature

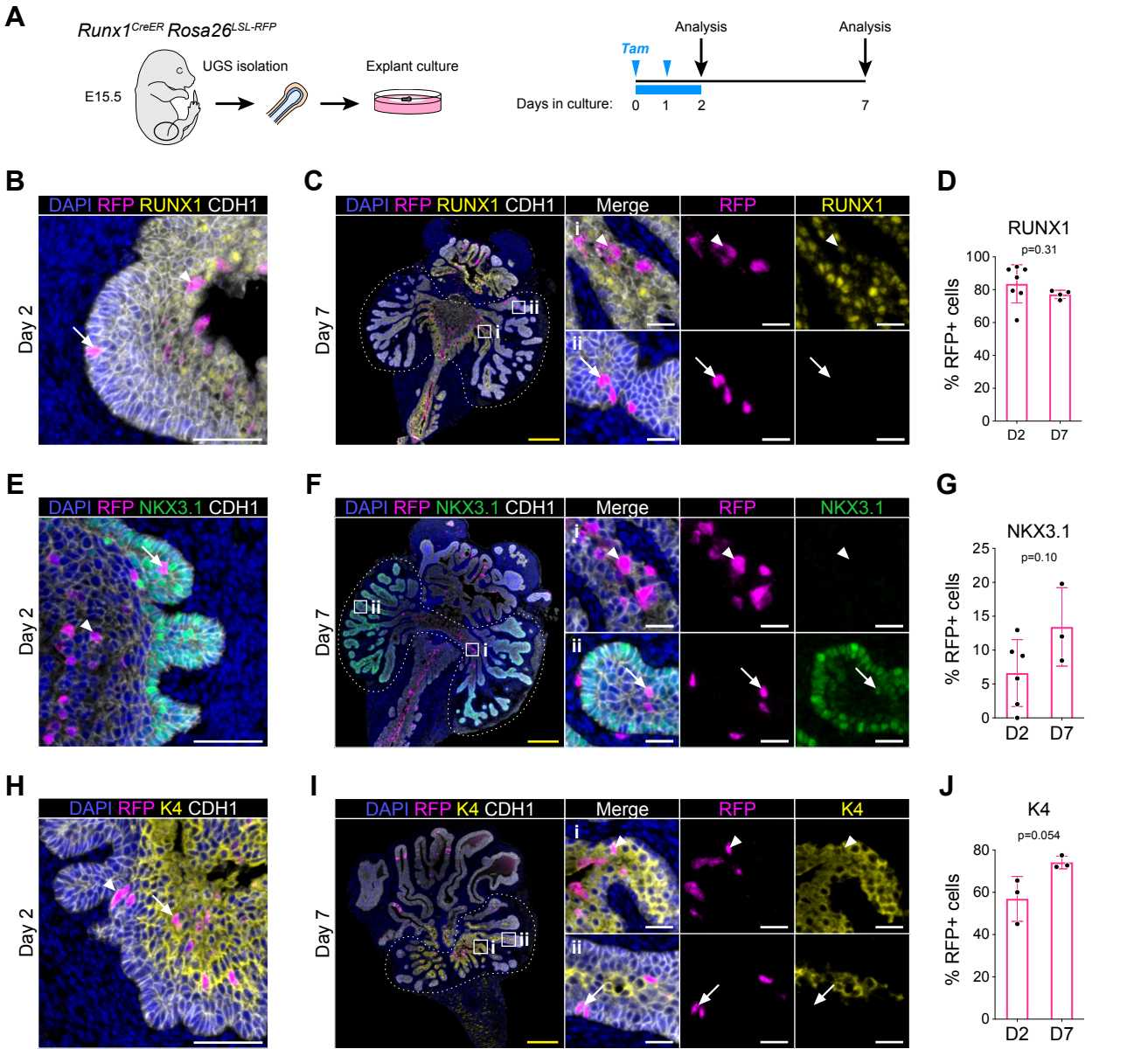
A
Runx1CreER Rosa26LSL-RFP
E15.5
UGS isolation
Explant culture
Tam
Analysis
Analysis
Days in culture:
0
1
2
7
B
DAPI RFP RUNX1 CDH1
Day 2
C
DAPI RFP RUNX1 CDH1
Merge
RFP
RUNX1
Day 7
i
ii
D
RUNX1
p=0.31
% RFP+ cells
100
80
60
40
20
0
D2
D7
E
DAPI RFP NKX3.1 CDH1
Day 2
F
DAPI RFP NKX3.1 CDH1
Merge
RFP
NKX3.1
Day 7
G
NKX3.1
p=0.10
% RFP+ cells
25
20
15
10
5
0
D2
D7
H
DAPI RFP K4 CDH1
Day 2
I
DAPI RFP K4 CDH1
Merge
RFP
K4
Day 7
J
K4
p=0.054
% RFP+ cells
80
60
40
20
0
D2
D7

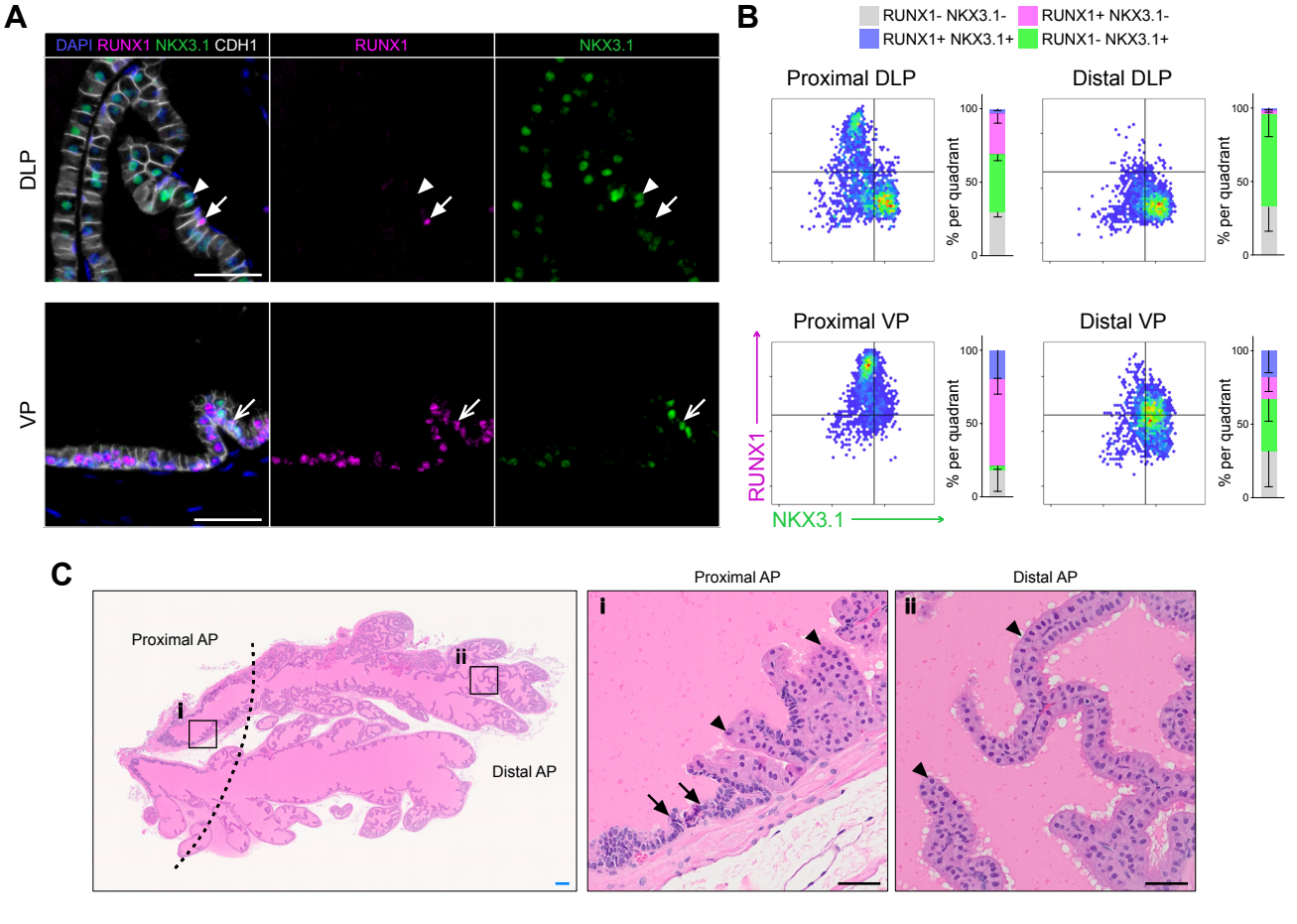
A
DAPI RUNX1 NKX3.1 CDH1
RUNX1
NKX3.1
DLP
VP
B
RUNX1- NKX3.1-
RUNX1+ NKX3.1-
RUNX1+ NKX3.1+
RUNX1- NKX3.1+
Proximal DLP
Distal DLP
Proximal VP
Distal VP
% per quadrant
100
50
0
RUNX1
NKX3.1
C
Proximal AP
Distal AP
i
ii

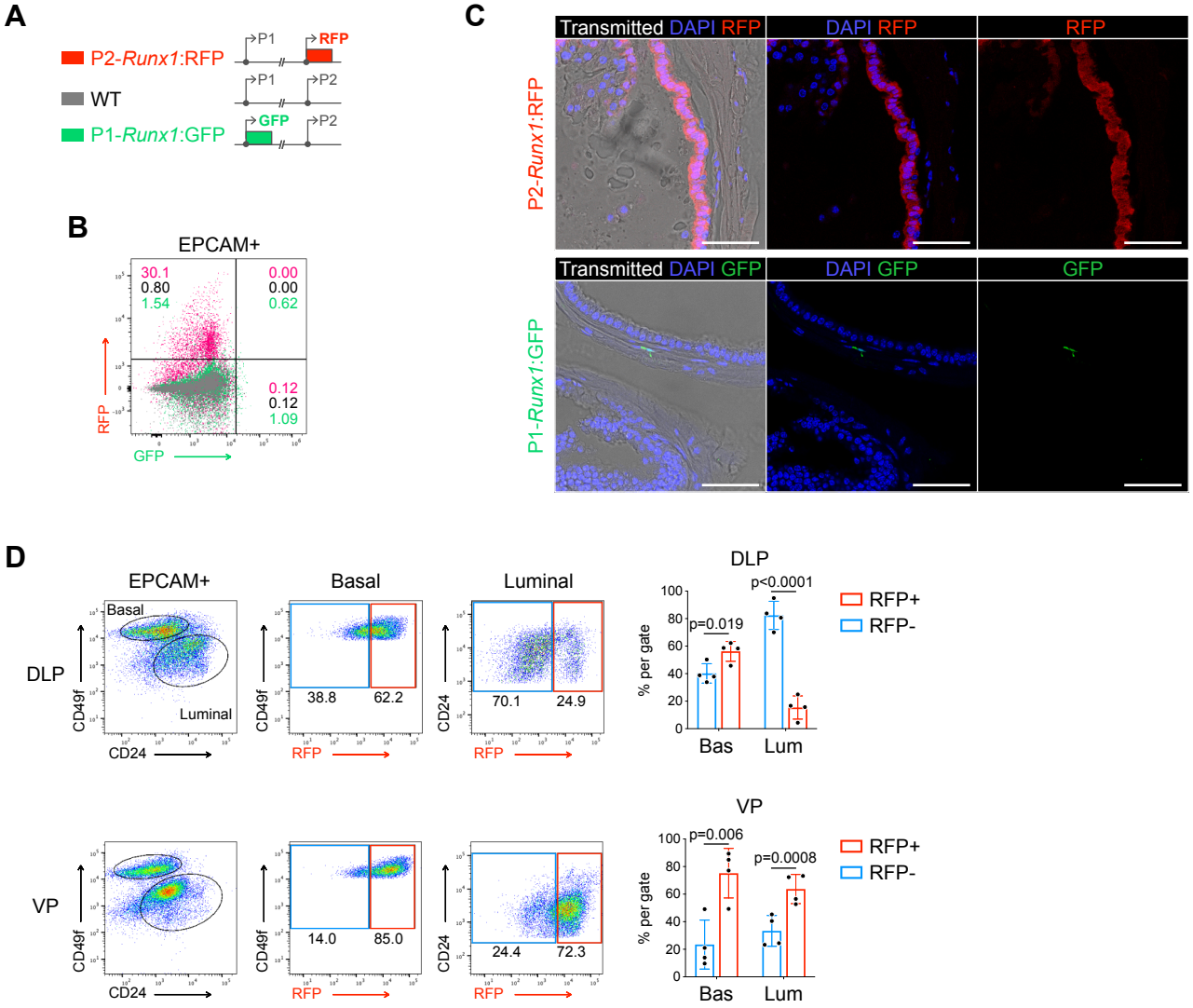
A
P2-Runx1:RFP
WT
P1-Runx1:GFP
P1
RFP
P2
GFP
B
EPCAM+
30.1
0.80
1.54
0.00
0.00
0.62
0.12
0.12
1.09
RFP
GFP
C
Transmitted DAPI RFP
DAPI RFP
RFP
P2-Runx1:RFP
Transmitted DAPI GFP
DAPI GFP
GFP
P1-Runx1:GFP
D
EPCAM+
Basal
Luminal
DLP
CD49f
CD24
38.8
62.2
70.1
24.9
RFP
VP
14.0
85.0
24.4
72.3
% per gate
p=0.019
p<0.0001
p=0.006
p=0.0008
Bas
Lum
RFP+
RFP-

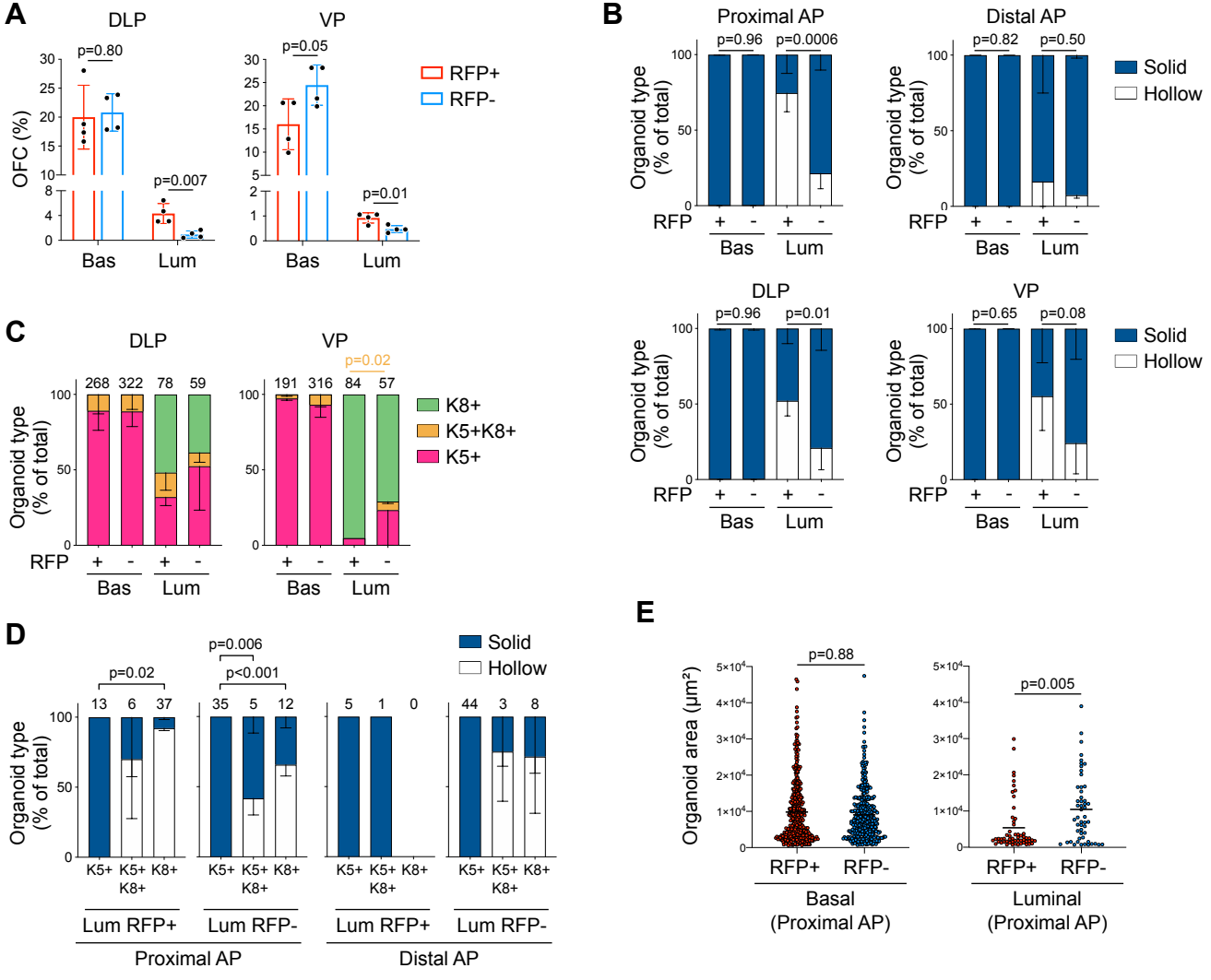
A
DLP
VP
p=0.80
p=0.05
p=0.007
p=0.01
OFC (%)
RFP+
RFP-
Bas
Lum
B
Proximal AP
Distal AP
p=0.96
p=0.0006
p=0.82
p=0.50
Organoid type (% of total)
Solid
Hollow
RFP
Bas
Lum
p=0.96
p=0.01
p=0.65
p=0.08
C
DLP
VP
p=0.02
268 322 78 59
191 316 84 57
K8+
K5+K8+
K5+
D
p=0.02
p=0.006
p<0.001
13 6 37
35 5 12
5 1 0
44 3 8
K5+ K5+ K8+ K8+
Lum RFP+
Lum RFP-
Proximal AP
Distal AP
E
Organoid area (µm²)
p=0.88
p=0.005
RFP+
RFP-
Basal (Proximal AP)
Luminal (Proximal AP)

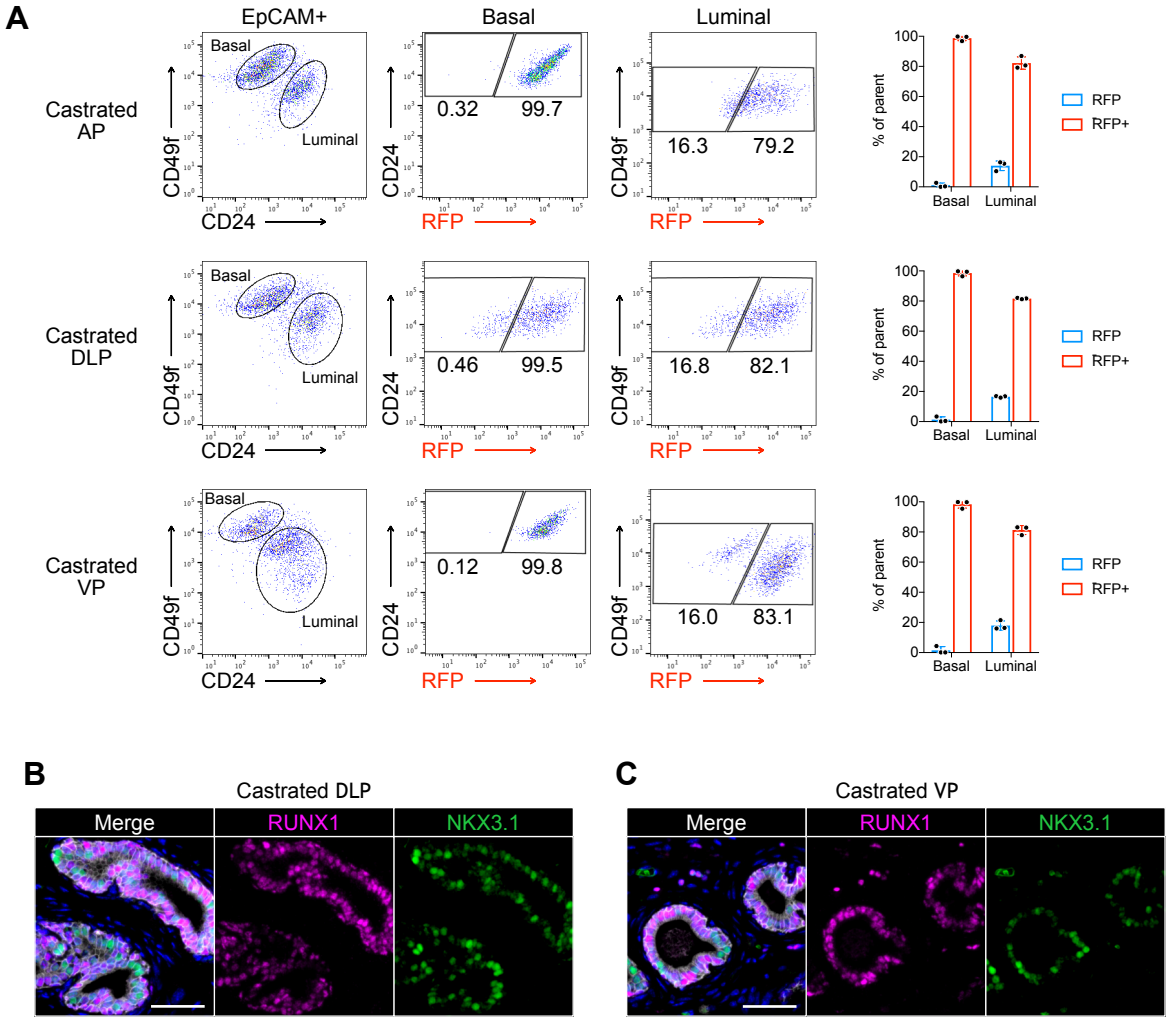
A
EpCAM+
Basal
Luminal
Castrated AP
Castrated DLP
Castrated VP
Basal
Luminal
CD49f
CD24
0.32
99.7
16.3
79.2
0.46
99.5
16.8
82.1
0.12
99.8
16.0
83.1
RFP
% of parent
RFP
RFP+
B
Castrated DLP
C
Castrated VP
Merge
RUNX1
NKX3.1

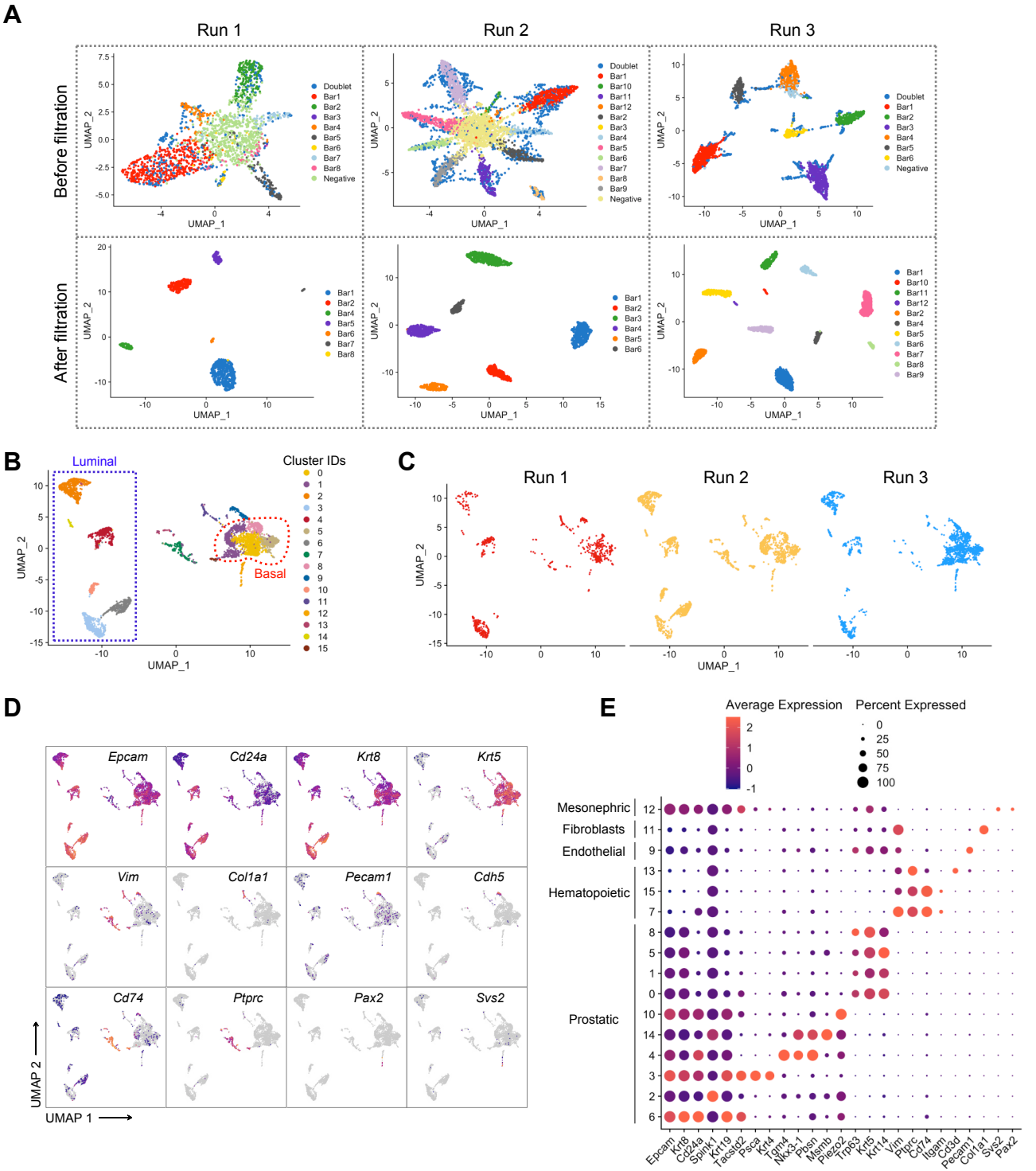
A
Run 1
Run 2
Run 3
Before filtration
After filtration
UMAP_1
UMAP_2
Doublet
Bar1
Bar2
Bar3
Bar4
Bar5
Bar6
Bar7
Bar8
Bar9
Bar10
Bar11
Bar12
Negative
B
Luminal
Basal
Cluster IDs
C
D
Epcam
Cd24a
Krt8
Krt5
Vim
Col1a1
Pecam1
Cdh5
Cd74
Ptprc
Pax2
Svs2
UMAP 2
UMAP 1
E
Average Expression
Percent Expressed
Mesonephric
Fibroblasts
Endothelial
Hematopoietic
Prostatic
Epcam
Krt8
Cd24a
Sphk1
Krt19
Tacstd2
Psca
Krt4
Tgm4
Nkx3.1
Ppsn
Msmb
Piezo2
Trp63
Krt5
Krt14
Vim
Ptprc
Cd74
Itgam
Cd3d
Pecam1
Col1a1
Svs2
Pax2

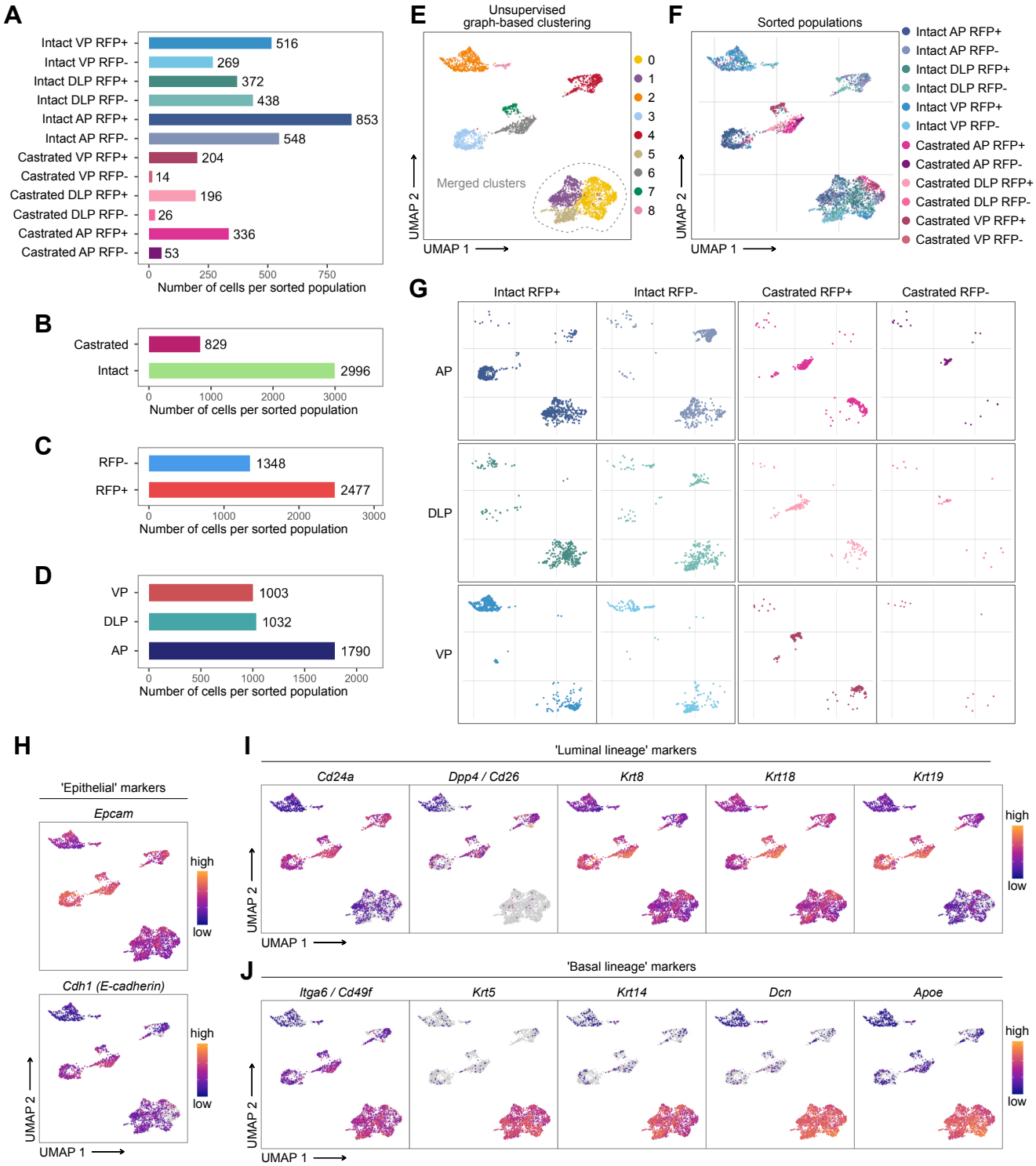
A
Intact VP RFP+ 516
Intact VP RFP- 269
Intact DLP RFP+ 372
Intact DLP RFP- 438
Intact AP RFP+ 853
Intact AP RFP- 548
Castrated VP RFP+ 204
Castrated VP RFP- 14
Castrated DLP RFP+ 196
Castrated DLP RFP- 26
Castrated AP RFP+ 336
Castrated AP RFP- 53
0 250 500 750
Number of cells per sorted population
B
Castrated 829
Intact 2996
0 1000 2000 3000
Number of cells per sorted population
C
RFP- 1348
RFP+ 2477
0 1000 2000 3000
Number of cells per sorted population
D
VP 1003
DLP 1032
AP 1790
0 500 1000 1500 2000
Number of cells per sorted population
E
Unsupervised graph-based clustering
Merged clusters
0 1 2 3 4 5 6 7 8
UMAP 2
UMAP 1
F
Sorted populations
Intact AP RFP+
Intact AP RFP-
Intact DLP RFP+
Intact DLP RFP-
Intact VP RFP+
Intact VP RFP-
Castrated AP RFP+
Castrated AP RFP-
Castrated DLP RFP+
Castrated DLP RFP-
Castrated VP RFP+
Castrated VP RFP-
UMAP 2
UMAP 1
G
Intact RFP+
Intact RFP-
Castrated RFP+
Castrated RFP-
AP
DLP
VP
H
'Epithelial' markers
Epcam
Cdh1 (E-cadherin)
high
low
UMAP 2
UMAP 1
I
'Luminal lineage' markers
Cd24a
Dpp4 / Cd26
Krt8
Krt18
Krt19
high
low
UMAP 2
UMAP 1
J
'Basal lineage' markers
Itga6 / Cd49f
Krt5
Krt14
Dcn
Apoe
high
low
UMAP 2
UMAP 1

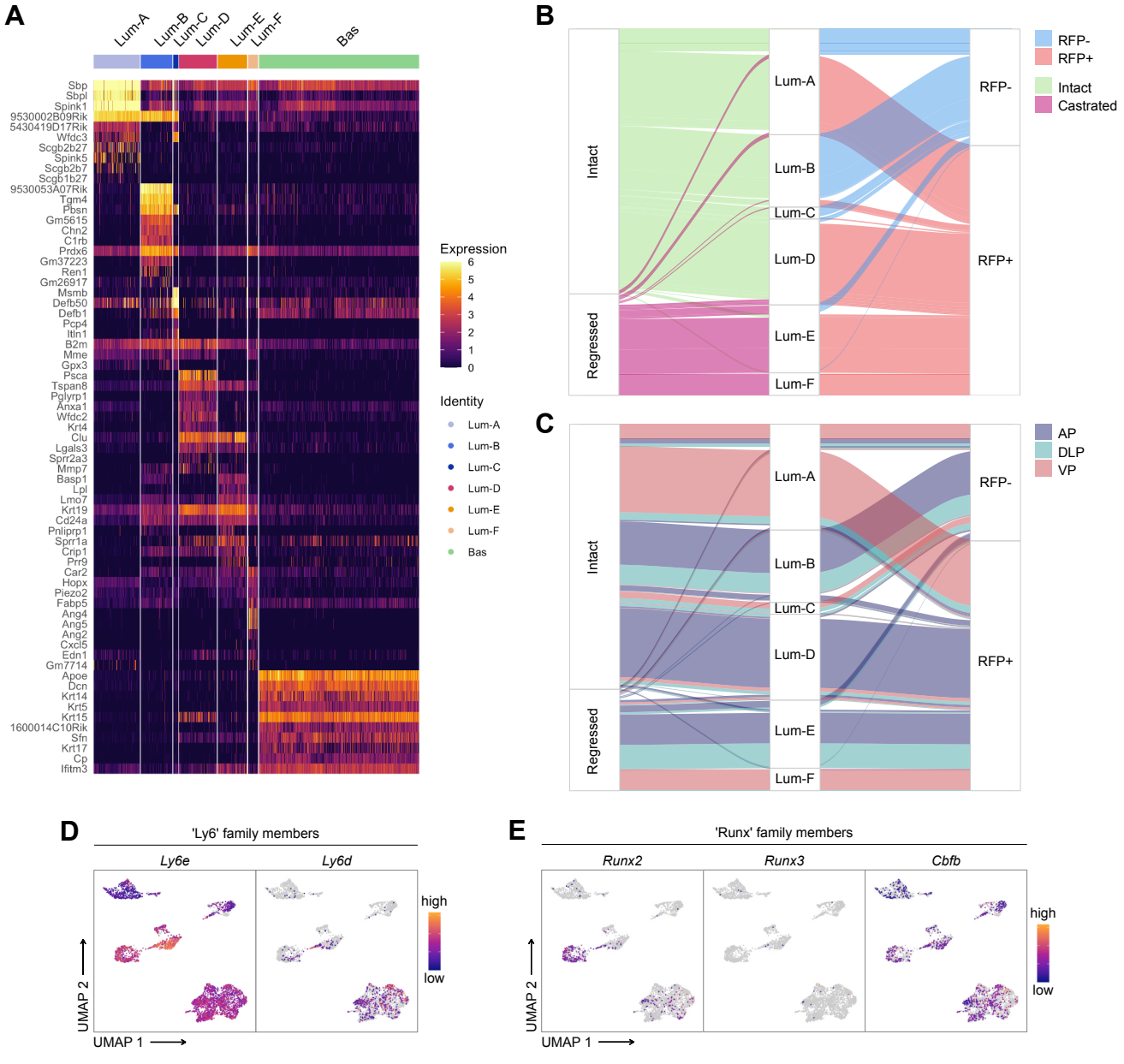
A
Lum-A
Lum-B
Lum-C
Lum-D
Lum-E
Lum-F
Bas
Sbp
Sbpl
Spink1
9530002B09Rik
5430419D17Rik
Wfdc3
Scgb2b27
Spink5
Scgb2b7
Scgb1b27
9530053A07Rik
Tgm4
Pbsn
Gm5615
Chn2
C1rb
Prdx6
Gm37223
Ren1
Gm26917
Msmb
Defb50
Defb1
Pcp4
Itln1
B2m
Mme
Gpx3
Psca
Tspan8
Pglyrp1
Anxa1
Wfdc2
Krt4
Clu
Lgals3
Sprr2a3
Mmp7
Basp1
Lpl
Lmo7
Krt19
Cd24a
Pnliprp1
Sprr1a
Crip1
Prr9
Car2
Hopx
Piezo2
Fabp5
Ang4
Ang5
Ang2
Cxcl5
Edn1
Gm7714
Apoe
Dcn
Krt14
Krt5
Krt15
1600014C10Rik
Sfn
Krt17
Cp
Ifitm3
Expression
6
5
4
3
2
1
0
Identity
Lum-A
Lum-B
Lum-C
Lum-D
Lum-E
Lum-F
Bas
B
Intact
Regressed
Lum-A
Lum-B
Lum-C
Lum-D
Lum-E
Lum-F
RFP-
RFP+
RFP-
RFP+
Intact
Castrated
C
Intact
Regressed
Lum-A
Lum-B
Lum-C
Lum-D
Lum-E
Lum-F
RFP-
RFP+
AP
DLP
VP
D
'Ly6' family members
Ly6e
Ly6d
high
low
UMAP 2
UMAP 1
E
'Runx' family members
Runx2
Runx3
Cbfb
high
low
UMAP 2
UMAP 1

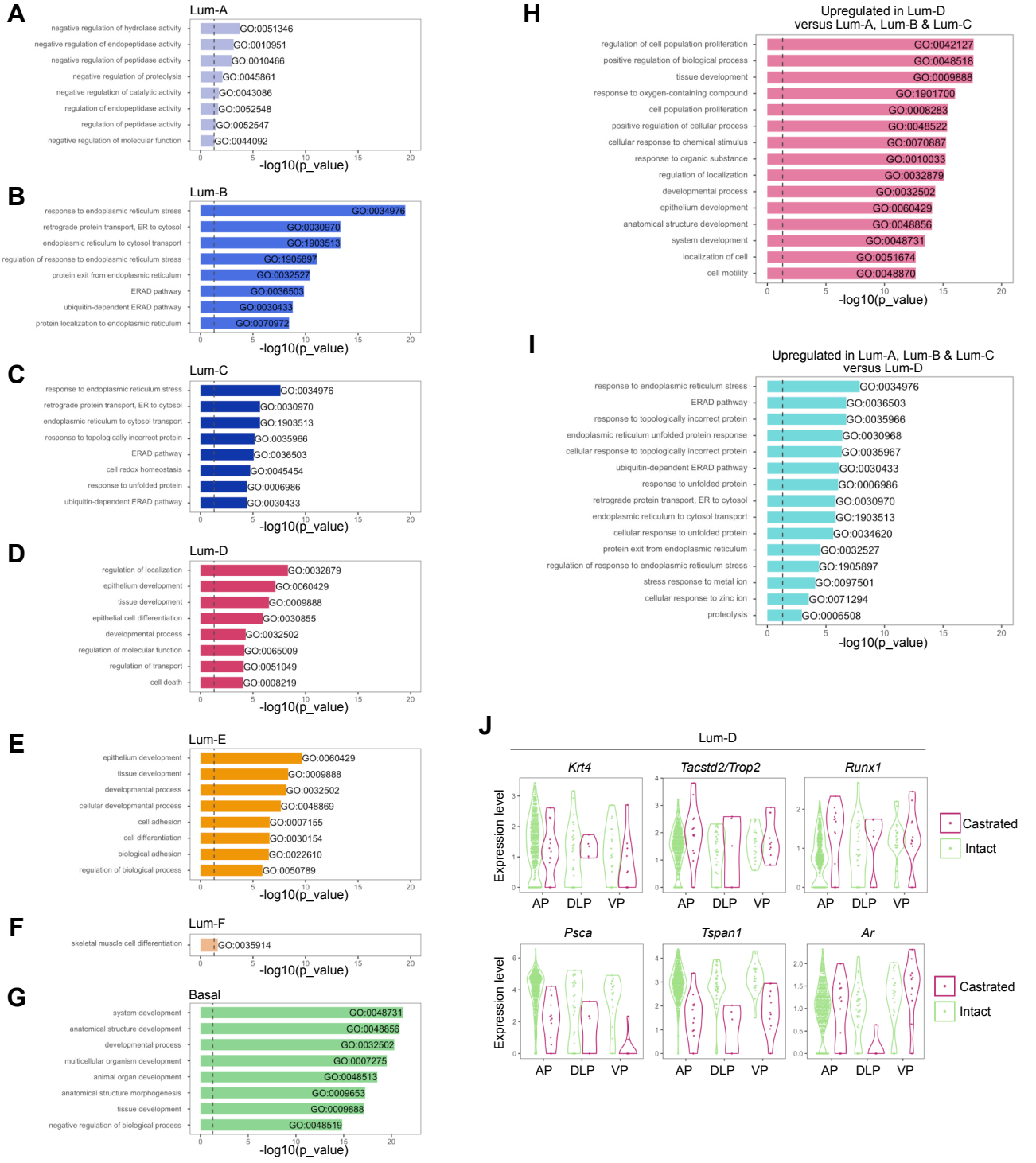
A
Lum-A
negative regulation of hydrolase activity
negative regulation of endopeptidase activity
negative regulation of peptidase activity
negative regulation of proteolysis
negative regulation of catalytic activity
regulation of endopeptidase activity
regulation of peptidase activity
negative regulation of molecular function
GO:0051346
GO:0010951
GO:0010466
GO:0045861
GO:0043086
GO:0052548
GO:0052547
GO:0044092
-log10(p_value)
B
Lum-B
response to endoplasmic reticulum stress
retrograde protein transport, ER to cytosol
endoplasmic reticulum to cytosol transport
regulation of response to endoplasmic reticulum stress
protein exit from endoplasmic reticulum
ERAD pathway
ubiquitin-dependent ERAD pathway
protein localization to endoplasmic reticulum
GO:0034976
GO:0030970
GO:1903513
GO:1905897
GO:0032527
GO:0036503
GO:0030433
GO:0070972
-log10(p_value)
C
Lum-C
response to endoplasmic reticulum stress
retrograde protein transport, ER to cytosol
endoplasmic reticulum to cytosol transport
response to topologically incorrect protein
ERAD pathway
cell redox homeostasis
response to unfolded protein
ubiquitin-dependent ERAD pathway
GO:0034976
GO:0030970
GO:1903513
GO:0035966
GO:0036503
GO:0045454
GO:0006986
GO:0030433
-log10(p_value)
D
Lum-D
regulation of localization
epithelium development
tissue development
epithelial cell differentiation
developmental process
regulation of molecular function
regulation of transport
cell death
GO:0032879
GO:0060429
GO:0009888
GO:0030855
GO:0032502
GO:0065009
GO:0051049
GO:0008219
-log10(p_value)
E
Lum-E
epithelium development
tissue development
developmental process
cellular developmental process
cell adhesion
cell differentiation
biological adhesion
regulation of biological process
GO:0060429
GO:0009888
GO:0032502
GO:0048869
GO:0007155
GO:0030154
GO:0022610
GO:0050789
-log10(p_value)
F
Lum-F
skeletal muscle cell differentiation
GO:0035914
-log10(p_value)
G
Basal
system development
anatomical structure development
developmental process
multicellular organism development
animal organ development
anatomical structure morphogenesis
tissue development
negative regulation of biological process
GO:0048731
GO:0048856
GO:0032502
GO:0007275
GO:0048513
GO:0009653
GO:0009888
GO:0048519
-log10(p_value)
H
Upregulated in Lum-D
versus Lum-A, Lum-B & Lum-C
regulation of cell population proliferation
positive regulation of biological process
tissue development
response to oxygen-containing compound
cell population proliferation
positive regulation of cellular process
cellular response to chemical stimulus
response to organic substance
regulation of localization
developmental process
epithelium development
anatomical structure development
system development
localization of cell
cell motility
GO:0042127
GO:0048518
GO:0009888
GO:1901700
GO:0008283
GO:0048522
GO:0070887
GO:0010033
GO:0032879
GO:0032502
GO:0060429
GO:0048856
GO:0048731
GO:0051674
GO:0048870
-log10(p_value)
I
Upregulated in Lum-A, Lum-B & Lum-C
versus Lum-D
response to endoplasmic reticulum stress
ERAD pathway
response to topologically incorrect protein
endoplasmic reticulum unfolded protein response
cellular response to topologically incorrect protein
ubiquitin-dependent ERAD pathway
response to unfolded protein
retrograde protein transport, ER to cytosol
endoplasmic reticulum to cytosol transport
cellular response to unfolded protein
protein exit from endoplasmic reticulum
regulation of response to endoplasmic reticulum stress
stress response to metal ion
cellular response to zinc ion
proteolysis
GO:0034976
GO:0036503
GO:0035966
GO:0030968
GO:0035967
GO:0030433
GO:0006986
GO:0030970
GO:1903513
GO:0034620
GO:0032527
GO:1905897
GO:0097501
GO:0071294
GO:0006508
-log10(p_value)
J
Lum-D
Krt4
Tacstd2/Trop2
Runx1
Psca
Tspan1
Ar
Expression level
AP
DLP
VP
Castrated
Intact

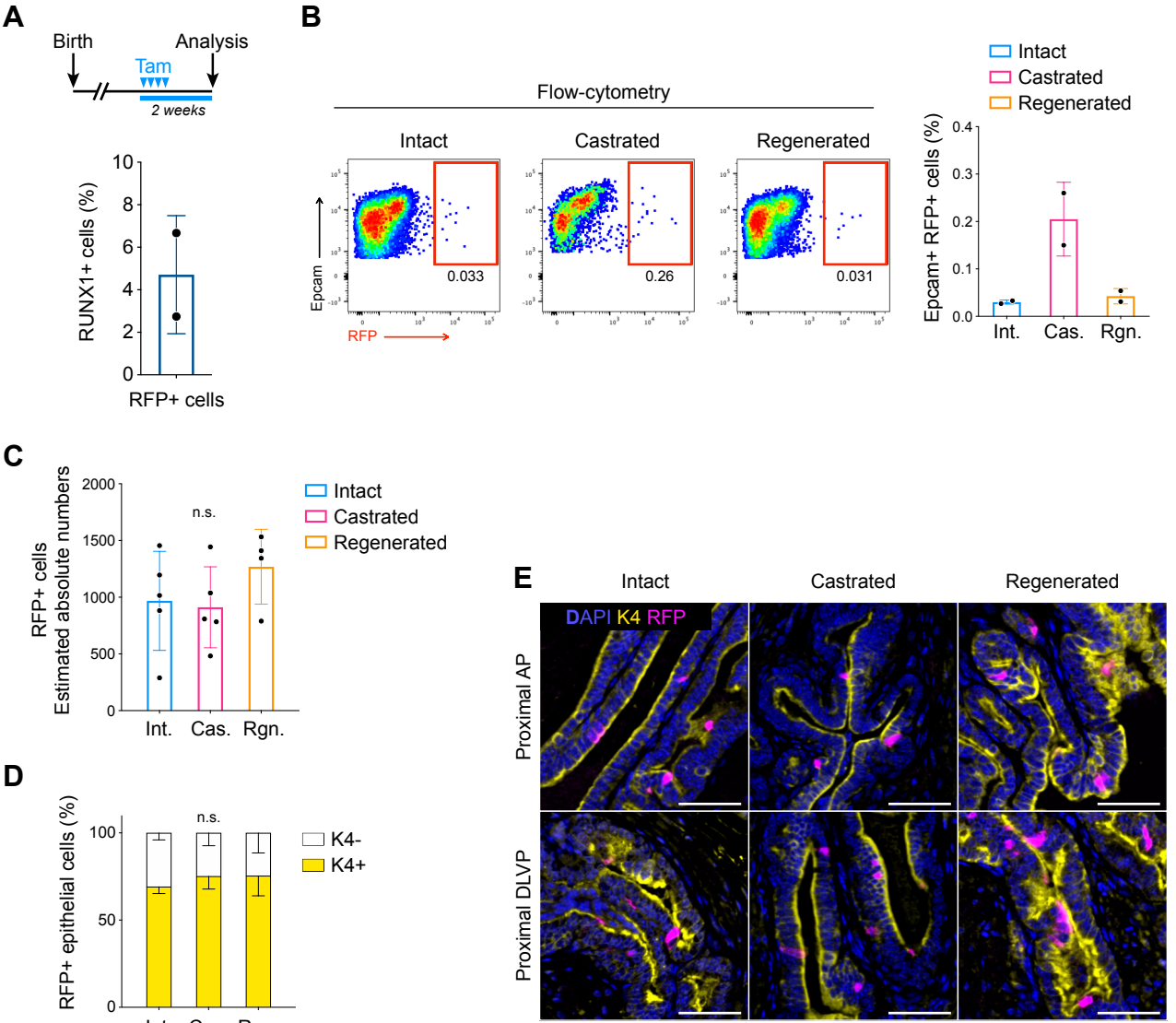
A
Birth
Analysis
Tam
2 weeks
RUNX1+ cells (%)
RFP+ cells
B
Flow-cytometry
Intact
Castrated
Regenerated
Epcam
RFP
0.033
0.26
0.031
Epcam+ RFP+ cells (%)
Int.
Cas.
Rgn.
C
RFP+ cells
Estimated absolute numbers
n.s.
D
RFP+ epithelial cells (%)
K4-
K4+
E
DAPI K4 RFP
Proximal AP
Proximal DLVP

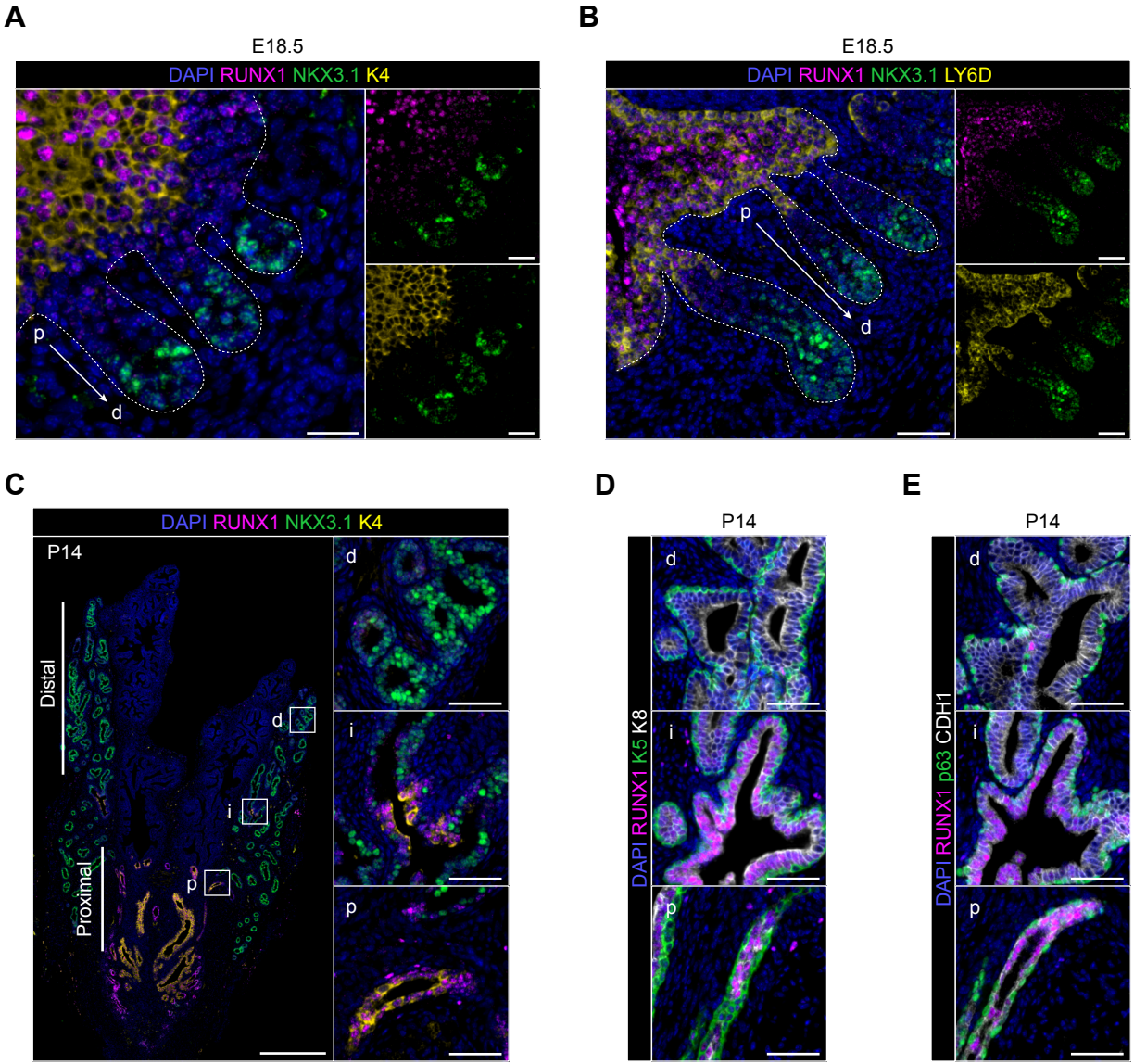
A
E18.5
DAPI RUNX1 NKX3.1 K4
p
d
B
E18.5
DAPI RUNX1 NKX3.1 LY6D
p
d
C
DAPI RUNX1 NKX3.1 K4
P14
Distal
Proximal
d
i
p
D
P14
DAPI RUNX1 K5 K8
E
P14
DAPI RUNX1 p63 CDH1

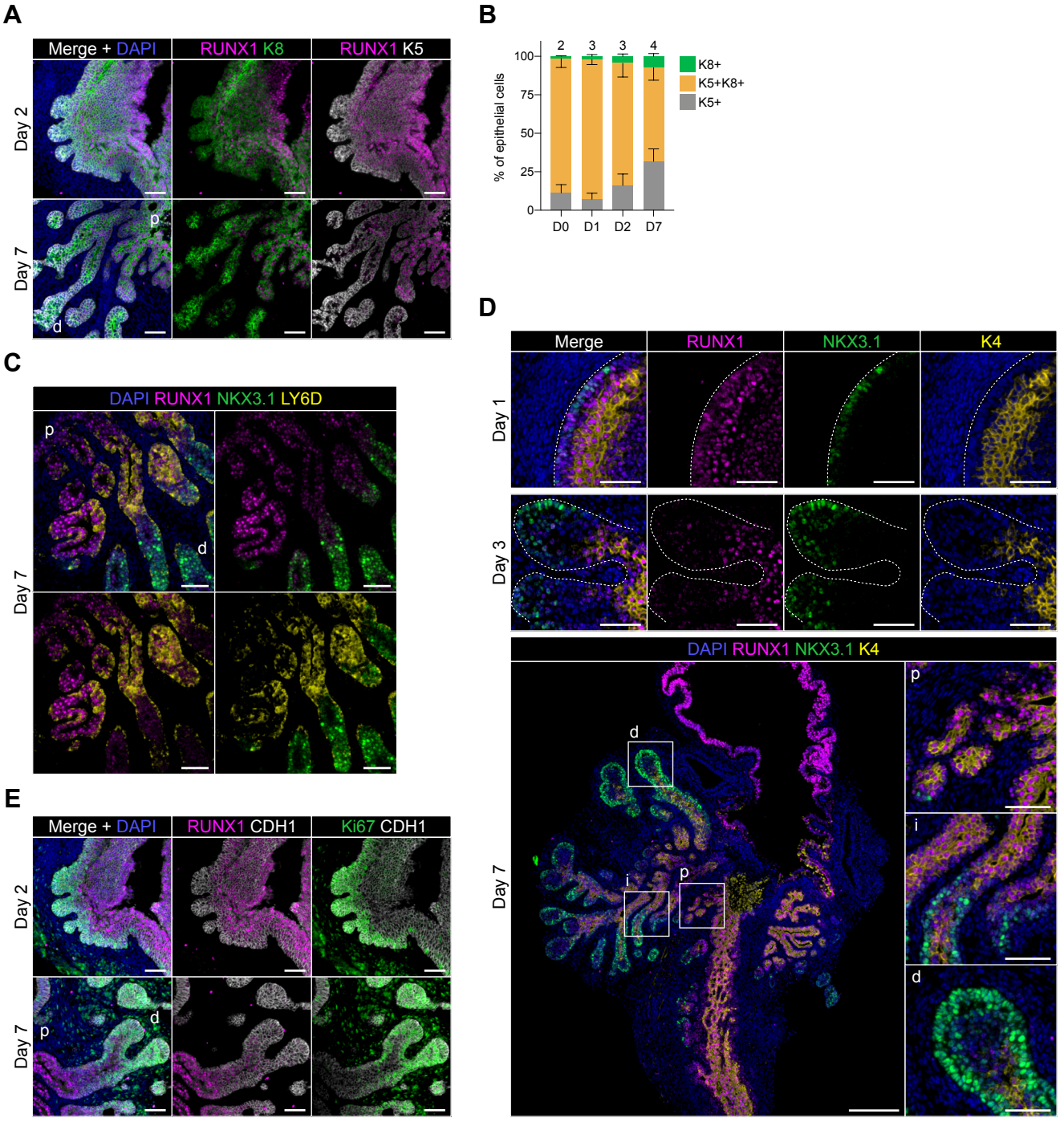
A
Merge + DAPI
RUNX1 K8
RUNX1 K5
Day 2
Day 7
p
d
B
% of epithelial cells
100
75
50
25
0
2
3
3
4
D0
D1
D2
D7
K8+
K5+K8+
K5+
C
DAPI RUNX1 NKX3.1 LY6D
Day 7
p
d
D
Merge
RUNX1
NKX3.1
K4
Day 1
Day 3
DAPI RUNX1 NKX3.1 K4
Day 7
d
i
p
E
Merge + DAPI
RUNX1 CDH1
Ki67 CDH1
Day 2
Day 7
p
d

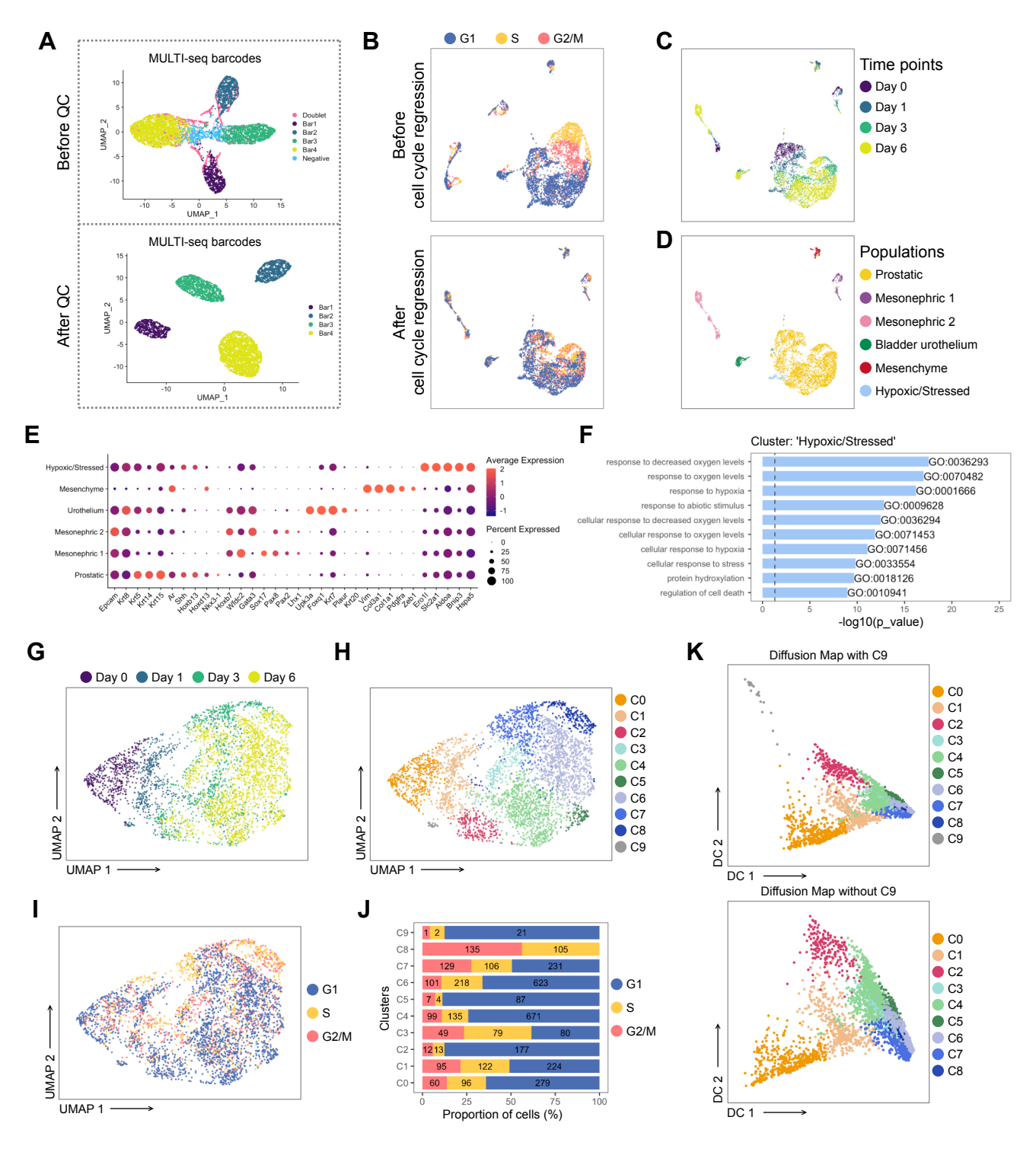
A
Before QC
MULTI-seq barcodes
Doublet
Bar1
Bar2
Bar3
Bar4
Negative
UMAP_1
UMAP_2
After QC
MULTI-seq barcodes
Bar1
Bar2
Bar3
Bar4
B
G1
S
G2/M
Before cell cycle regression
After cell cycle regression
C
Time points
Day 0
Day 1
Day 3
Day 6
D
Populations
Prostatic
Mesonephric 1
Mesonephric 2
Bladder urothelium
Mesenchyme
Hypoxic/Stressed
E
Hypoxic/Stressed
Mesenchyme
Urothelium
Mesonephric 2
Mesonephric 1
Prostatic
Average Expression
Percent Expressed
Epcam Krt8 Krt5 Krt14 Krt15 Ar Shh Hoxb13 Hoxd13 Nkx3.1 Hoxb7 Wnt3a2 Gata3 Sox17 Pax8 Pax2 Lhx1 Upk3a Foxa1 Krt7 Pla1r Krt20 Vim Col3a1 Col1a1 Pdgfra Zeb1 Ero1l Slc2a1 Aldoa Bnip3 Hspa5
F
Cluster: 'Hypoxic/Stressed'
response to decreased oxygen levels GO:0036293
response to oxygen levels GO:0070482
response to hypoxia GO:0001666
response to abiotic stimulus GO:0009628
cellular response to decreased oxygen levels GO:0036294
cellular response to oxygen levels GO:0071453
cellular response to hypoxia GO:0071456
cellular response to stress GO:0033554
protein hydroxylation GO:0018126
regulation of cell death GO:0010941
-log10(p_value)
G
Day 0
Day 1
Day 3
Day 6
UMAP 1
UMAP 2
H
C0
C1
C2
C3
C4
C5
C6
C7
C8
C9
UMAP 1
UMAP 2
K
Diffusion Map with C9
DC 1
DC 2
Diffusion Map without C9
DC 1
DC 2
I
G1
S
G2/M
UMAP 1
UMAP 2
J
Clusters
C9 1 2 21
C8 135 105
C7 129 106 231
C6 101 218 623
C5 7 4 87
C4 99 135 671
C3 49 79 80
C2 12 13 177
C1 95 122 224
C0 60 96 279
Proportion of cells (%)
G1
S
G2/M

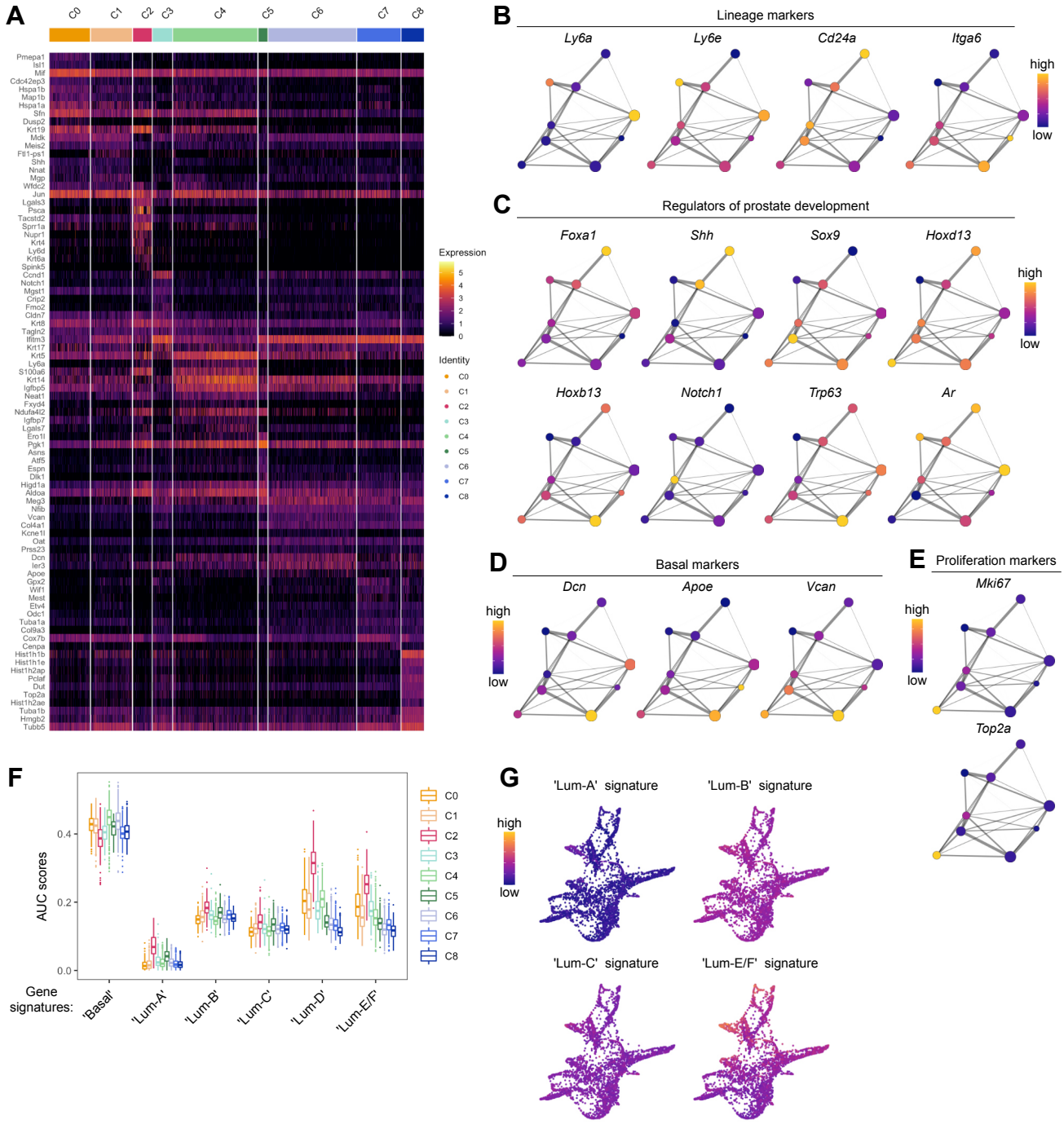
A
C0
C1
C2
C3
C4
C5
C6
C7
C8
Pmepa1
Isl1
Mif
Cdc42ep3
Hspa1b
Map1b
Hspa1a
Sfn
Dusp2
Krt19
Mdk
Meis2
Fit1-ps1
Shh
Nnat
Mgp
Wfdc2
Jun
Lgals3
Psca
Tacstd2
Sprr1a
Nupr1
Krt4
Ly6d
Krt6a
Spink5
Ccnd1
Notch1
Mgst1
Crip2
Fmo2
Cldn7
Krt8
Tagln2
Ifitm3
Krt17
Krt5
Ly6a
S100a6
Krt14
Igfbp5
Neat1
Fxyd4
Ndufa4l2
Igfbp7
Lgals7
Ero1l
Pgk1
Asns
Atf5
Espn
Dlk1
Higd1a
Aldoa
Meg3
Nfib
Vcan
Col4a1
Kcne1l
Oat
Prss23
Dcn
Ier3
Apoe
Gpx2
Wif1
Mest
Etv4
Odc1
Tuba1a
Col9a3
Cox7b
Cenpa
Hist1h1b
Hist1h1e
Hist1h2ap
Pclaf
Dut
Top2a
Hist1h2ae
Tuba1b
Hmgb2
Tubb5
Expression
5
4
3
2
1
0
Identity
C0
C1
C2
C3
C4
C5
C6
C7
C8
B
Lineage markers
Ly6a
Ly6e
Cd24a
Itga6
high
low
C
Regulators of prostate development
Foxa1
Shh
Sox9
Hoxd13
Hoxb13
Notch1
Trp63
Ar
high
low
D
Basal markers
Dcn
Apoe
Vcan
high
low
E
Proliferation markers
Mki67
Top2a
high
low
F
AUC scores
0.0
0.2
0.4
Gene signatures:
'Basal'
'Lum-A'
'Lum-B'
'Lum-C'
'Lum-D'
'Lum-E/F'
C0
C1
C2
C3
C4
C5
C6
C7
C8
G
'Lum-A' signature
'Lum-B' signature
'Lum-C' signature
'Lum-E/F' signature
high
low

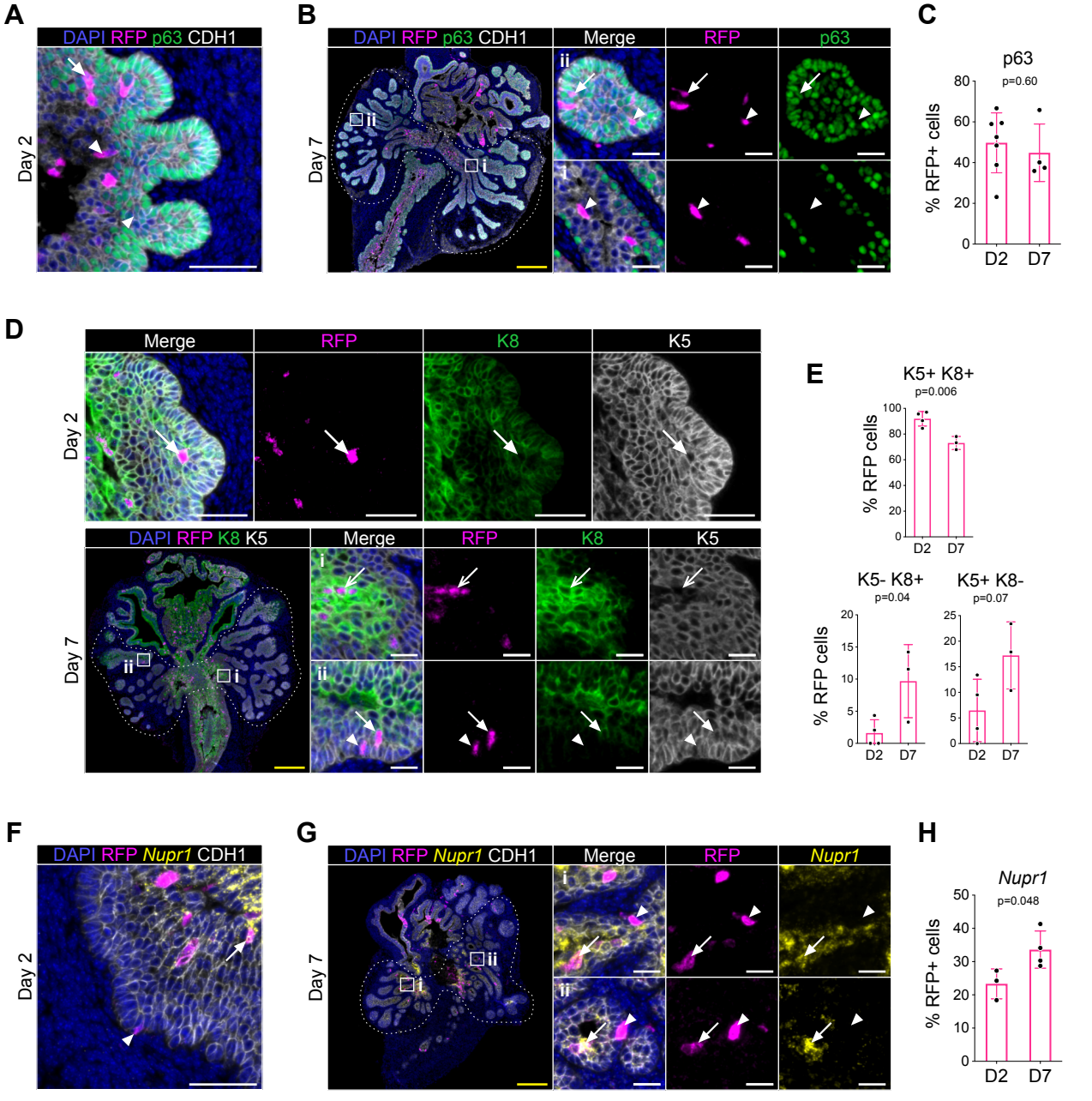
A
DAPI RFP p63 CDH1
Day 2
B
DAPI RFP p63 CDH1
Merge
RFP
p63
Day 7
ii
i
C
p63
p=0.60
% RFP+ cells
80
60
40
20
0
D2
D7
D
Merge
RFP
K8
K5
Day 2
DAPI RFP K8 K5
Merge
RFP
K8
K5
Day 7
ii
i
E
K5+ K8+
p=0.006
% RFP cells
100
80
60
40
20
0
D2
D7
K5- K8+
p=0.04
K5+ K8-
p=0.07
% RFP cells
20
15
10
5
0
25
20
15
10
5
0
D2
D7
F
DAPI RFP Nupr1 CDH1
Day 2
G
DAPI RFP Nupr1 CDH1
Merge
RFP
Nupr1
Day 7
i
ii
H
Nupr1
p=0.048
% RFP+ cells
50
40
30
20
10
0
D2
D7